The Pennsylvania State University

The Graduate School

TESTS OF GENERALIZED HYDRODYNAMICS IN ONE-DIMENSIONAL BOSE GASES

A Dissertation in

Physics

by

Neel Malvania

Submitted in Partial Fulfillment

of the Requirements

for the Degree of

Doctor of Philosophy

December 2021

The dissertation of Neel Malvania was reviewed and approved by the following:

David S. Weiss

Distinguished Professor of Physics

Dissertation Advisor

Chair of Committee

Mikael C. Rechtsman

Downsbrough Early Career Development Professor of Physics

Eric Hudson

Associate Professor of Physics and Associate Head for Diversity

Roman Engel-Herbert

Associate Professor of Materials Science and Engineering and Physics

Nitin Samarth

George A. and Margaret M. Downsbrough Department Head and Professor of Physics

Abstract

Strongly interacting quantum many-body systems are widely studied in physics due to their complexity and the wide range of phenomena they exhibit. With complicated many-body interactions, systems can often be described in terms of emergent quasiparticles, which often simplify the behavior. In the special case of integrable systems, the momentum distribution of quasiparticles is referred to as the distribution of rapidities. For most systems, currently available theoretical tools are limited in their ability to calculate dynamics except in certain limits. Fortunately, efficient dynamical calculations are now possible with the advent of a new method called Generalized Hydrodynamics (GHD). GHD aims to simulate dynamics for interacting many-body systems near an integrable point by following the evolution of rapidities (ie. the momenta of the underlying quasiparticles).

In the experiments presented in this thesis, we study 1D Bose gases in a trap, whose interactions are described by the Lieb-Liniger model. Prior to our recent work, an experiment with a 1D Bose gas validated GHD predictions in the weak coupling regime. Here we test GHD in nearly-integrable interacting 1D gases in an 2D array formed using an optical lattice. We perform large quenches of the initial confining potential and directly measure the evolving rapidity distributions in the strong and intermediate coupling regimes. Our experimental results agree extremely well with GHD predictions for many trap oscillation periods. Even when the assumptions underlying GHD are challenged in one of our quenches, the theory does remarkably well in describing the experiment.

Another experiment we have started to work on is studying evolution after a strong wavefunction quench, where the gas is put locally out of equilibrium. Here we strive to observe and understand the approach to local equilibrium, which is outside the realm of GHD. This is an ongoing project, so I will only present some preliminary experimental results. I will also briefly describe recent and upcoming upgrades to the apparatus that will serve to broaden the range of experiments that we can perform.

Table of Contents

List of Figures

Acknowledgments

First and foremost, I would like to thank my supervisor and mentor, Prof. David S. Weiss. His dedication and passion for science is touching. Over the years he has willingly sacrificed much of his personal time to help out myself and all his other students whenever we have any problems or concerns. He is knowledgeable in essentially everything, and is extremely careful and thorough in all aspects of the scientific process. Apart from being a fantastic educator, he is a very patient and understanding communicator. I have learnt a lot from him and I am fortunate to have worked under his guidance for the past six years.

I also thank Joshua Wilson and Yuan Le for keeping me company in the dark reaches of our Davey basement lab. It hasn't always been fun and games down there, but I have had some great moments and conversations with them while conducting research. Whether it was silly videos, uncontrollable laughs, times with lab equipment frustrations, impromptu foreign language sessions, or sleepless nights of data collecting, I am glad they were there to keep me (mostly) sane during my time here. They are both amazing people and I couldn't ask for better lab partners.

Next I would like to thank our theory collaborators, Marcos Rigol and Yicheng Zhang, for their deep contributions and calculations for our recent experiments. Their theoretical insight has been crucial in helping us better understand some of the unintuitive concepts we have come across.

I am grateful for the other research group members I've had the chance to interact with: Laura Zundel, Lin Xia, Cheng Tang, Yang Wang, Aishwarya Kumar, Teng Zhang, Tsung-Yao Wu, Felipe Giraldo Mejia, Zhenyu Wei, Peng Du, and Maarten De Haan. It has been a pleasure catching up with them at group meetings, helping each other out and bouncing ideas off each other.

I want to thank all my friends for the sense of community and family they have provided. I feel so incredibly lucky to have friends that are not only tolerant of my unpredictable and volatile work hours, but are selflessly willing to check in with me and help out when I am going through a rough time. Even though a lot of them are very far away, they have been super supportive and are always enthusiastically looking forward to my visits.

Last but not least, I am thankful to my family for their never-ending support, love, and concern for my well-being while I was in graduate school. I would not be where I am today had they not nurtured my curiosity and encouraged me to perform experiments with household objects, read extensively, and ask questions while growing up.

The content of this thesis is based upon work supported by the NSF under Grant No. PHY-2012039, the Army Research Office under Grant No. W911NF-16-0031-P00005. Any opinions, findings, and conclusions or recommendations expressed in this publication are those of the author and do not necessarily reflect the views of the NSF, or the Army Research Office.

Chapter 1

Introduction

Integrable systems are a special class of physical systems, both in classical and quantum physics. Perhaps the most striking feature of these systems is the existence of extra constants of motion apart from just energy and momentum. This lets them have a 'memory' of their initial state, and as a consequence, impedes these systems from thermalizing when taken out of equilibrium. While statistical mechanics can in general be used to predict the behavior of physical systems, it does not apply to integrable systems because of the constraints put in place by the large set of conserved quantities.

With very few exceptions, many-body systems have inter-particle interactions. These can be attractive or repulsive, short range or long range. Often in interacting systems one wants to understand the collective many-body behavior. When bare particles become dressed by interactions, the system can be expressed in the language of the emergent quasiparticles. Quasiparticles are used universally in other branches of physics such as condensed matter physics to help make the system behavior more intuitive. Generally, quasiparticles provide an approximation for calculating system properties and they have a

finite lifetime. For integrable systems, however, the quasiparticle description is exact and the quasiparticles live forever [1]. Their momentum distribution is called the distribution of rapidities.

Integrable many-body systems have been of interest to theorists over the decades because unlike most many-body quantum systems, they are exactly solvable in equilibrium. Perhaps one of the simplest is the one-dimensional (1D) Bose gas and its properties have been well-studied theoretically for a long time [2]. In the last two decades, several developments have made ultracold atom experiments a viable tool to study this system experimentally [3, 4]. Results from several experiments have shown that good approximations to these systems can be produced in the laboratory. However, until very recently there has not been a direct measurement of rapidities in an interacting many-body system. Armed with the techniques demonstrated in [5], our 1D Bose gas apparatus can now measure the rapidity distributions of out-of-equilibrium states.

On the theoretical side, it is difficult to study many-body system dynamics beyond special cases due to the complex nature of the interactions between particles, even for integrable systems. It was only a few years ago that a method called generalized hydrodynamics (GHD) was developed to tackle this issue. Before the work I will describe in this thesis, GHD has only been applied to one other experiment, a weakly interacting 1D Bose gas on an atom chip [6]. In the quench experiments that I discuss in this thesis, this approach will prove useful in describing dynamics even in the strongly interacting regime.

1.1 The Lieb-Liniger model

The first paper to introduce a 1D gas of interacting bosons was presented by Marvin Girardeau in 1960, in which he described bosons with an "impenetrable core" [7]. In 1963, Elliot Lieb and Werner Liniger came up with an extension where the strength of interactions could be arbitrary, and in one limit would reduce to Girardeau's system. A relatively simple model, the Lieb-Liniger Hamiltonian describes bosons that interact via a repulsive δ-function interaction [8].

$$H = \sum_{i=1}^{N} \frac{-\hbar^2}{2m} \frac{\partial^2}{\partial z_i^2} + \sum_{i<j} g_{1D} \delta(z_i - z_j) \tag{1.1}$$

In the above Hamiltonian for N particles, the first term is the kinetic energy term and the second term is the interaction term with strength g_{1D}, which only becomes relevant when the relative coordinate between two particles is zero. This model was first solved exactly by Lieb and Liniger using a Bethe ansatz approach [9] and has been thoroughly studied since. When solved at zero temperature, one finds that the system in equilibrium can be described by a dimensionless coupling parameter which sets the strength of the interaction;

$$\gamma = \frac{m g_{1D}}{\hbar^2 n_{1D}} \tag{1.2}$$

where n_{1D} is the 1D density.

When γ is close to zero, the weak nature of the interaction puts the system in the

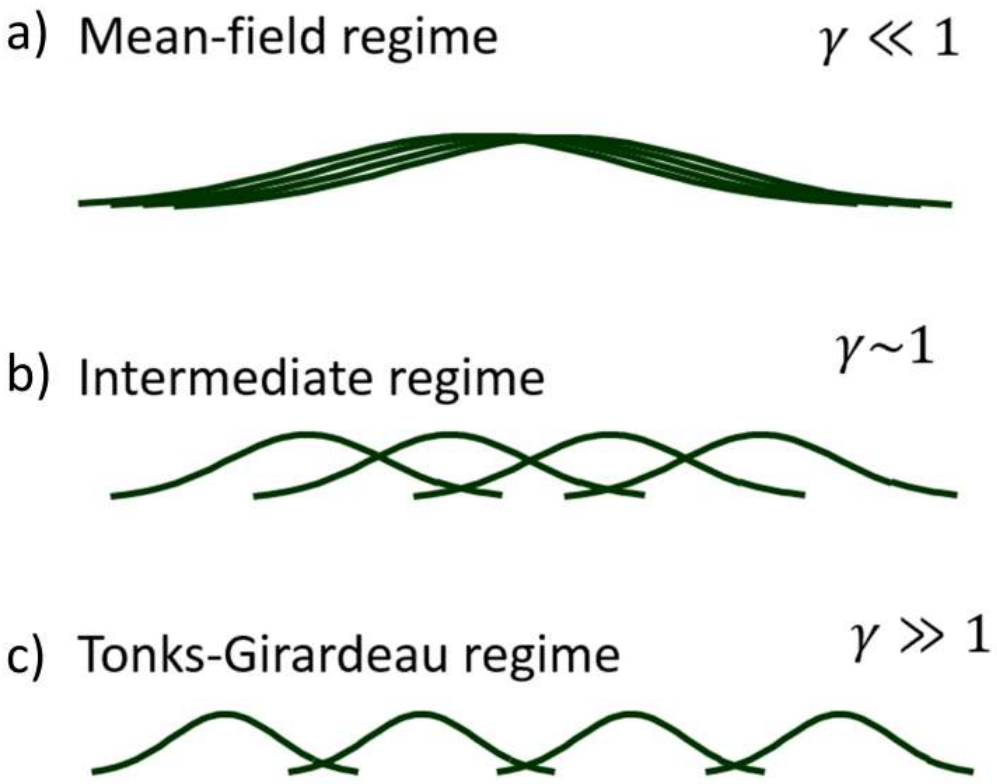

Figure 1.1. Cartoon illustrations of 1D Bose gas correlations. In the mean-field regime (top) it is not difficult to find two particles at the same position. As γ gets larger the correlations get stronger and particles tend to avoid each other more and more (middle). The Tonks-Girardeau regime (bottom) features a very low probability of finding two particles at the same point. In the $\gamma \to \infty$ limit, this probability approaches zero and the gas can be mapped onto a non-interacting Fermi gas. Adapted from Ref [10].

mean-field limit dominated by interaction energy. As γ gets larger, it becomes more energetically costly to have particles close together, so correlations form in the system. This results in the single particle parts of the many-body wavefunctions developing additional curvature in order to minimize energy (see Figure 1.1). In the limit of infinitely strong interactions (known as the Tonks-Girardeau limit) the correlations are such that it is impossible to find two particles at the same point, so the particles are sometimes referred to as hard-core bosons. Here, the strong correlations cause the many-body

wavefunction to develop large curvatures, which is associated with a large amount of kinetic energy. This is a special limit of the Lieb-Linger model: due to the vanishing pair correlation function the bosonic particles effectively behave as though they are experiencing Pauli exclusion, a feature of fermionic systems. Here the bosonic many-body wavefunction of the system is the same as for a non-interacting Fermi gas, up to an absolute value sign:

$$\psi_o^B = |\psi_o^F| \tag{1.3}$$

This phenomenon is aptly referred to as Bose-Fermi duality.

1.2 Adaptation of the Lieb-Liniger model in experiment

The first proposal for realizing a Lieb-Liniger gas came from Maxim Olshanii in 1998. He showed that collisions between ultracold atoms in a 1D waveguide can be mapped onto bosons scattering off of a δ-function potential in the low-energy limit [11]. Specifically, the scattering amplitude for the bosons can be written as

$$f_{even}(k_z) \approx \frac{-1}{1 + ik_z a_{1D}} \tag{1.4}$$

The form of Equation 1.4 turns out to have the same properties as scattering from a potential $U_{1D}(z) = g_{1D}\delta(z)$, where $g_{1D} = -\hbar^2/(\mu a_{1D})$ and a_{1D} is the 1D scattering

length. One can express this quantity in terms of further reducible quantities:

$$a_{1D} = -\frac{a_\perp^2}{2a_{3D}}(1 - 1.46\frac{a_{3D}}{a_\perp}) \tag{1.5}$$

Here, $a_\perp$ is the transverse size of the ground state wavefunction (determined by the atom trapping geometry) and a_{3D} is the 3D scattering length. Equipped with this mapping, Olshanii was able to write the interaction parameter in terms of experimental quantities [12]:

$$\gamma = \frac{2}{n_{1D}|a_{1D}|} \tag{1.6}$$

$$\gamma \approx \frac{4a_{3D}}{a_\perp^2 n_{1D}} \tag{1.7}$$

In the next chapter I will outline how we achieve 1D trapping of atoms in a waveguide, thereby experimentally realizing the Lieb-Liniger model.

1.3 The hydrodynamic description

One can study physical systems on a range of distance and time scales. At the level of individual particles, a microscopic description requires a detailed understanding of their interactions. At a larger distance scale and on time scales much longer than collision times, systems have characteristic equilibration times for local relaxation. In these cases, a hydrodynamic description is often more useful since it simplifies calculations

by focusing on continuous quantities like density instead of the behavior of individual particles. On time scales much longer than the local relaxation time, the system can be approximated as being in local equilibrium. Therefore, local equilibrium states can be written in terms of conserved quantities in the system and the time evolution of the system can be described by continuity equations. For conventional fluids, one can write continuity equations for mass density, momentum density, and energy density, corresponding to the conserved quantities: particle number, momentum and energy. This is the "coarse-grained" hydrodynamic description; it is valid for large distances and long time scales.

1.4 Generalized Hydrodynamics

In order to utilize the power of the hydrodynamic approach for quantum integrable systems such as the Lieb-Liniger model, one has to extend the concept to include the infinite number of conserved quantities involved [13, 14]. The "generalized" formulation of hydrodynamics, known simply as Generalized Hydrodynamics (GHD), focuses on the evolution of the distribution of underlying quasiparticles, which have an "effective velocity" instead of a single-particle group velocity [15].

The emergence of an effective velocity can be visualized in the simplest system that exhibits generalized hydrodynamics: a classical 1D hard rod gas. If we imagine individual particle motion along the 1D direction, at each collisional event there is an exchange of single-particle velocities. Tracking the trajectory of the highlighted particle over many

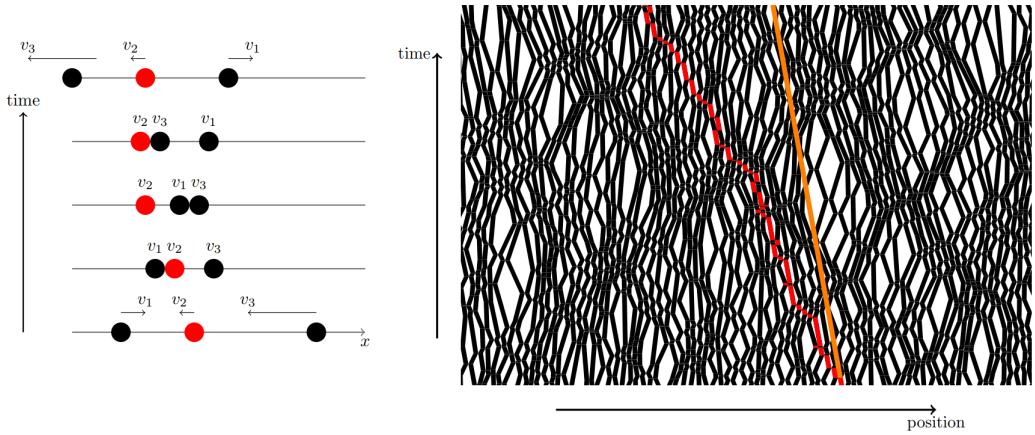

Figure 1.2. Emergence of an effective velocity in a classical 1D hard rod gas. When balls collide elastically with each other they simply exchange velocities. Being identical, one can re-label the balls to have the bare velocity be constant (as done with the red ball in the left panel). At large distances and long timescales, the trajectory of the red ball (red line on the right panel) has an 'effective velocity' that is different than its bare velocity (orange line). Adapted from Ref [16].

collisions, we can see that it drifts with an effective velocity that is different from its original bare velocity, as illustrated in Figure 1.2. This is essentially because of the role of interactions in the system. The rapidities, which are the quasiparticle momenta, are built into the framework of GHD. When there is an external potential, integrability is lifted but often only weakly. A hallmark of integrable systems is the absence of diffractive 3-body collisions [17]. When integrability is broken, diffractive 3-body collisions can occur and to the extent that they do, quasiparticles have a finite lifetime. In systems like ours, diffractive collisions arise mainly from virtual transverse excitations [18], but there are a number of other ways that they can show up [19, 20]. On times shorter than the diffractive 3-body collision timescale, GHD is able to efficiently calculate system dynamics by following the quasiparticle evolution.

Generalized hydrodynamics uses two core assumptions [21–23]. First, the system is

spatially discretized into an array of small fluid cells which are each spatially homogeneous. Each fluid cell is viewed as having lots of particles so as to appear coarse-grained for the hydrodynamic approximation. Additionally, each cell is assumed to be describable by an integrable model, and in our case, the Lieb-Liniger model. And second, each fluid cell is locally equilibrated to a generalized Gibbs ensemble (GGE). Here, system evolution is assumed to be slow enough compared to local relaxation time scales that the assumed local equilibrium state can always be written in terms of the distribution of rapidities. We test these two assumptions in the bulk of the work presented in this dissertation.

1.5 Contributions to other projects

During the course of my time on the 1D Bose gas apparatus, I've worked on projects other than the main rapidity evolution and GHD project discussed in this dissertation.

1.5.1 Precision measurements of the equilibrium momentum distribution

Even though the Lieb-Liniger model is exactly solvable for all coupling strengths, only its local properties are calculable. Non-local properties such as momentum distributions are not easily found; there is no straightforward way of taking a Fourier transform of the spatial many-body wavefunction since it is highly correlated. They can only be calculated exactly in the $\gamma \to 0$ and $\gamma \to \infty$ limits [24]. Recent developments in Monte Carlo techniques have made it possible to determine the equilibrium momentum distributions

at arbitrary coupling strengths and finite temperatures [25–27].

When I joined the lab, we were starting to experimentally access the momentum distributions and perform clean measurements so that we could compare to theoretical predictions. We use a time-of-flight (TOF) method, where the spatial distribution after a period of free-space expansion from a trap maps onto the initial momentum distribution. Of course, this mapping is only accurate if the TOF distribution is much larger than the initial size of the cloud. Given experimental limitations on the length of the time of flight, other methods have to be used.

We implemented a momentum focusing technique to circumvent the problem of the initial size effect, similar to the one utilized in [28]. This scheme is explained at length in Joshua Wilson's dissertation, so I will not go into too much detail [29]. Essentially it involves giving an impulse to the gas in the form of a harmonic trap, such that each momentum component receives a momentum kick proportional to its distance from the trap center. Since the kick is linear in position, there exists a TOF for a particular impulse strength such that identical momentum components – no matter where they originate – arrive at the same position after the time-of-flight.

We have performed preliminary tests with this focusing technique with our approximately harmonic trap. The results demonstrate that this method is effective in measuring the momentum distributions, and we may use it in future experiments.

1.5.2 Thermalization in a Quantum Newton's Cradle

The original Quantum Newton's Cradle experiment showed that 1D Bose gases do not thermalize on experimental time scales when put in highly non-equilibrium states [30]. Since this landmark paper from our group in 2006 there have been further efforts to understand the onset of thermalization in our system and by other groups as well [19]. It is known that virtual transverse excitations in atomic waveguides allow for diffractive 3-body collisions, which can lead to thermalization [18, 20]. To understand how robust our adaption of the Lieb-Liniger Hamiltonian is to thermalization due to these collisions, we needed to understand the heating mechanisms that are present during the QNC evolution.

Density independent processes like absorption and spontaneous emission of lattice photons are the dominant source of heating. Heating from these had been modeled by calculating the spontaneous emission rates and shown to agree with measurements of QNC evolution at low densities [31, 32]. We then performed experiments at high densities, where we observed 3-body loss with a clear energy dependence, something that is not a feature of 3D gases [33, 34]. We calculated the heating from this effect based on an empirical model and also the cooling from evaporative processes. The analysis and results from these experiments and computations forms the core of Laura Zundel's dissertation [35].

Combined, all these mechanisms capture most of the observed energy evolution, but there is still some that is not accounted for. We have started to look at an effective

mean-field potential created by the axial distribution as part of a possible explanation.

1.6 Thesis Overview

The out-of-equilibrium dynamics of strongly interacting 1D Bose gases are not easily simulated. Current methods for exact dynamical calculations are only valid in the very special cases of the mean-field and Tonks-Girardeau limits. To efficiently simulate dynamics in all regimes, we use a recently developed model called generalized hydrodynamics (GHD).

In this thesis I will describe recent experiments that study the evolution of 1D Bose gases with high precision after a quench and how the results compare to GHD predictions. Chapter 2 will go into length about the different elements of the experimental setup. This includes the process of creating a Bose-Einstein condensate through laser cooling and trapping and evaporation [36, 37], and achieving a 1D trapping geometry for an atom waveguide array using a 2D optical lattice. I will also describe our control over the coupling parameter via tunability of atom number and axial trap depth. Recent improvements that allow us to fine-tune the axial cloud position relative to the trap center will be explained, and finally the way we acquire data using our imaging system will be mentioned.

I will lay out the measurement scheme and techniques we use to observe momentum and rapidity evolution in our experiments in Chapter 3. I will talk about the time-of-flight (TOF) measurement via rapid shutoff of the 2D lattice. Next, I will explain the creation

of a flat potential for 1D expansion that is needed for a rapidity measurement and provide a recap of our previous dynamical fermionization measurement. Lastly, the procedure to quench the 1D gas ensemble to bring the system out of equilibrium will be presented.

The theoretical methods of GHD will be discussed in Chapter 4. I will describe the process of calculating the initial state of the 1D Bose gas array that is used in the simulation. Thereafter, we model evolution of the system after a 10x or 100x trap quench. I describe the relevant GHD equation for each 1D gas and how it can be written as an equation for a time-dependent parametric curve in phase space. The process of extracting the theoretical spatial and rapidity distributions will also be detailed here, along with methods for obtaining the total rapidity energy as well as the interaction and kinetic energies.

In Chapter 5 I will talk about the extension of the rapidity measurement scheme for variable times after a trap quench. We adapt timing protocols for performing both a rapidity measurement and a momentum measurement. As a function of time after the quench we measure these distributions and compute their respective energies and compare them to the GHD predictions. The results agree well with each other for the first few cycles in both quenches, even when the core GHD assumptions are challenged by relatively low particle numbers in the 1D gases. I will go through several sources of discrepancy, including experimental imperfections in the trapping and in the quench, and atom loss at higher density instances during evolution.

Finally, Chapter 6 will start by going over a different type of quench that we started exploring but have not quite finished. This dramatic wavefunction quench puts the system

out of equilibrium by introducing momentum sidebands on the atomic wavefunction. This is done by suddenly pulsing on a lattice potential along the axial direction, analogous to light diffracting from a diffraction grating. I will present preliminary results of the momentum distributions after a variable evolution time, and follow the width of the central peak of the distribution.

I will conclude this thesis and elaborate on recent upgrades that have been made to the apparatus, such as the installation of a new 50 W 1064 nm laser that will serve as a generator for several new beams. We have already set up a beam path to use more than double the power previously available for the crossed dipole trap, in order to have a more stable BEC. We plan on using the rest of the power to create a more uniform trapping geometry for our 1D Bose gas array, so that future experiments are able to probe sharper features that would otherwise be smoothed out by tube averaging.

Chapter 2

Experimental Apparatus

A central development in the history of ultracold atom experiments was the creation of a Bose-Einstein condensate (BEC). This state of matter is formed when a dilute gas of bosons gets cold enough that the particles' spatial wavefunctions extend beyond the interparticle distance and there is macroscopic occupation of the ground state. Although it was predicted a century ago, the first BEC was only produced in a laboratory in 1995 independently by the Cornell and Wiemann lab and Ketterle lab [38, 39].

In this chapter I will talk about how we experimentally create a Lieb-Liniger gas in our laboratory using a BEC as a starting point. We take advantage of the optical atomic transitions of ^{87}Rb to slow and cool atoms starting from an atomic beam oven down to a BEC that is only at a few nanokelvin. I will talk about the vacuum chamber where all the science occurs, and mention the lasers and other devices that generate and manipulate our beams so the light is at the necessary wavelengths. Our cooling and trapping process to obtain a BEC involves chirped slowing, polarization gradient cooling and evaporative cooling. The experimental setup and procedure have been described

in detail, first in Trevor Wenger's thesis and then in Laura Zundel's thesis, and has not changed significantly since, so I will not go into too much depth [35, 37]. Next, I will talk about how we make an ensemble of 1D gases and the complications involving averaging due to inhomogeneity between individual gases. Finally, I will outline the data acquisition process using our imaging system, and how we do the initial image conditioning before further analysis.

2.1 Our lasers and optical transitions

The fact that atoms are polarizable has enabled researchers in the last few decades to use lasers and other narrow linewidth sources to manipulate them. We use several different types of lasers to generate the necessary beams for slowing, cooling and trapping throughout the experiments. The atomic species used in this apparatus is ^{87}Rb. We take advantage of the D_2 line in the energy level structure (shown in Figure 2.1) where levels $5S_{1/2}$ and $5P_{3/2}$ are split due to hyperfine interactions.

2.1.1 Ti:Sapph I

For slowing and cooling the atoms we use red-detuned light near the $F = 2$ to $F^{'} = 3$ optical transition. The source of this light is a Ti:Sapphire ring laser we call Ti:Sapph I. 4.8 Watts of 532 nm light from a V-18 Verdi laser is used as the seed for Ti:Sapph I, which outputs about 350 mW of power at 780.24 nm [1]. Using saturation absorption

[1] Over the years the power output of Ti:Sapph I has decreased considerably, so in the near future we plan on replacing it with a fiber laser that can give us 1 W of power

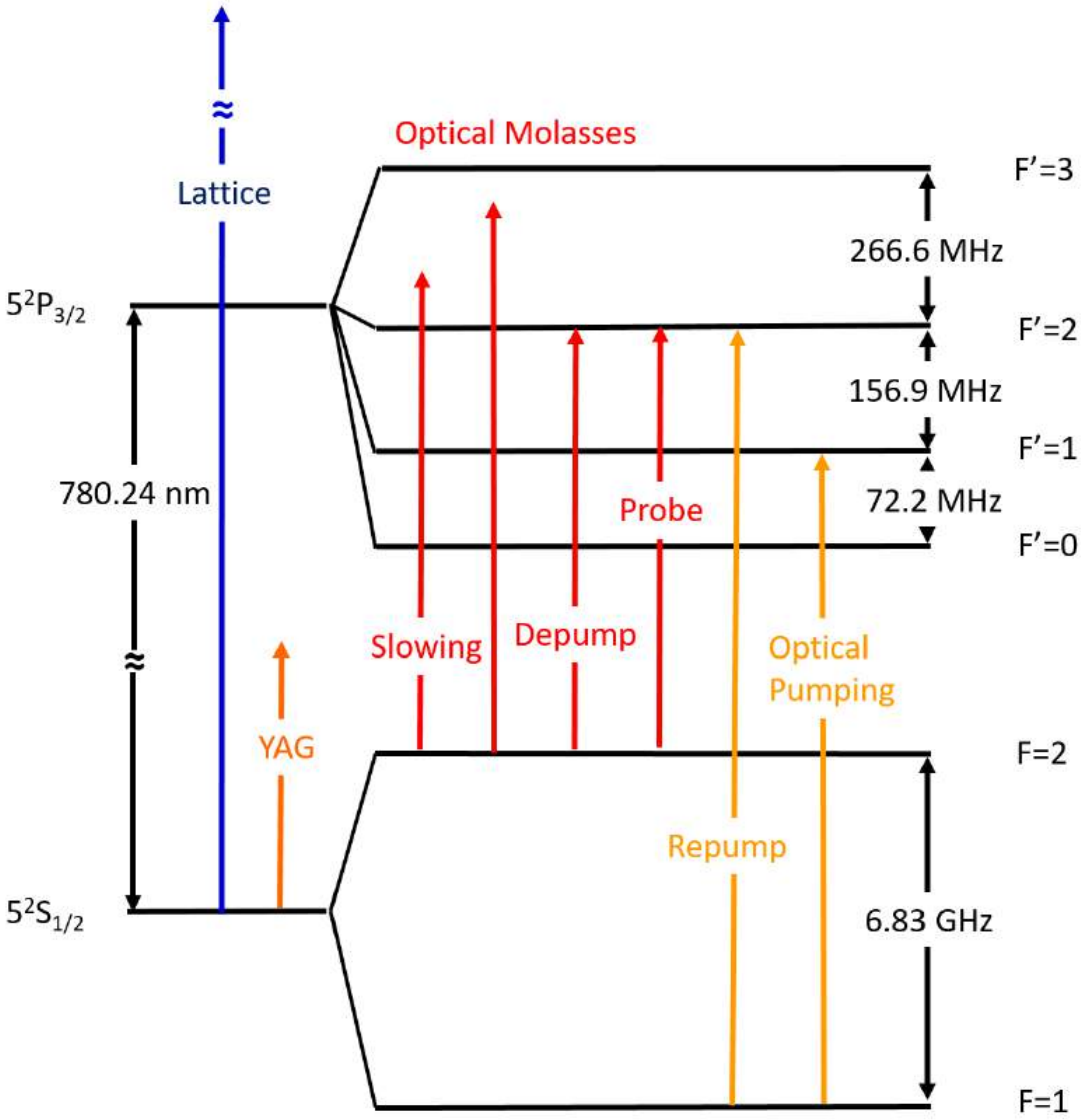

Figure 2.1. Energy level diagram for the D_2 line of ^{87}Rb. Red (blue) lines depict laser light generated by the Ti:Sapph I (Ti:Sapph II) laser. Yellow lines are beams that originate from our diode laser, while the orange line shows the far red-detuned 1064 nm light from the dipole trapping laser. Taken from Ref [35].

combined with a Pound-Drever-Hall locking technique we are able to lock the laser to the $F = 2 \Longleftrightarrow F^{'} = 2, 3$ crossover resonance, with frequency control achieved using a double-pass acousto-optic modulator (AOM) setup. During the experimental sequence, Ti:Sapph I generates slowing and molasses beams, the depumping beam, and later a

resonant probe beam for imaging.

2.1.2 Ti:Sapph II

The rest of the 12.4 W of light from the Verdi laser is directed into another Ti:Sapphire laser we call Ti:Sapph II. It outputs about 1.5 W of power which then follows a daisy-chain AOM setup to generate the three beams used for the optical lattice. Red-detuned light (130 GHz) is chosen for trapping atoms during BEC production, whereas the transverse confinement for a 1D Bose gas is with a far blue-detuned lattice (772 nm). The dynamic tuning of the wavelength needed between these two stages of the experimental sequence is done using a programmable stepper-motor that rotates the birefringent filter in the laser cavity.

2.1.3 Dipole trapping laser

This laser primarily generates the beams we need for a crossed dipole trap. During most of my graduate career we used a 10 W 1064 nm laser source with a Nd:YVO4 crystal. Towards the late summer of 2020, an internal electronic issue rendered it unusable so we decided to upgrade to a 50 W fiber laser that we could use to generate additional beams for more uniform trapping. I will talk about upgrades in Chapter 6. For historical reasons, the 10 W source had been called the 'YAG' laser, but for the sake of simplicity I will refer to it as the dipole trapping laser.

During the experiment, we need the ability to dynamically change the intensity of the beam, very quickly in some instances, for example for a sudden trap quench. For

intensity control we pass the light through a setup consisting of electro-optic modulators (EOMs) combined with polarization optics (see Ref [29] for a detailed discussion).

Later in the path, the intensity-tuned beam passes through an acousto-optic tunable filter that acts as a beam splitter while also giving the deflected beam a frequency shift. These two beams then get focused into the chamber from the x- and y- directions and intersect at the atoms' position, forming the crossed dipole trap.

2.1.4 Diode laser

We generate our optical pumping and repumping beams using a homemade diode laser in an extended cavity Littrow configuration. The frequency of this laser is locked to the $F = 1 \Longleftrightarrow F^{'} = 1, 2$ crossover resonance using saturation absorption spectroscopy in a Rb cell. From then on, AOMs provide the frequency shift needed for the optical pumping and repump beams to be resonant on the $F = 1 \Longleftrightarrow F^{'} = 1$ and $F = 1 \Longleftrightarrow F^{'} = 2$ transitions respectively.

2.2 The vacuum chamber

Cold atom experiments require an ultra-high vacuum (UHV) environment to keep the system isolated from the surrounding atmospheric conditions. In our system we use a stainless-steel vacuum chamber that has a main section and an oven section that are separated by an 'intermediate' chamber and an 8-inch long tube.

The oven chamber contains an ampule of solid ^{87}Rb, and is heated by current-carrying

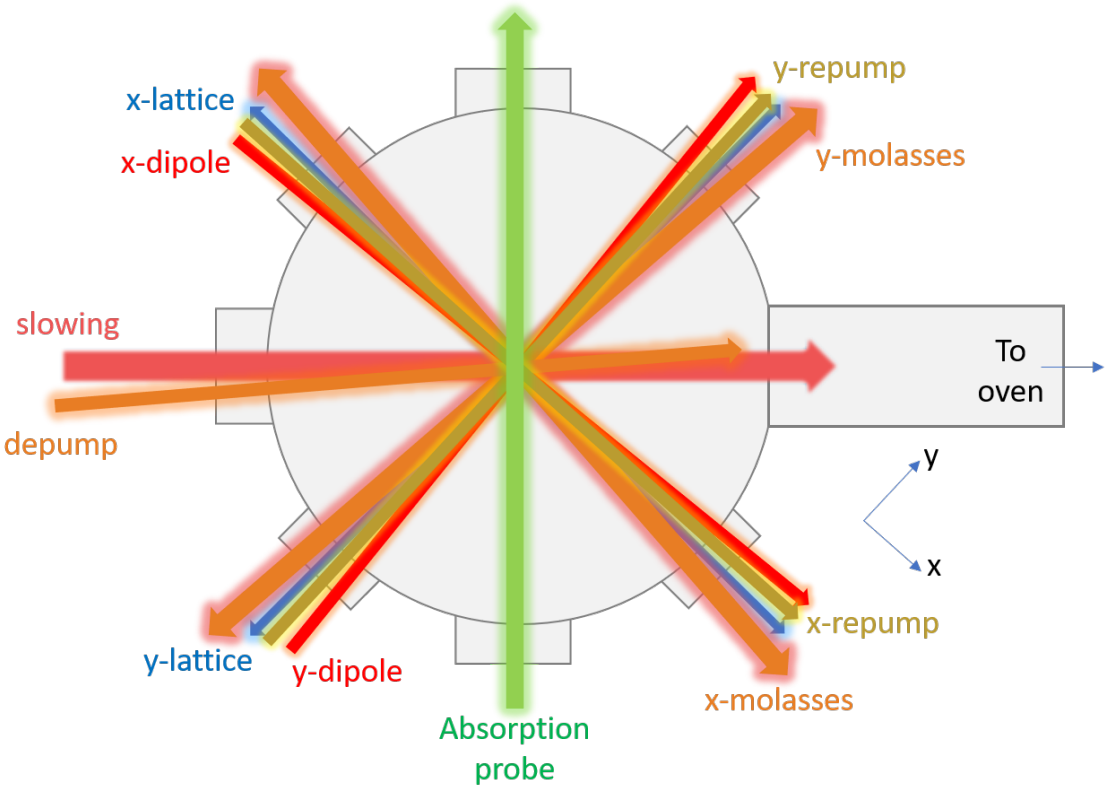

Figure 2.2. Top view schematic of the vacuum chamber. The atomic beam originates from the right and makes its way into the center of the chamber. Slowing and depumping beams enter through the window on the left. The molasses beams, dipole trap beams, lattice beams and repump beams enter the chamber from the windows along the diagonals of the figure. The absorption probe beam for imaging enters through the window at the bottom, exits at the top and into the imaging system.

coils. The coils keep the temperature of the 'oven' at the back and 'nozzle' at the front at 75° C and 139° C respectively. The heated up Rb forms an atomic vapor that passes through a microcapillary array and into the main chamber in the form of an atomic beam.

Seven windows on the main chamber act as input ports for the many beams that enter the chamber over the course of an experimental sequence (see Figure 2.2 for a schematic of the chamber). Not shown in the figure are the z-lattice beam, z-molasses beam, optical pumping beam, all of which propagate along the direction perpendicular

to the page. Furthermore, we are able to do absorption imaging in the vertical direction as well as the horizontal direction, and for that a probe beam enters from the bottom of the chamber.

Further details about the vacuum chamber are discussed in Ref [29].

2.3 Magnetic field generation

Around the main vacuum chamber, we have several sets of current-carrying coils that are used to generate the necessary magnetic fields for the experiment. A pair of 'MOT' coils in an anti-Helmholtz configuration generate a field gradient in the vertical direction during the experimental sequence. Additionally, we have three sets of Helmholtz coil pairs that are used to generate bias fields of up to 6 Gauss in each of the three cardinal directions. We use these to cancel out Earth's field and any residual unwanted fields in the lab.

2.4 BEC production

All our experiments start by slowing atoms in the atomic beam using a chirped slowing technique [40, 41] and loaded into a 3D magneto-optical trap (MOT) formed by the three retroreflected, orthogonal molasses beams. After several seconds of loading, the MOT reaches its steady-state size. At this point we compress the MOT, turn off the molasses beams and magnetic fields and load the atoms in a 3D optical lattice. The three $\sim$130 GHz red-detuned lattice beams trap atoms at individual sites in the optical

lattice. We then perform polarization gradient cooling (PGC) in the lattice to cool the atoms below the Doppler limit, using the same molasses beams as for the MOT.

Next, we compress the atom cloud in both the vertical (z) direction and horizontal (x and y) directions by alternatively turning off the lattice in those respective directions, letting the cloud collapse in the remaining trap, turning back on the full 3D lattice, and PGC cooling the atoms [42]. Following a final PGC step, we optically pump the atoms into the $F = 1, m_F = 1$ magnetic sublevel which allows them to be levitated by a magnetic field gradient of 30 G/cm. The lattice is then shut off adiabatically, resulting in an atom cloud with a temperature of less than 900 nK.

The final step involves pushing the phase-space density to above the threshold required for a Bose-Einstein condensate. This is done by first loading the levitated atom cloud into an overlapped compressible crossed dipole trap formed when the beam waist is $\sim$300 μm. A movable lens mounted on a translation stage allows the beam waist at the point of crossing to be dynamically changed down to $\sim 55\mu$m. We adiabatically ramp down the intensity over several seconds, forcing evaporation of the most energetic atoms. During the first 800 ms, we also compress the trap by adjusting the lens position. Doing this greatly increases the atomic density and lets the atoms collisionally thermalize, so as to keep the thermal tails populated to evaporate efficiently. The end result of the optimized evaporation sequence is a nearly pure BEC with a $> 95\%$ condensate fraction.

2.5 Creating a bundle of 1D Bose gases

Starting from the BEC, we adiabatically ramp up a 2D optical lattice made of the same x- and y- lattice beams, whose wavelength has been shifted to 772 nm during evaporative cooling. The blue-detuned lattice allows the atoms to be trapped at intensity minima in a 2D array of 1D 'tubes' (see Figure 2.3). The lattice is ramped up in 165 ms in 4 linear segments to a final depth of 40 E_r. Here $E_r = \frac{\hbar^2 k^2}{2m}$ is the recoil energy, where $k = \frac{2\pi}{772\ nm}$ is the lattice wavevector and m is the mass of a ^{87}Rb atom. The series of ramps is chosen to minimize breathing excitations as the system transitions from 3D to 1D, where it will not thermalize because it is a nearly integrable Lieb-Liniger gas. Empirical optimization of the ramps has been done, and is described in Ref [29].

With a blue-detuned 2D lattice, there exists a weak anti-trap for the atoms along the z (axial) direction. This does not significantly affect the overall trapping when the dipole trap is factored in, but it becomes relevant when we need a flat potential for a rapidity measurement (I'll talk more about it in Chapter 3). However, the dipole trap does not provide uniform confinement across the atom cloud. The 55 μm dipole trap waist is much smaller than the $\sim$430 μm lattice beam waist. Therefore, all occupied tubes experience very nearly the same transverse confinement, but the axial depth can vary as much as 28% across the cloud for the experiments discussed in this thesis. It is therefore a challenge to identify exactly how atoms have distributed among tubes. For simulations of the experiment, particularly those involving the calculation of rapidities after a trap quench, it is crucial to know the starting atom distribution because the

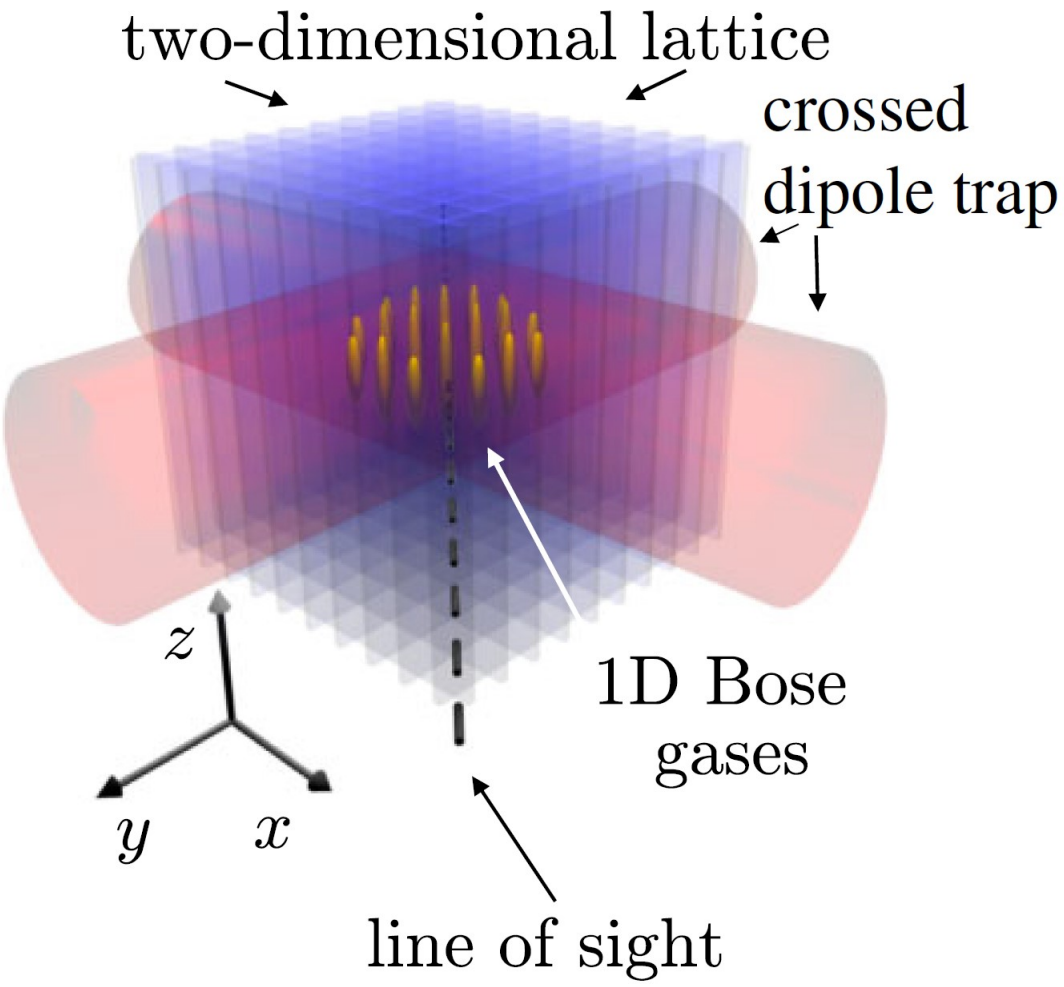

Figure 2.3. Our 1D Bose gas system in a 2D optical lattice. Atoms initially in the crossed dipole trap (red beams) are loaded into a blue-detuned lattice that restricts motion to 1D. The large size of the lattice beams compared to the dipole trap ensures that that transverse confinement for all the 1D tubes is essentially identical. Note: There are on the order of thousands of tubes in the actual setup, but only a few are shown here to illustrate the point.

behavior of the rapidity energy is highly sensitive to that initial condition. To obtain an empirical measurement of the atom distribution, we use the measured energy along with the total atom number and the fully known 3-dimensional trap geometry. This process is outlined in Chapter 4.

Additionally, because different tubes have different atom numbers, the interaction

parameter γ varies not only within each tube but also between tubes. Naturally, it is convenient to assign an average value of γ to the 1D Bose gas array once the population in each tube is known. Recalling that locally in a single tube, $\gamma = \frac{2}{n|a_{1D}|}$ where n is the 1D density and $|a_{1D}|$ is the 1D scattering length, we can calculate a weighted average as follows. The average γ for each tube is

$$\overline{\gamma_i} \equiv \frac{\int_{-R_i}^{R_i} \gamma_i(z) n_i(z), dz}{\int_{-R_i}^{R_i} n_i(z), dz} \tag{2.1}$$

where R_i is the length where the density reaches zero. The denominator is simply the number of atoms in the tube, N_i, while the numerator reduces to $\frac{4R_i}{|a_{1D}|}$. The weighted average over tubes is then written as

$$\overline{\gamma} = \frac{1}{N_{tot}} \sum_i \overline{\gamma_i} N_i = \frac{4}{N_{tot}|a_{1D}|} \sum_i R_i \tag{2.2}$$

Here, N_{tot} is the total atom number and the sum is taken over populated tubes. It is often helpful to quote both weighted average and the minimum γ in the central tube (where the largest density in the cloud occurs) to get a sense of the range of interaction parameters across the cloud. In the experiments discussed in this thesis, we produce a 1D Bose gas array with an initial average γ as high as 9, which is a good approximation for the Tonks-Girardeau limit, and as low as 1.4 which extends into the intermediate coupling regime.

2.6 The imaging system

Once the experimental sequence has ended and any pertinent time evolution has taken place, we measure the atomic cloud using absorption imaging. The imaging system works by passing an absorption probe beam along the 45-degree line-of-sight through the atomic cloud (see Figure 2.3). The shadow cast by the atoms is detected by a camera CCD.

To prevent any ambient light being measured as part of the atom signal, we first take an image with no probe beam (A). Then, for any given measurement we have the probe light on and we take both an image with the atoms (B) and another without them (C). Taking the ratio of the intensities of $\frac{(C-A)}{(B-A)}$ yields the atomic density which we can then use in the image analysis.

Even after this ambient background subtraction, there often remains a high-spatial-frequency background signal in the resultant image that arises from weak interference patterns on the probe beam between the time images B and C are taken. Filtering out these fringes is done using a Principal Component Analysis algorithm, and will be discussed in Appendix A [42].

Chapter 3

Momentum and rapidity measurements after a trap quench

3.1 The Bose-Fermi correspondence

As mentioned earlier, the Lieb-Liniger model can be exactly solved, and the system can be described in terms of emergent quasiparticles. The momenta of these quasiparticles are referred to as the rapidities. The Bose-Fermi correspondence shows that the local properties of a Tonks-Girardeau gas are the same as for a non-interacting Fermi (NIF) gas, as follows from Equation 1.3. Even though the momentum distribution of the two are quite different, the rapidity distribution of the Tonks-Girardeau gas turns out to be the momentum distribution of a NIF gas in the same initial trap. Due to the mapping between the two systems, the particles' momenta in the latter are conserved, and so they are also the rapidities of the system.

Things get more complicated when there is an external potential. The quasiparticle

momenta are no longer conserved, but there is still a set of conserved quantities used to constrain the GGE. In our experimental setup for example, we do not have a flat trap; the crossed dipole trap that is used to provide weak confinement along the axial (1D) direction breaks the integrability of the Lieb-Liniger gas [18] by allowing diffractive 3-body collisions to occur. These collisions result in an outgoing set of momenta that are different from the incoming momenta, eventually leading to thermalization. So for times shorter than the diffractive collision timescale, the aforementioned set of quantities can be considered conserved and the quasiparticles do not decay on these short timescales.

Since quasiparticles arise from interactions among particles, if a trapped Lieb-Liniger gas is allowed to expand in one dimension until interactions vanish, the quasiparticles eventually become the bare particles and their momentum distribution asymptotically approaches the distribution of rapidities [43–47]. In the Tonks-Girardeau limit, this phenomenon is called dynamical fermionization. It was predicted more than 15 years ago and its generalization to 1D expansion at arbitrary γ can be exploited experimentally to directly measure rapidities.

In Figure 3.1, the simulated evolution of a Tonks-Girardeau gas is shown after turning off the initial harmonic confinement. Its momentum distribution, which starts out sharply peaked, rounds out with time and slowly asymptotes to the momentum distribution of a NIF gas in the same initial trap.

We demonstrated this experimentally in 2019 [5]. To do so we started with an equilibrium Lieb-Liniger gas close to the Tonks-Girardeau limit in an approximately harmonic trap. By suddenly turning off the trapping, the momentum distribution evolves

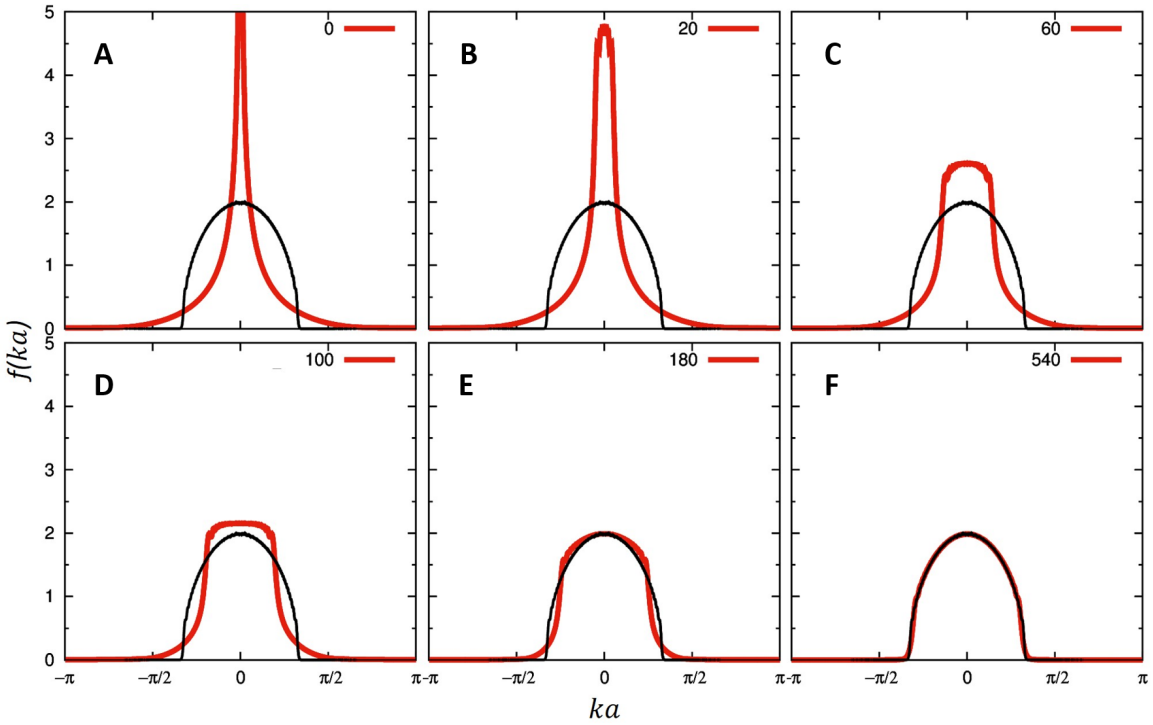

Figure 3.1. Dynamical fermionization of a Tonks-Girardeau gas, as calculated by theory. The simulation is done on a fine-spacing lattice along the 1D direction, along with a superimposed harmonic potential [44]. After the sudden removal of the harmonic confinement, the red curves show the evolution of the momentum distribution of the gas. The momentum axis is in units of inverse lattice spacing. The shape progresses from panels A to F, with the time label on the top right of each panel (in units of $\hbar$ divided by the tunneling amplitude). Asymptotically, the shape of the momentum distribution becomes that of a non-interacting Fermi gas (black) in the same trap (shown in panel F).

due to interactions and reaches a shape that is consistent with theoretical calculations of the rapidity distribution. I will describe this measurement in this chapter, and further discussions can be found in Joshua Wilson's thesis [29].

3.2 Making a momentum measurement

In order to measure the momentum distribution, we use a time-of-flight (TOF) approach in our system. Most variations of this method involve releasing atoms or particles from

some trap and measuring their spatial distribution after a fixed TOF. From this one can extract information about the atoms' initial momenta from the TOF distribution. A clean TOF measurement of the momentum distribution requires that the initial spatial spread of the atomic distribution be much smaller than the size of the TOF distribution. This way the broadening due to the initial size is small and the momentum-to-space mapping is good.

After we turn off the axial trapping to observe dynamical fermionization we look to measure the instantaneous momentum distribution at variable evolution times. To ensure that the momentum evolution does not get affected by interactions during the measurement itself, we need to turn off interactions quickly whenever we initiate a momentum measurement. We minimize the effect of interactions by shutting off the 2D optical lattice. Turning off the initially tight transverse confinement causes the atomic cloud to expand rapidly transversely, much faster than expansion in the relevant axial direction, as shown in Figure 3.2. At this point we face a number of experimental limitations. First, the transverse field-of-view of the camera prevents us from using a TOF longer than 70 ms for our chosen lattice shutoff speed. Second, the magnetic field gradient keeping the atoms levitated against gravity is not sufficiently uniform more than a few hundred μm away from the center of the trap, and the atom cloud starts to sag at large transverse distances. The amount of sagging Δz is a sharply increasing function of transverse distance r from the center ($\Delta z \propto r^4$), so we cannot allow transverse expansion for long distances. The optimization of the lattice shutoff to suppress this limitation is discussed in [29].

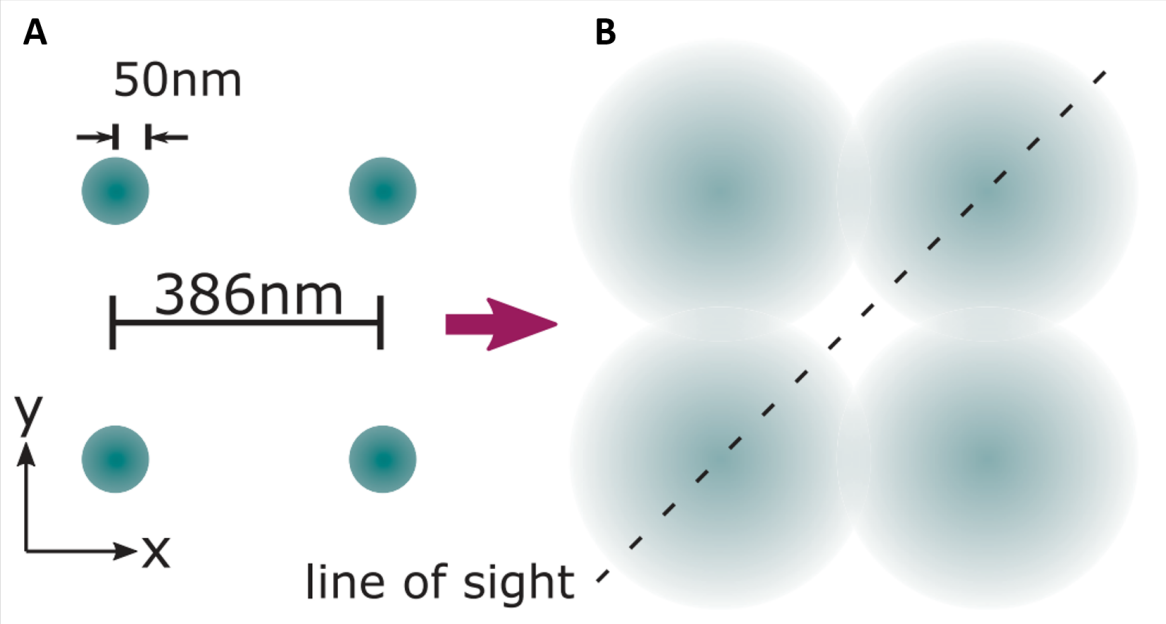

Figure 3.2. Top view of a zoomed-in section of the 1D Bose gas ensemble. The 2D optical lattice confines individual gases over a 50 nm width, separated by half the lattice wavelength, as shown in (A). When a momentum measurement is initiated, we turn off the lattice rapidly. As a result there is transverse expansion (B) which reduces interactions greatly.

3.3 Cancellation of the lattice anti-trap

When atoms are trapped in a blue-detuned 2D lattice, they experience a slight anti-trap, or a potential with a negative curvature. Due to the Gaussian beam shape, both the retroreflected x- and y- lattice beams produce a deeper transverse confinement in the center of the beams than towards the edges. Therefore, the energy of the vibrational ground state decreases as you move away from the beam center along the axial direction. The result is an effective 'anti-trapping potential' which is inherent to a blue-detuned lattice.

The anti-trap is a small correction which needs to be present in all calculations involving the 1D trapping potential, and must be accounted for in the modeling of the

experiment. It is naturally Gaussian in shape, but has a width that is much larger than the dipole trapping potential, so we approximate it in the region of the dipole trap as a harmonic potential with a negative spring constant.

As mentioned before, a rapidity measurement requires expansion in a flat potential before making a momentum measurement. We therefore keep on a shallow dipole trap with a curvature that is positive but equal to the anti-trap, resulting in a combined potential that is approximately 'flat' over a 30 μm range. The calculation of the appropriate dipole trap depth is discussed in detail in Joshua Wilson's dissertation [29].

3.4 Dynamical Fermionization: a prototype rapidity measurement

For the first ever measurement of rapidities in a quantum system, we start out with a total of $N \sim 10^5$ atoms in a bundle of 1D Bose gases, giving a gas with an average coupling parameter $\gamma \approx 8$ and a minimum $\gamma \approx 4.2$ at the center of the central tube. The combined trap has an effective axial trapping frequency of $\omega_{eff} = 18.1 \pm 0.36$ Hz. At $t = 0$ we almost completely turn off the axial trap, allowing dynamical fermionization in a nearly flat potential. Details about the timing sequence are explained in [29], so I will not reiterate them here.

We integrate the raw images transversely to extract the axial TOF distributions, shown in Figure 3.3. The initial bosonic distribution broadens quickly and becomes rounded over the first few milliseconds. By $t_{ev} = 15$ ms the shape of the distribution has

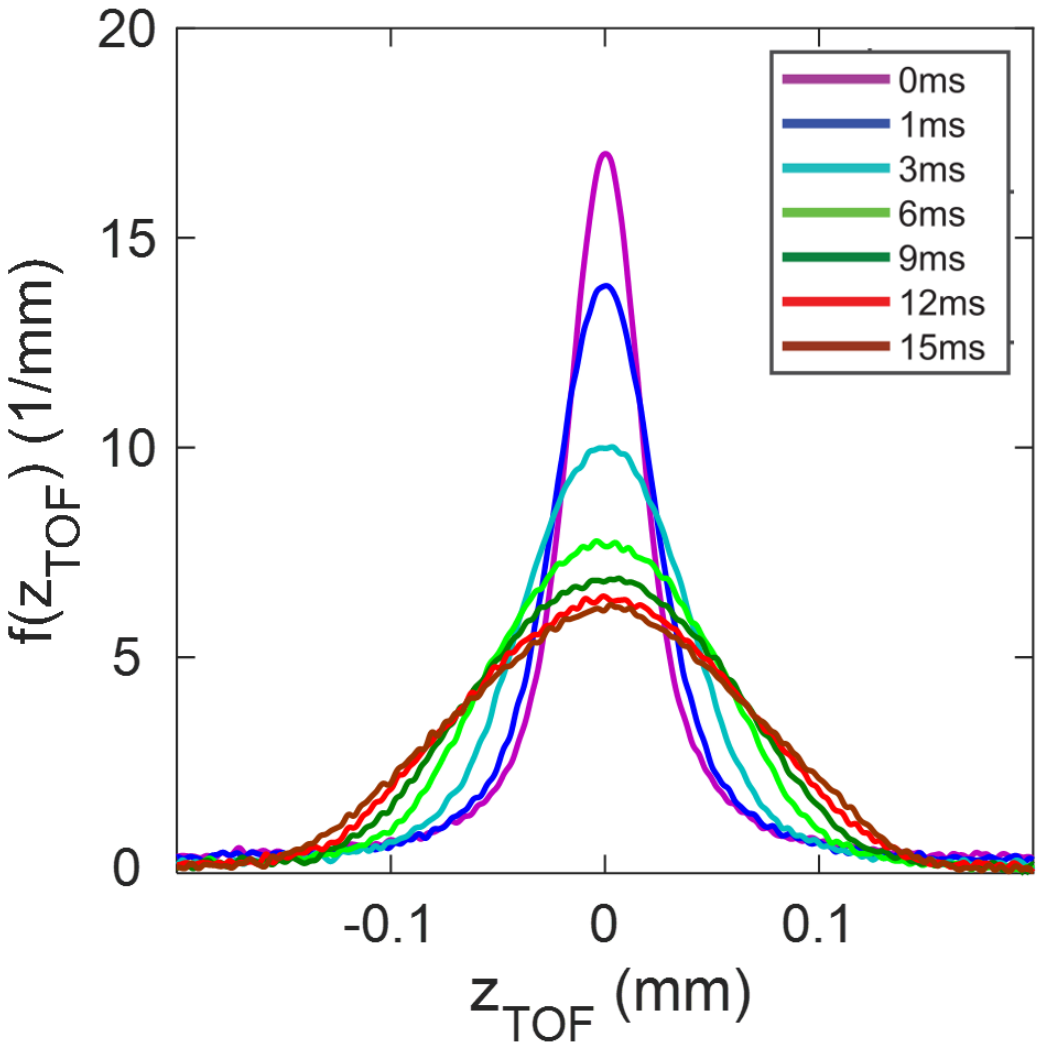

Figure 3.3. Momentum distributions after variable times after quenching to a flat potential. The distribution starts out bosonic in shape and transforms over time, demonstrating dynamical fermionization. The shape asymptotes by 15 ms. Adapted from [5].

essentially asymptoted to a fermionic shape, indicating that dynamical fermionization is complete and that the distribution of rapidities has been measured. We stop making measurements past this because by this time the axial spatial extent of the cloud has reached the end of the range of our flat potential.

To show that the asymptotic distribution is in fact the distribution of rapidities, we

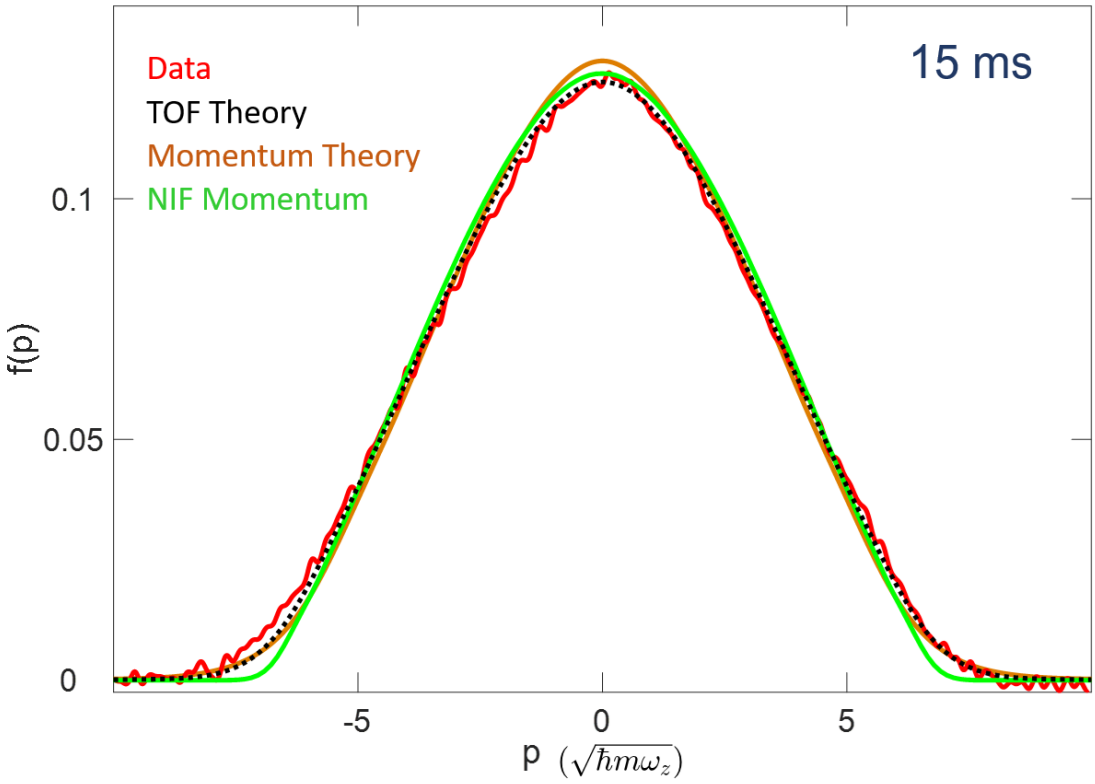

Figure 3.4. Comparison of the $t_{ev} = 15$ ms asymptoted momentum distribution with theory curves. That the dashed black curve agrees with the data shows that the experiment is captured by hard-core boson theory. Since the orange curve overlaps as well, it shows that that TOF distribution is a good measurement of the momentum distribution. Finally, the green curve, which is the rapidity distribution for a NIF or a Tonks-Girardeau gas, agrees with the data, demonstrating that we in fact have observed dynamical fermionization. Adapted from [5].

compare our experimental results at $t_{ev} = 15$ ms with three hard-core boson theory calculations, shown in Figure 3.4. The agreement among the four curves in the figure validates our measurement of the rapidity distribution in the following ways. The fact that the TOF theory curve (black dashed line) is close to the momentum theory (solid orange line) shows that our time-of-flight scheme measures the momentum distribution. The experimental data curve (solid red line) is also close to these two, suggesting that we do indeed measure the asymptotic momentum distribution. To the extent that we are

in the Tonks-Girardeau limit, the NIF gas momentum (solid green line) is the rapidity distribution and it is remarkably close to the other three curves, suggesting that we have performed a good rapidity measurement. There is, however, some discrepancy is in the tails, where the data and the simulated curves don't quite agree with the NIF momentum.

Recall that a good measurement of the rapidities requires giving up interactions via 1D expansion. Once the atom cloud has expanded quite a lot compared to its starting size, it becomes more and more difficult to reduce interactions because the cloud is so sparse. While the momentum distribution has mostly fermionized by $t_{ev} = 15$ ms, the 1D density has not reduced enough for the highest momentum components to fermionize. Calculations for a single tube show that ∼100 ms of 1D expansion time, much longer than we we have access to, is required before the momentum distribution closely matches the NIF momentum curve at the tails.

3.5 Quench to a deeper or shallower trap

If a gas is instead quenched to a trap with a different trap frequency, theory at $\gamma \longrightarrow \infty$ has predicted there to be oscillatory behavior in the momentum distribution. The system responds to the sudden change in the potential, causing the cloud to undergo breathing oscillations spatially. For a Tonks-Girardeau gas the momentum distribution changes shape from initially bosonic to fermionic, then back to bosonic, every half-cycle, with a scale factor $r = \omega_f/\omega_i$ that is the ratio of the final and initial trapping frequencies (see

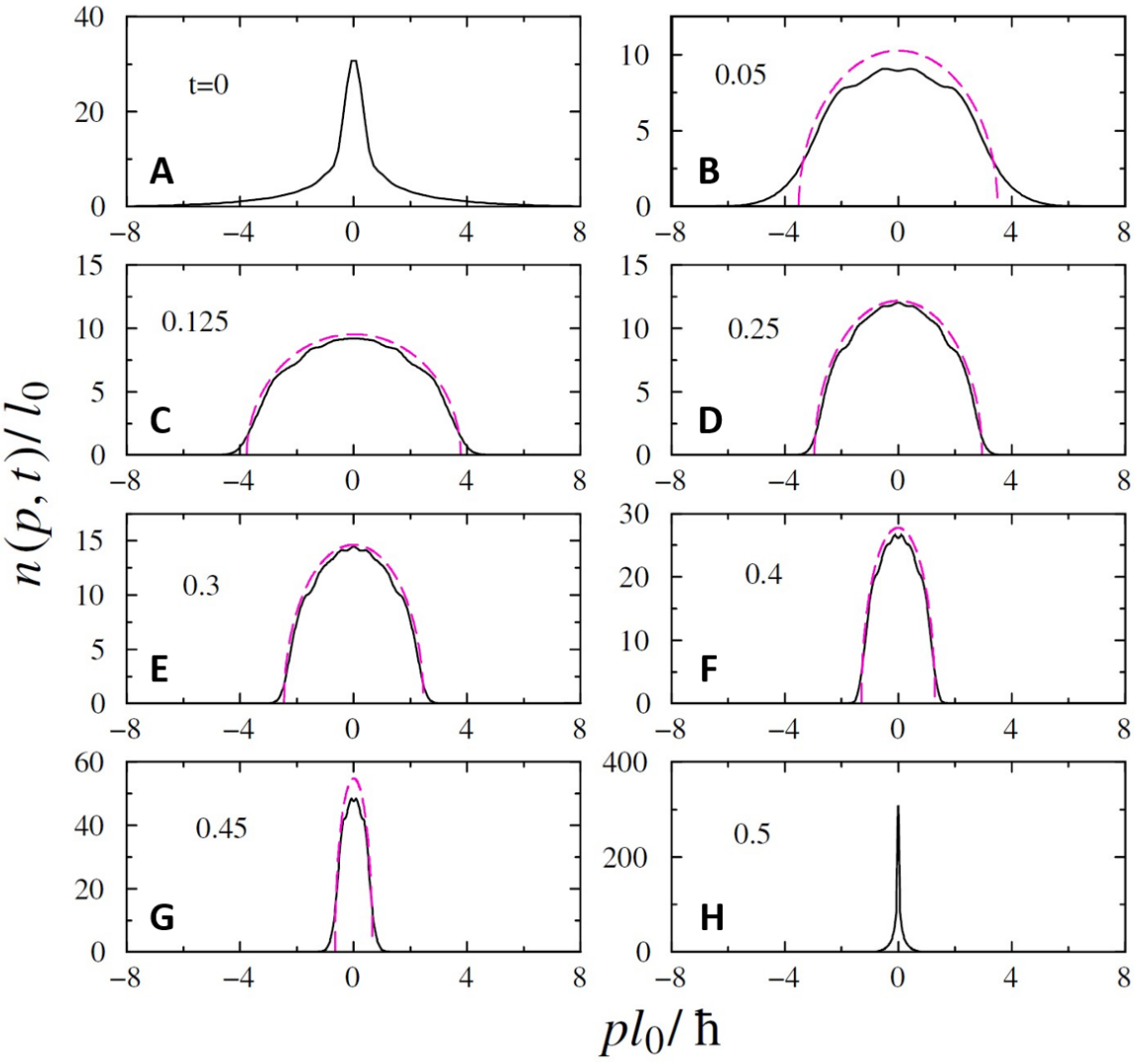

Figure 3.5. Momentum distribution evolution of a 1D Bose gas after quenching to a trap that has a 10x smaller trap frequency. In the half cycle shown, the initial broadening is rapid (panels A-C), and roughly acts like dynamical fermionization, as the distribution (solid black line) reaches a fermionic shape (dashed purple line). At half cycle in the new trap (panel H), the momentum distribution returns to a bosonic shape, but rescaled by a factor of the ratio of initial to final trap frequencies. Later it reverses this process and retains its initial shape at full cycle. Taken from [45].

Figure 3.5).

We observed these Bose-Fermi oscillations in the work that was published in Ref [5], where we quench the trap to both 10x deeper and 3x shallower and track the changing

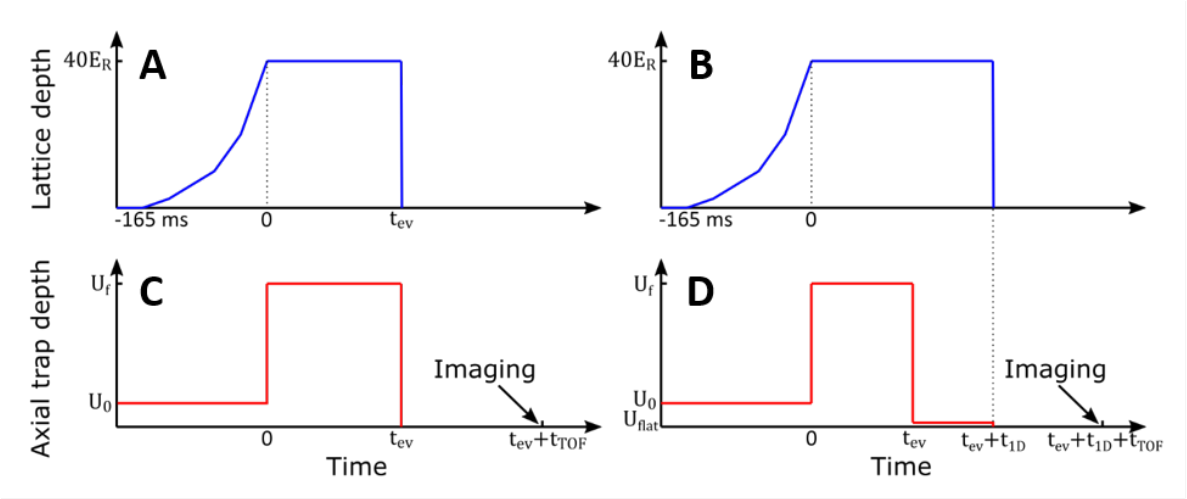

Figure 3.6. Timing diagrams for momentum (A,C) and rapidity measurements (B,D). A momentum measurement is performed by allowing free space expansion after an evolution time t_{ev} in the deeper trap (panels A,C). The image is taken after an appropriate TOF after expansion. To measure the rapidities we need some 1D expansion (panel D) for the instantaneous momentum distribution to fermionize into the rapidity distribution. Hence the 2D lattice is kept on for a time t_{1D} after t_{ev}, and then turned off before a TOF measurement (panel B).

shape of the momentum distribution of our 1D system as it cycles through bosonic and fermionic. Theory calculations in the Tonks-Girardeau limit replicate the qualitative features of the evolving distributions, even though the system does not experimentally stay in that regime throughout the cycle. A more careful discussion can be found, again, in Ref [29].

In the experiments pertinent to this thesis, we instead focus on measuring the rapidity evolution after similar trap quenches. Evolution starts at t=0 after the trap quench, which is a sudden increase of the dipole trapping beam intensity (see Appendix C for details on how we set up the quench). After a variable evolution time t_{ev}, we measure the momentum distribution by turning off all traps as described earlier in the chapter. The rapidity measurement is done by turning off the trap almost completely and creating a flat potential for 1D expansion.

Once the cloud edge reaches the end of the flat potential (the 1D expansion time t_{1D} that is needed varies from as long as 15 ms to shorter than 1.5 ms, depending on the evolution time during the quench), we measure the momentum distribution using the technique described earlier, knowing that it has evolved into the rapidity distribution. For each t_{ev} we choose an appropriate TOF long enough such that: 1) All atoms are contained in the CCD field-of-view, and 2) the atom signal in the image is not small enough to be buried in the noise. Since the axial cloud size is always smaller or equal to what it was for the first ever rapidity measurement in dynamical fermionization, all momentum measurements here are at least as good as that one.

Chapter 4

Theoretical Setup

4.1 Modeling the initial state and the quench

Before implementing GHD to simulate our experiments, we first need to calculate the initial state before the quench. Each 1D gas tube in the ensemble contains an independent gas obeying the Lieb-Liniger Hamiltonian plus an external trapping potential term. However, because of the intensity profile of the crossed dipole trap, each tube has a different trapping potential that needs to be taken into account to find the initial state as well as to compute the dynamics. The combined potential is the sum of the dipole trap beams propagating along the x and y directions and the approximately harmonic blue-detuned lattice anti-trap along z. The axial potential felt by the atoms at a tube l with position (x_l, y_l) in the 2D array of gases is

$$U_l(z) = U\left[1 - \frac{1}{2}\left(e^{-\frac{x_l^2}{2W^2}} + e^{-\frac{y_l^2}{2W^2}}\right)e^{-\frac{z^2}{2W^2}}\right] - \frac{1}{2}m\omega_{at}^2 z^2 \tag{4.1}$$

where U and W are the amplitude and width of the Gaussian trap, and ω_{at} is the anti-trap spring constant.

Depending on the initial condition, we use dipole trapping beams, each with 36 mW or 2.5 mW of power, corresponding to an axial trap depth of $U = 19.39\ E_r$ or $U = 1.195\ E_r$ for intermediate or strong coupling respectively. The measured size of the beam waist is $W = 55.2\ \mu$m and $\omega_{at} = 41.6\ s^{-1}$ for our 2D lattice depth of 40 E_r. For either starting trap geometry, we use the total measured atom number at time t, $N_{tot}(t)$, to calculate the number of atoms in each 1D tube, $N_l(t)$. We do this by first assuming that atom loading into the 2D lattice is adiabatic and therefore that the system starts and remains in the ground state. With the assumption of a constant chemical potential across the 2D tube array, we determine a critical depth U_{2D}^* at which the 3D system is assumed to decouple into individual tubes. This depth is such that the tube numbers $N_l(t)$, calculated for the chemical potential using the exact Lieb-Liniger ground state solution [12] add up to $N_{tot}(t)$. Details of the ground state calculation and atom numbers are discussed in Appendix D. Our assumption of the system decoupling into independent tubes at a fixed depth works well, even though in reality each tube decouples at a slightly different depth.

Using U_{2D}^* as a free parameter, we simulate the experiment for integer values of U_{2D}^* and compare the rapidity energies to the experimentally measured ones. We minimize the least-squares difference between the two for a set of time steps near the maximal compression point of the first cycle in the evolution for both quenches (see Figure 4.1). The 'optimal' value of U_{2D}^* is then used to calculate the transverse atom number distributions in each case; we find that they are consistent with both the experimental measurements

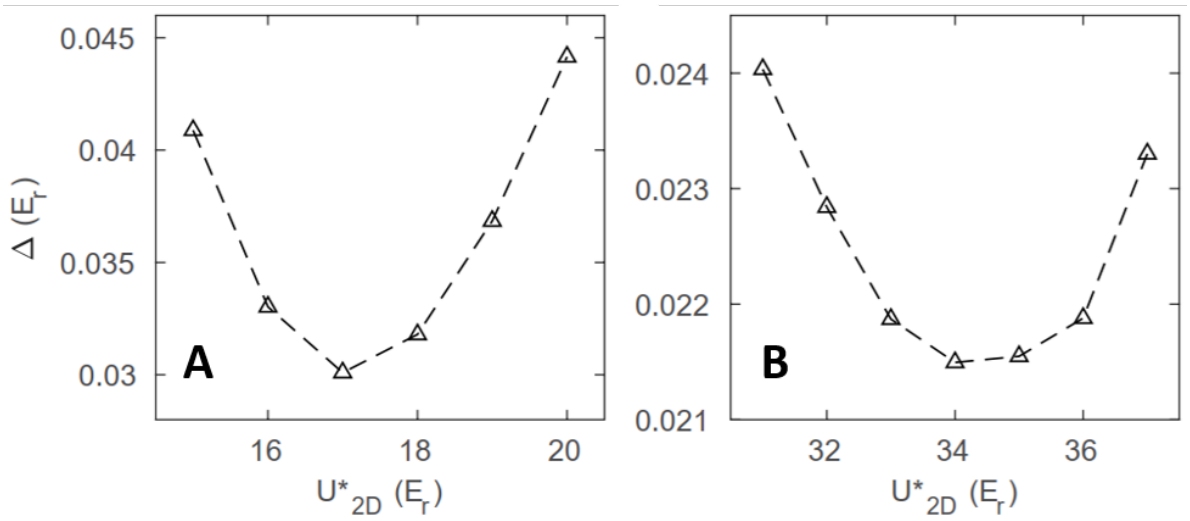

Figure 4.1. Least-squares differences for experimental and theoretically calculated rapidity energies. In panel A, as a function of the decoupling depth U^*_{2D}, the RMS difference is plotted for the intermediate coupling initial condition for seven time points around the energy maximum in the first cycle. Panel B shows the difference for the strong coupling condition, but for six points around the first cycle energy maximum.

and are close to 2D projections of 3D Thomas-Fermi distributions (displayed in Figure 4.2). As seen in the plots, the experimental distributions are slightly asymmetric towards the edges, with ripples that can drop below zero. The asymmetry may in part be due to non-cylindrically-symmetric transverse trapping, but some of the asymmetry and all of the ripples are a measurement artifact.. The measurement is done by loading atoms in the 2D optical lattice and taking an image after 15 ms of 1D expansion after the axial trapping is shut off. Even after the expansion, the atomic density remains high enough that atoms cause some lensing of the probe absorption beam, as evident in the ripples near the edge of the distributions. Although the ripples are greatly reduced by the letting the atoms expand before imaging, they do not wholly disappear.

When modeling the experiment, we take the trapping potential as suddenly increasing from U_0 to U_f at t=0, although in practice there is finite ramp-up time for the depth

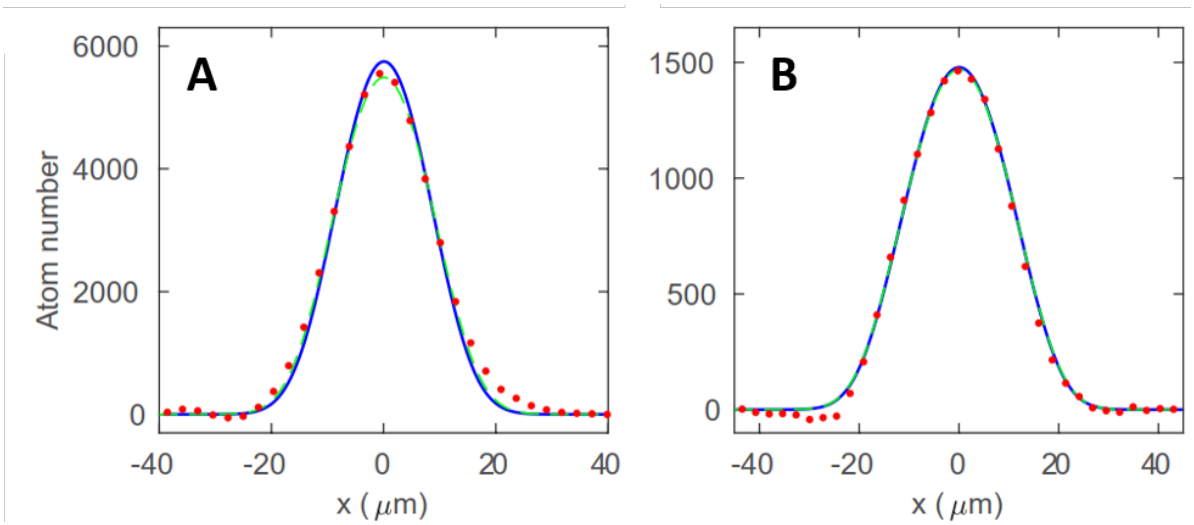

Figure 4.2. Transverse distributions of the 1D gas ensemble for both the intermediate (panel A) and strong (panel B) coupling conditions. Red points are from experimental measurements of the distributions. Solid blue lines are distributions computed using the optimal U^*_{2D} in Figure 4.1, convolved with our 4.8 μm instrumental resolution. Dashed green lines are the 1D projection of a 3D Thomas-Fermi distribution, where the Thomas-Fermi radius of 17 μm in panel A (22 μm in panel B) is obtained by fitting the red points in the range -13 μm to 13 μm.

(see Appendix C for details about the ramp). For the simulation of the 10x quench we use $U_f = 206.9\ E_r$ and a waist $W = 57.1\ \mu$m, whereas for the 100x quench we have $U_f = 125.7\ E_r$ and a waist $W = 55.2\ \mu$m The waist was slightly larger for the 10x quench due to refractive effects in the electro-optic modulators at high intensities.

4.2 GHD in our Lieb-Liniger gas ensemble

We solve the following GHD equation for each 1D tube in the system to model post-quench dynamics:

$$\partial_t n + v^{eff}\partial_z n = [\partial_z U(z)]\partial_\theta n \tag{4.2}$$

Within each spatial fluid cell, coupled hydrodynamic equations follow the evolution of the quasiparticle velocity distribution along with a Fermi occupation ratio $n(\theta, z, t)$ at a rapidity θ, for each point in space z and time t. The Fermi occupation ratio is the ratio of the density of quasiparticles to the local density of states. As illustrated in Figure 1.2, the effective velocity can be thought of as the group velocity of a quasiparticle with energy $\epsilon = \theta^2/2m$ and momentum $p = \theta$. Since we only consider evolution under a zero-entropy assumption, the Fermi occupation ratio can correspond to a single Fermi sea or multiple Fermi seas in θ [48], and can be written as

$$n(\theta, z, t) = \begin{cases} 1 & \text{if} \quad \theta \in [\theta_1, \theta_2] \cup \cdots \cup [\theta_{2q-1}, \theta_{2q}] \\ 0 & \text{otherwise,} \end{cases} \tag{4.3}$$

where q is the number of Fermi seas. The points $(z, \theta_i(z))$ form a closed loop in phase space at any given time t because the local state is a continuous function of position. Then, the GHD equation can be written as a parametric curve for the phase space trajectory for the 1D gas [49, 50]:

$$\frac{d}{dt} \begin{bmatrix} z_t(s) \\ \theta_t(s) \end{bmatrix} = \begin{bmatrix} v^{\text{eff}}(z_t(s), \theta_t(s), t) \\ -\partial_z U(z_t(s)) \end{bmatrix}. \tag{4.4}$$

We solve Equation 4.4 and approximate the phase space curve at 500 discrete points with a time step $dt = 0.1$ μs, so as to increment each point: $(z_s, \theta_s) \to (z_s + v^{eff} dt, \theta_s - \partial_z U dt)$. As the curve evolves, it folds onto itself, eventually creating a double Fermi sea for certain z values. At later times, additional Fermi seas can be seen. Examples of phase

space curves are shown in Figure 5.6 in Chapter 5. At early times, as long as there is a single Fermi sea, the dynamics can be mapped onto conventional hydrodynamics (if the right parameters are chosen), which uses the exact equation of state as the Lieb-Liniger model [49,51]. However, as soon as a second Fermi sea forms, conventional hydrodynamics predicts an unphysical shockwave, and to make accurate predictions from that time onward, the full GHD description is required [52].

4.3 Extraction of rapidity distributions and energies

We obtain the predicted rapidity distribution by integrating over the spatial (z) direction the local density of quasiparticles $\rho_l(\theta, z, t)$ in tube l:

$$f(\theta, t) = \frac{1}{N_{tot}(t)} \sum_l \int dz \rho_l(\theta, z, t) \tag{4.5}$$

Here, $N_{tot}(t)$ is the total measured atom number at time t and the sum is performed over all 1D gas tubes.

For a Lieb-Liniger gas, one can write the total energy density as

$$e = \int d\theta \rho(\theta) \frac{\theta^2}{2m} \tag{4.6}$$

where $\rho(\theta)$, the rapidity density, is the spatially integrated local density of states ρ_l [8]. One can show that in the thermodynamic limit $N \to \infty$, $L \to \infty$, the interaction energy

density e_I is [53]

$$e_I = \int d\theta \rho(\theta) \left[\frac{\theta}{m} - v^{eff}(\theta) \right] \theta \tag{4.7}$$

The kinetic energy density is $e_K = e - e_I$. Putting all of these equations together and performing a weighted average for our ensemble of tubes, we use the following expressions to compare experimentally measured energies:

$$E(t) = \frac{1}{N_{tot}(t)} \sum_l \int dz d\theta \rho_l(\theta, z, t) \frac{\theta^2}{2m} \tag{4.8}$$

$$E_I(t) = \frac{1}{N_{tot}(t)} \sum_l \int dz d\theta \rho_l(\theta, z, t) \left[\frac{\theta}{m} - v_l^{eff}(\theta) \right] \theta \tag{4.9}$$

$$E_K(t) = \frac{1}{N_{tot}(t)} \sum_l \int dz d\theta \rho_l(\theta, z, t) \left[v_l^{eff}(\theta) - \frac{\theta}{2m} \right] \theta \tag{4.10}$$

Chapter 5

Rapidity evolution after a trap quench

5.1 Quench to a 10x deeper trap

In Ref [5] we study momentum evolution after a trap quench and examine the shape of the distributions as they change from bosonic to fermionic and back over half a trap period. Our more recent work concerns GHD, which is instead able to follow the evolution of rapidities for our nearly integrable system. We extend our scheme previously used for an equilibrium rapidity measurement to a dynamical study of rapidities after quenching the trap. Doing so, we are able to test GHD by directly comparing experimental rapidity distributions to those calculated using GHD theory, and we will see that their shapes across the first couple of cycles are much more similar than the momentum distributions. The first such experiment we perform is initialized in the intermediate coupling regime with an average $\gamma \approx 1.4$ and a total atom number of $\sim N = 3 \times 10^5$, corresponding to about 60 atoms in a typical tube. At $t = 0$ we quench to a 10x deeper trap, letting the atoms evolve for t_{ev}, after which we measure the rapidity distribution.

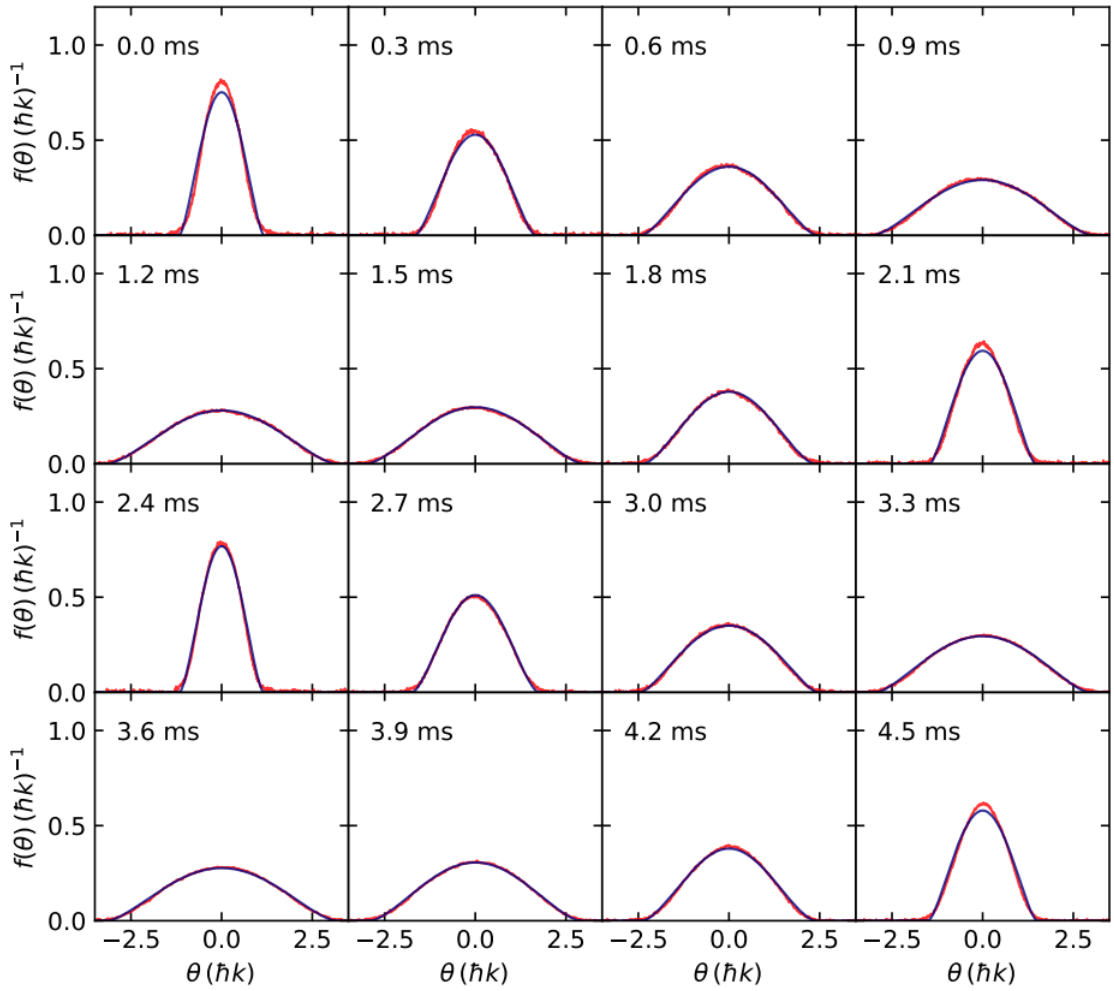

Figure 5.1. Rapidity profiles during evolution after the 10x quench. The rapidity axis θ is presented in momentum units of the lattice wavevector k, and the evolution time is displayed in the top left of each panel. Red (blue) curves show experimentally measured (theoretically calculated) distributions for the first two cycles. In order to account for day-to-day fluctuations, the calculations use different values for the trap depth (by about 2.7%) between the two cycles. All theory curves use the measured average atom number for that time.

Figure 5.1 shows the rapidity evolution for the 10x trap quench starting from the intermediate coupling starting condition. We conduct 15 runs for each time step and process each averaged profile to remove as much of the inherent low frequency background as possible. This is done by fitting the region outside the atom signal with a 4^{th} order polynomial and subtracting it from the entire signal (see Appendix E for details).

Initially, the quench results in a collapse of the cloud and as it gets denser, the many-body wavefunction reconfigures itself. The gas minimizes energy by converting some of the extra kinetic energy into mean-field energy throughout the collapse, meaning a change in the built-in correlations and therefore the coupling parameter. Later, as the gas rebounds the mean-field repulsion results in conversion to kinetic energy and the cycle repeats. During this 'breathing' the initial average γ of 1.4 reaches as low as 0.3, as the average axial cloud size ranges from 14 μm to 3 μm. We choose the size of the quench so the system stays 1D; that is, even when two of the most energetic atoms that start at the edge of the spatial distribution collide in the center, they do not have enough energy to excite one of them to the next even transverse vibrational level, which is the lowest energy even parity two atom state, which is about 20 E_r from the ground state. As seen in Figure 5.1 the agreement between theory and experiment is very good, suggesting that the dynamics are well-captured by GHD in this case.

Another way to compare the results is by looking at the extensive quantity – the average rapidity energies – extracted from the profiles. Details of error analysis are discussed in Appendix E. In short, we integrate the profiles to get the energy as follows:

$$E = \int f(\theta) \frac{\theta^2}{2m} d\theta \tag{5.1}$$

where $f(\theta)$ is the rapidity distribution. We plot energies for the first two cycles in Figure 5.2. At every point, the atom number measured for that time-step is used in the GHD calculation. The experimental rapidity energies match their theory counterparts, as one would expect given the agreement in the distributions. The two insets show

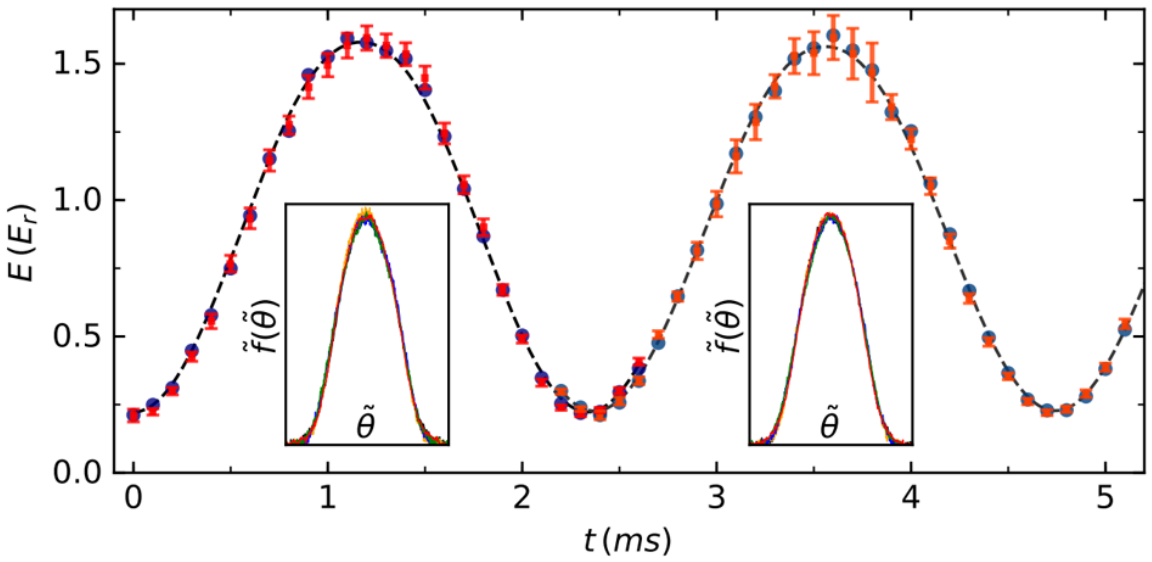

Figure 5.2. Rapidity energies after the 10x quench. The red/orange and dark/light blue points are experimental measurements and GHD theory respectively, with the measured atom number used at every point. The dashed line is GHD theory using the average atom number. Energies are computed by integrating the distributions (error analysis for the experimental points can be found in Appendix E). Insets contain rescaled rapidity profiles for the first and second cycle, and show that the shape is self-similar throughout this time.

rescaled rapidity distributions for the first two cycles. It is noteworthy that the shapes are self-similar, even though the momentum distributions change dramatically in shape, as demonstrated in Ref [5].

We also explore rapidity evolution at a later time, during the 11^{th} cycle. By this time the high densities during breathing lead to a $\sim 20\%$ atom loss from 3-body inelastic collisions, loss that is not incorporated into the model. The loss produces a discrepancy between theory and experiment that is noticeably large, in both the distributions and the energies.

Looking at panel E in Figure 5.3, we can see that at the maximum compression point the theoretical energy is higher than the experimentally measured energy. Atom loss happens disproportionately near peak compression when the densities are higher.

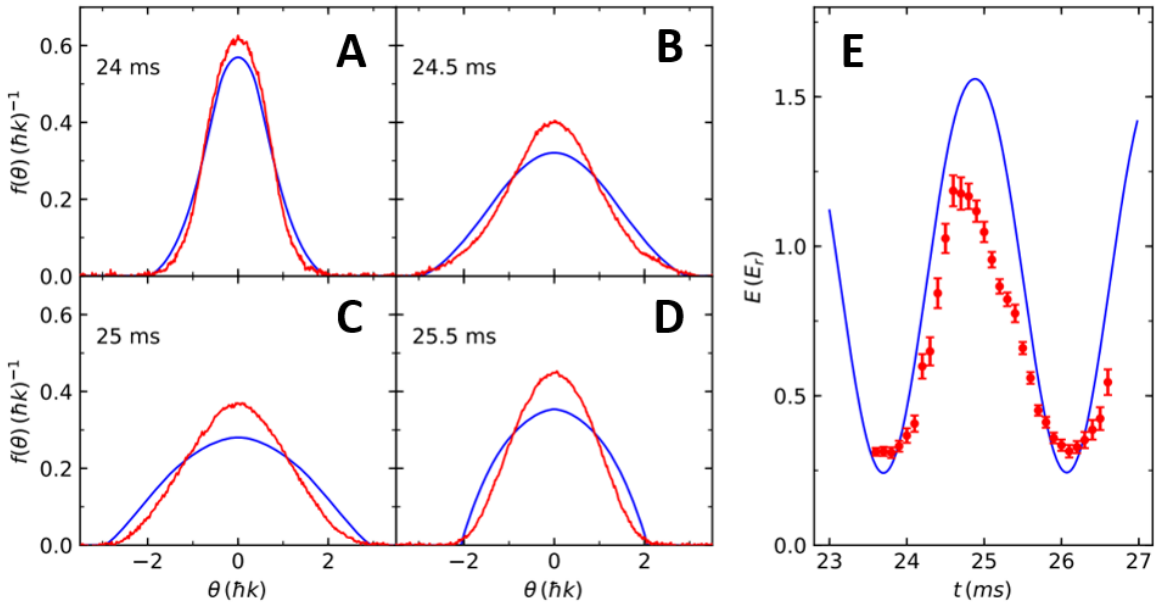

Figure 5.3. Rapidity evolution in the 11^{th} cycle after the 10x quench. In panel B, the trap depth used in GHD calculations has been adjusted to match the oscillation phase of the experimental energy curve, and an average atom number of 2.4×10^5 is used. In panels A-D, the corresponding experimental rapidity distributions for select points are shown in red, while theory is shown in solid blue. The discrepancy arises mostly from atom loss by the 11^{th} cycle, due to inelastic collisions at high density points in the oscillation.

Some of the energy added from the quench, which is partly stored as mean-field energy and partly as kinetic energy in the correlations, is lost as a result of atom loss. Near the energy peak, this results in a smaller amount of rapidity energy available for 1D expansion, which then manifests itself as a discrepancy near the local maximum. At the energy local minima, the situation is more subtle. The lost mechanical energy causes the gas to not spread out as far when it rebounds. The total energy (mean-field energy plus mechanical energy) is essentially constant over the cycle, but a smaller fraction of the energy is potential. The increase in available rapidity energy from the resulting smaller cloud size at peak expansion partially counteracts the loss of mechanical energy, and therefore the measured energy minima are not far from GHD theory. If we had studied

the spatial distribution, it would also exhibit a decrease in amplitude with the loss of mechanical energy over time.

5.2 Quench to a 100x deeper trap

In our main quench of study, we start with a gas in the strongly interacting regime, with an average γ of 9.3. With a total atom number of $\sim 1 \times 10^5$ and only about 11 atoms in a typical tube, this quench to a 100x deeper trap can be studied for tens of cycles with negligible loss. Rapidity profiles for the first two cycles are shown in Figure 5.4. Again, the agreement between GHD theory and experiment is remarkable considering that 1D Bose gases with such a small number of atoms can hardly be thought to be in the continuum limit of GHD [1]. We also compare these results to calculations in the Tonks-Girardeau limit to show the validity of GHD at low particle numbers; I will discuss this in Section 5.3.

In addition to the rapidities, we measure for the first two cycles the momentum distributions by turning off all trapping at once, granting us access to the kinetic energy evolution. During evolution after this very large quench, γ falls from 9.3 down to 0.4 which is well in the intermediate coupling regime, while the atom cloud compresses from 17 μm to a size of 0.5 μm. The spatial evolution calculated using GHD is described in Appendix F.

We compare energies between GHD theory and experiment in Figure 5.5. The

[1] As I'll mention later, rapidity distributions for small particle numbers have high-spatial-frequency oscillations, which are averaged out by averaging over tubes with different numbers.

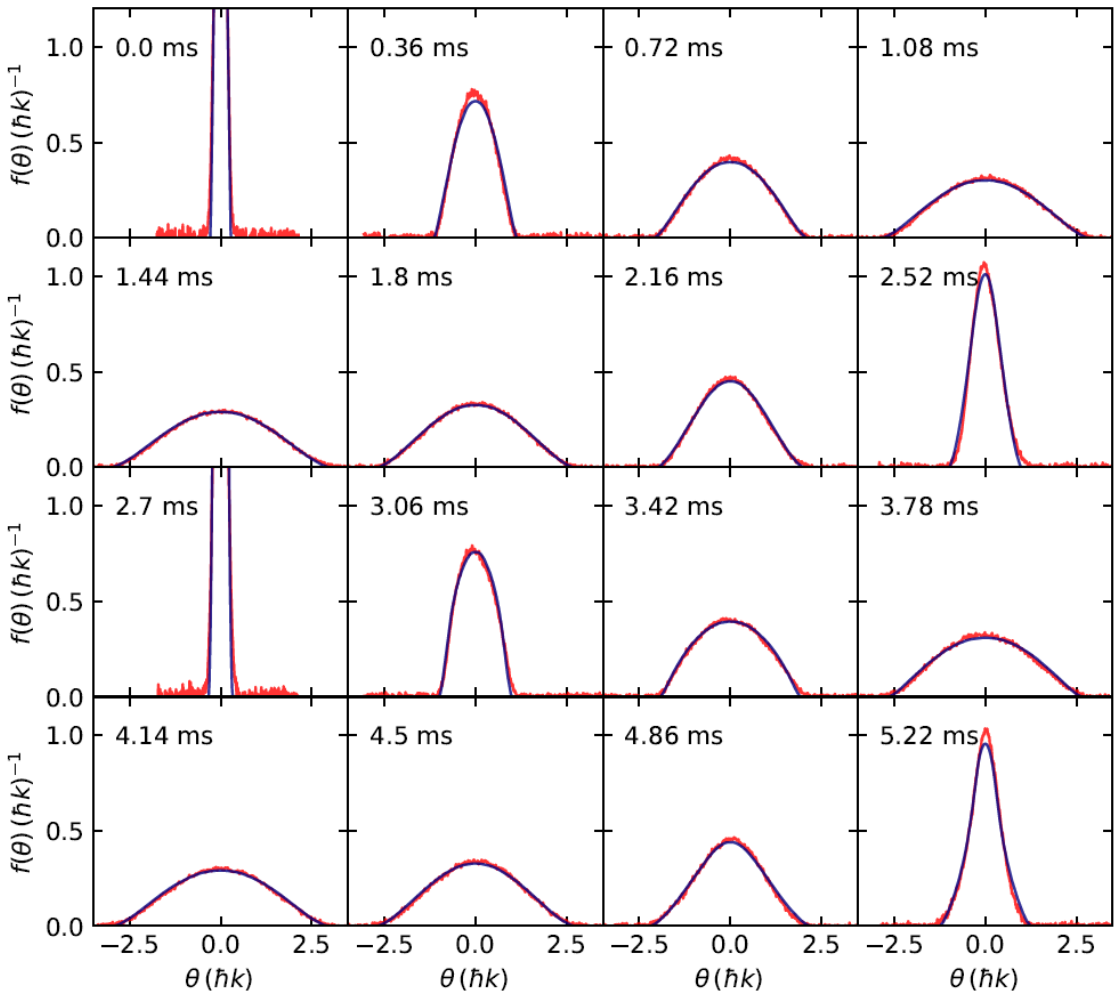

Figure 5.4. Rapidity distributions for the first two cycles after a 100x quench, starting in the strongly interacting regime.The time label is shown on the top left of each panel. Red and blue curves represent experiment and GHD theory respectively, accounting for a 1% day-to-day fluctuation in trap depth between the two cycles. Every theory curve uses the measured atom number at that point.

rapidity energies shown in the top panel are in very good agreement. The insets show the rescaled rapidity distributions for each cycle; interestingly, unlike for the 10x quench, time evolution here is such that rapidity profiles are no longer self-similar past the first cycle. Perhaps a clearer way to see the breakdown of self-similarity is by examining the Fermi occupation ratio $n(\theta, z)$ discussed in Chapter 4, with an example displayed in

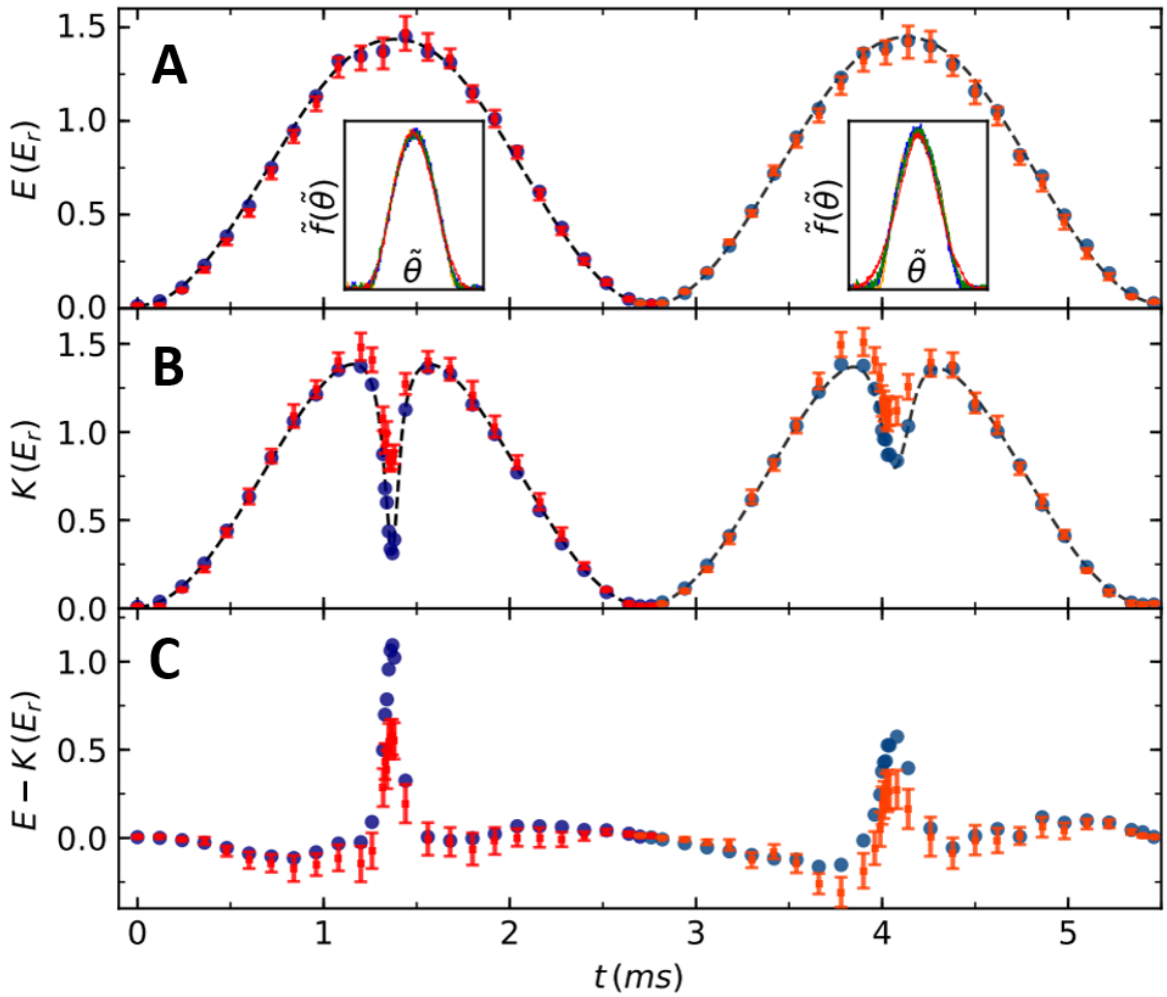

Figure 5.5. Rapidity, kinetic and interaction energy evolution after the 100x quench. Red and orange (dark and light) points represent experimental (theoretical) energies, with the color change associated with a drift in trap depth. Dashed lines are energies where the average atom number during that cycle is used. Panels A and B show rapidity and kinetic energies respectively. Insets in panel A display rescaled rapidity profiles across the first two cycles, and show that the shapes cease to be self-similar by the second cycle. Panel C contains the interaction energy evolution, where the points are obtained by subtracting the kinetic energy from the rapidity energy values.

Figure 5.6 in the next subsection. Rapidity distributions are theoretically obtained by integrating $n(\theta, z)$ over the spatial variable. As the gas evolves after the quench, $n(\theta, z)$ rotates counterclockwise about the origin in phase space. If the rapidity distributions were self-similar in shape, the Fermi occupation ratio would retain its elliptical shape as

it rotated and would be identical in shape after it returned to its initial orientation after a full cycle. What we see here is that even for a single tube evolving, the rate of rotation is not constant for all points; those closer to the origin rotate slower than those further out, leading to twisting of the occupation region and breaking of the self-similarity. Of course, when the average over tubes is taken, the shape is not self-similar either. Another way to visualize this effect is from the spatial distribution (see Figure F.2 in Appendix F). There the atom density for a single tube also does not preserve its shape throughout the cycle, and the differences are reflected in the shape of the rapidity distributions. Even though the shapes vary dramatically in shape for individual tube calculations (see Figure 5.10), changes in the ensemble average are quite modest. We are able to see deviation from self-similarity in our measurements over short times in the face of tube averaging performed by the imaging scheme.

The middle panel shows kinetic energy comparisons (see the discussion of the GHD calculation of energies in Chapter 4). Here, the dip at half-cycle is associated with kinetic energy being converted to interaction energy at points near peak compression. The dramatic increase in density during that time leads to a large interaction energy that somewhat compromises the momentum measurement, as evident in the discrepancy in those points. This is due to the 1D gas evolving while the 2D lattice is being turned off for the momentum measurement. Finally, in the bottom panel, the interaction energy is the difference between the rapidity and kinetic energies.

It should be mentioned that in the short time (0.2 ms) between the kinetic energy maximum and the maximum compression point, the ratio of interaction to kinetic energy

increases from 0.076 to 4.2. The fact that GHD is able to replicate experimental rapidity results when the nature of the quasiparticles is changing rapidly and dramatically suggests that GHD fluid cells being locally equilibrated to a GGE is a valid assumption.

5.2.1 Emergence of additional Fermi seas

All theoretical spatial and rapidity profiles are obtained by solving Equation 4.4 for the parametric curve for each 1D gas, taking a weighted average over tubes and integrating the Fermi occupation ratio for the contained region. After the quench, it is instructive to study the phase space evolution of these curves with GHD. As mentioned in Chapter 4, conventional hydrodynamics can yield the same qualitative results if an appropriate set of ad hoc parameters is chosen. For a tube containing $N = 24$ particles, evolution of the Fermi occupation ratio, $n(\theta, z)$, in phase space is shown in Figure 5.6.

As mentioned earlier, as the gas evolves, the curve defining $n(\theta, z)$ rotates in phase space. One of the striking features of GHD is the presence of multiple Fermi seas, as mentioned in Chapter 4. For evolution before about the first half-cycle, any cut along the rapidity axis only passes through one continuous section where occupation is unity. At around $t_{ev} = 1.38$ ms however, a second Fermi sea emerges, as seen by the vertical dashed line that passes through the shaded region more than once. This point marks the time past which conventional hydrodynamics predicts an unphysical shockwave and the full GHD treatment is required to perform accurate calculations [52]. The appearance of a third Fermi sea occurs sometime near $t_{ev} = 4.2$ ms, but is not clearly visible till the third cycle in the $t_{ev} = 6.9$ ms panel.

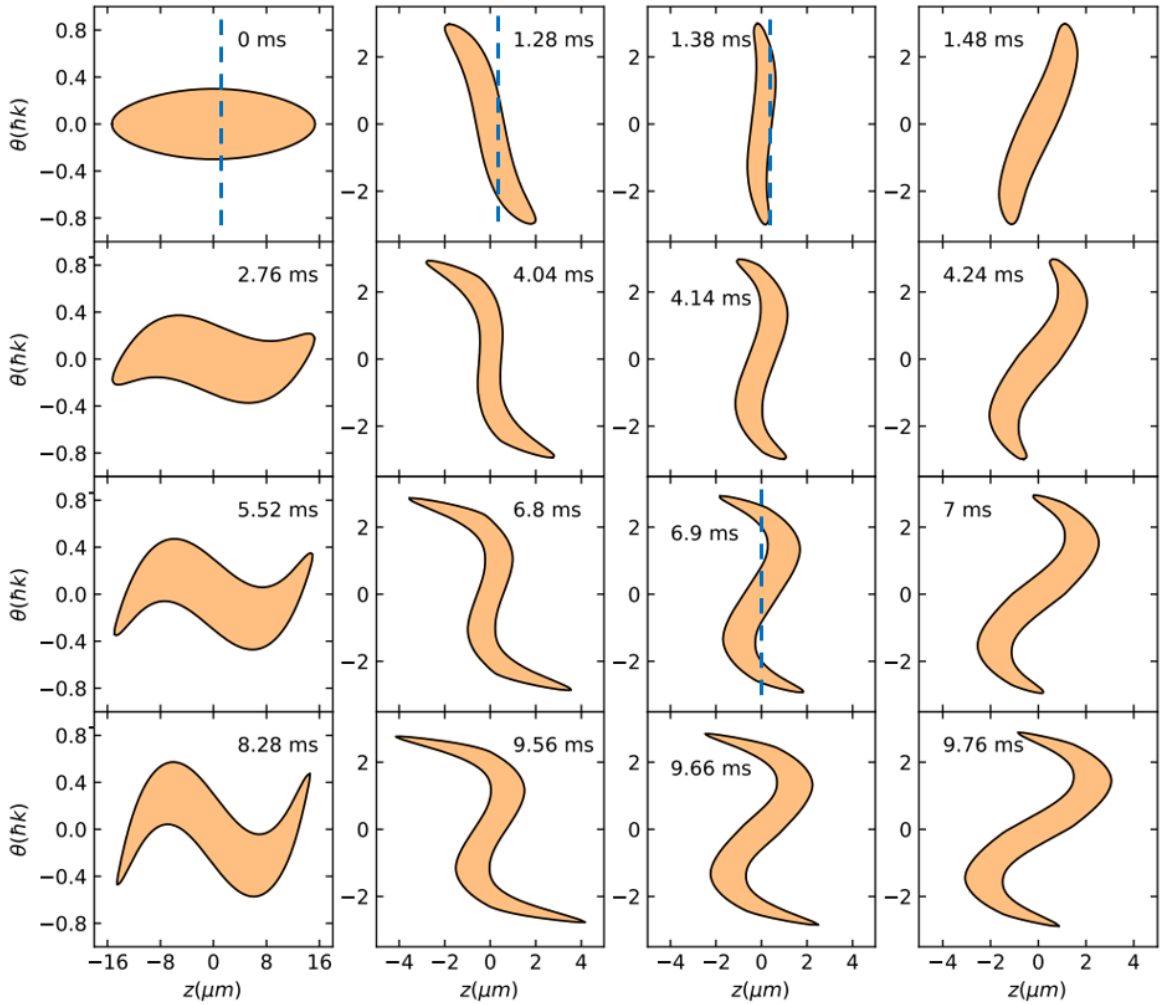

Figure 5.6. Evolution of the Fermi occupation ratio $n(\theta, z)$ for a 1D gas with $N = 24$ particles. Phase space plots are displayed with the spatial coordinate z on the horizontal axis and rapidity θ on the vertical axis, with time labels near the top of each panel. Occupation ratios for the first four oscillation cycles are shown at the beginning of each cycle (left column of panels) and near the peak compression times (the other three columns of panels). The shaded and white areas represent the regions where $n(\theta, z) = 1$ and $n(\theta, z) = 0$ respectively. Sometime near the midpoint of the first cycle, a second Fermi sea arises, as shown by the dashed blue line in the $t_{ev} = 1.38$ ms panel passing through two discontinuous portions of the shaded region. Before this point, a line along the rapidity axis can only cut through one section of the occupation ratio (shown in the $t_{ev} = 0$ and $t_{ev} = 1.28$ ms panels). Later, a third sea emerges at around $t_{ev} = 4.2$ ms, but is not easily visible till the third cycle (see $t_{ev} = 6.9$ ms panel).

5.2.2 Evolution after many cycles

We also test GHD for longer times at later cycles. The panels in Figure 5.7 show rapidity evolution during the sixth cycle. Here, a lot of the features in the experimental profiles

qualitatively match GHD predictions, although the experimental curves are not entirely symmetric. The most dominant cause of this imperfection is likely drifts in the axial levitation of the 17 μm atomic cloud that slightly displaces it (by less than 100 nm) relative to the center of the trap (see Appendix C for a discussion about the centering of the atoms on the trap). This gives atoms on opposite sides of the distribution an uneven kick, and while the effect is not immediately apparent, it compounds over many cycles and shows up in the measurements at later times.

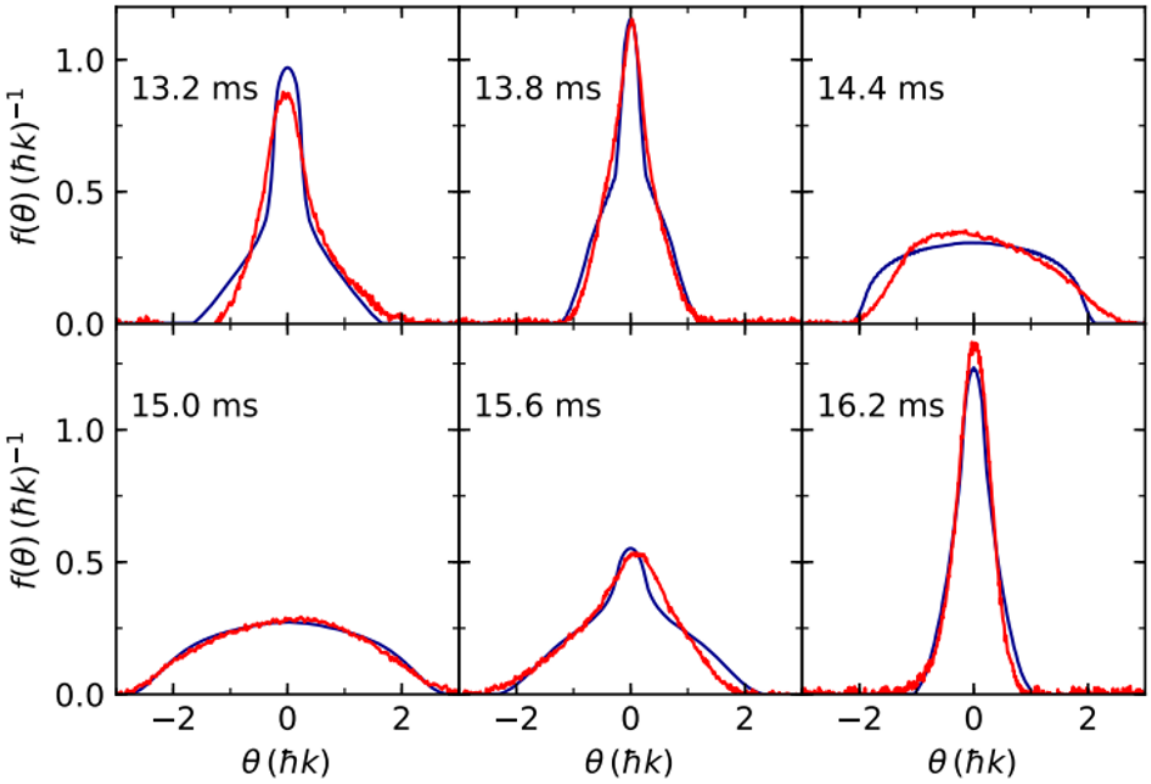

Figure 5.7. Rapidity distributions in the sixth cycle after the 100x quench. Experimental curves (red) and GHD theory curves (blue) are shown at select times throughout the cycle. Average atom numbers are used for all curves. While qualitatively the shapes are consistent with each other, there are asymmetries in the experimental results that are most likely due to trap and quench imperfections.

At even later times in cycles 11 and 21 shown in Figure 5.8, we see that the theory

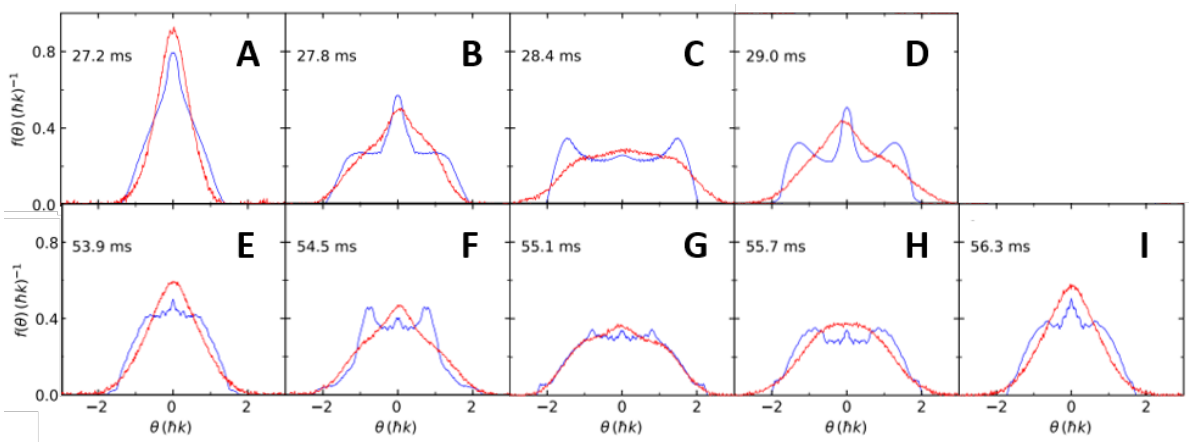

Figure 5.8. Rapidity evolution at even longer times after the 100x quench. Panels A-D show experimental measurements (red) alongside theoretical distributions (blue) for the 11^{th} cycle, while panels E-I show those for the 21^{st} cycle. Average atom numbers are used in GHD calculations and the trap depth is adjusted to match the phase of the oscillation of the rapidity energy evolution (see Figure 5.9). At these long times, experimental imperfections play a role in smoothing out the distributions, obscuring sharper features.

distributions contain sections with large curvature that are not present in the experiment. The same experimental imperfections that give rise to asymmetric profiles can also blur out sharp features over time. It is also important to point out that GHD, a hydrodynamic approach to dynamical calculations, is not an exact theory. It only provides an approximation to predictions of a full quantum simulation of the Lieb-Liniger model. Hence, any deviations from the exact prediction will accumulate and add to the overall discrepancy over time. Unfortunately, at the time this work was done it was not possible to quantify the extent to which either of these errors contribute to the disagreement.

Energy evolution for cycles 6, 11 and 21 is shown in Figure 5.9. Being an extensive quantity, the rapidity energy contains some information about the evolution but doesn't provide the full picture of the complicated many-body dynamics in the same way as the

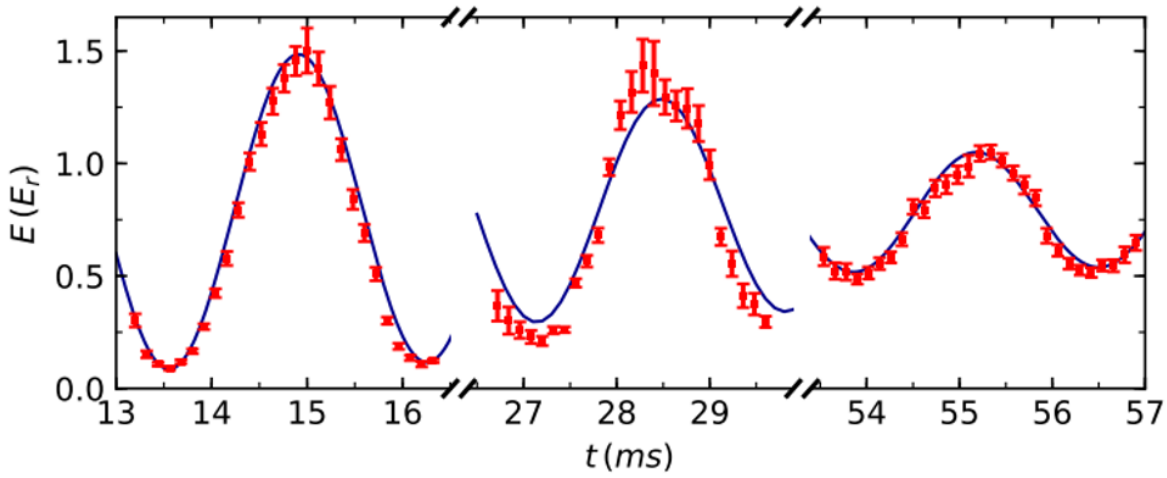

Figure 5.9. Rapidity energy evolution at longer times. Experimental (theoretical) energies are shown in red (blue) for the 6^{th}, 11^{th} and 21^{st} cycles after the quench. Average atom numbers during those cycles are used in GHD calculations, and the trap depth is chosen such that the phase of the theory oscillations matches the experiment. Evolution of the individual 1D gases accounts for 20% of amplitude reduction, while the rest is due to tube averaging.

actual distributions. At long times there is a reduction in the amplitude of the energy oscillation; theory shows that there is about 20% reduction due to the inherent evolution in individual 1D Bose gases. The rest of the large amplitude reduction seen in the figure is from the mundane effect of inhomogeneity in the axial trapping (about 28% variation in the trap depth across tubes). Tubes therefore evolve with slightly different oscillation frequencies and after dozens of cycles these oscillations dephase, leading to a smaller amplitude oscillation when tube averaging is performed. The blue theory curves include both these effects. Even though the profiles in Figure 5.8 are qualitatively different between theory and experiment, the energies are well-predicted by GHD.

In the future, one improvement could perform experiments with a configuration that provides more uniform trapping. We plan on upgrading our system to do just that (see more of this discussion in Chapter 6). Being able to see sharper features in the

distributions could help put stronger constraints on the validity of GHD.

5.3 Comparison of GHD results to calculations in the Tonks-Girardeau limit

To see if GHD provides an accurate description of non-equilibrium dynamics, one can compare its predictions of system behavior in a limit in which other theoretical approaches can be used. We validate GHD by calculating evolution at low particle numbers after our 100x trap quench. By setting the contact interaction strength g_{1D} used for GHD far into the Tonks-Girardeau regime, we are able to directly compare to exact Tonks-Girardeau theory. These exact numerical simulations are done on a finely-spaced 1D lattice with a low filling fraction, with the constraint that any given site can only be occupied by at most one boson. Effectively creating a mapping of bosons to non-interacting spinless fermions, this approach has been used in simulations of dynamical fermionization [5].

Here, we simulate quench dynamics for tubes containing 5, 10, and 20 atoms. Figure 5.10 shows the comparison of GHD and exact rapidity distributions for several evolution times, along with the ensemble average. The exact theory has finite particle number effects called Friedel oscillations that overlay onto the overall shape, but when averaged over the ripples, the curves are identical to GHD results. Black curves represent average over tubes, and the GHD and exact theory distribution are indistinguishable. In the experimental distributions, the measurement inherently includes an average over tubes with many different atom numbers and does not exhibit any oscillations.

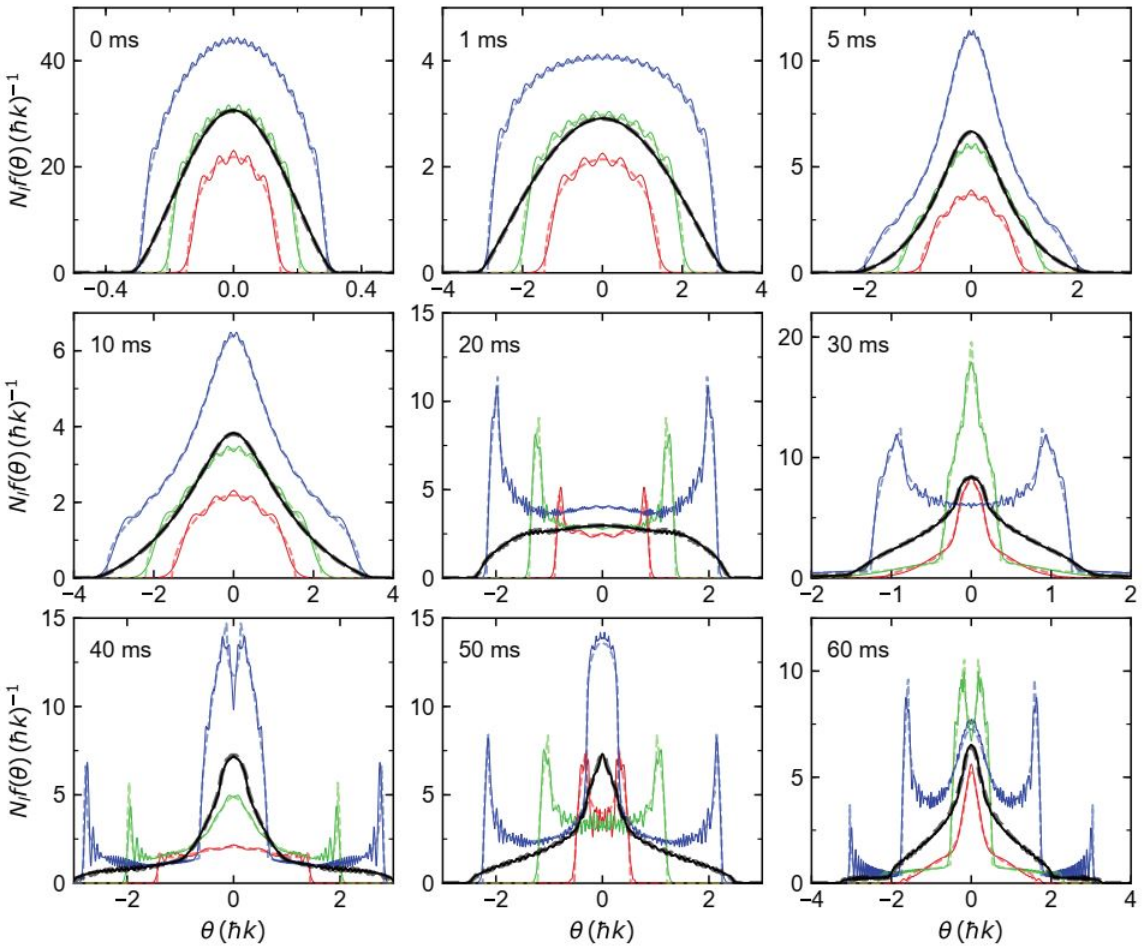

Figure 5.10. Comparison of GHD to exact Tonks-Girardeau theory for low particle numbers. Simulations of the 100x quench for the same experimental parameters are done using both approaches, with solid (dashed) lines denoting exact (GHD) theory. Rapidity distributions for tubes containing 5, 10, and 20 particles are shown in red, green, and blue respectively. Exact theory curves contain oscillatory features emerging from finite number effects, but the shape is the same as for GHD. The average over all tubes is shown in black, and is essentially identical for the two approaches.

Chapter 6

Ongoing and near-future endeavors

6.1 Relaxation after a wavefunction quench

Besides trap quenches, we can perform another type of quench: a wavefunction quench. Instead of suddenly changing the atoms' confining potential, we put them in an out-of-equilibrium state that is a superposition of non-zero momentum states. This is very similar to what was done in the original quantum Newton's cradle experiment, but there the focus was on evolution after the initial dephasing of the atomic cloud [30]. In this ongoing project we attempt to observe the dynamics as the system undergoes immediate relaxation to the local GGE after the quench [54, 55].

6.1.1 Producing an optical Bragg pulse

To quench the wavefunction, we suddenly pulse on a standing wave along the axial direction. We turn on the z-lattice beam for 5 μs, creating a 1D lattice potential that acts as a diffraction grating for the atoms. This is analogous to light diffracting from a grating and interfering with itself to form a pattern of intensity maxima and minima on a screen in the far-field. In this matter-wave version, the atoms' wavefunction picks up a phase proportional to the local lattice potential:

$$\psi \longrightarrow \psi e^{i\phi} \tag{6.1}$$

where $\phi \propto cos(kz)$ is proportional to the beam intensity and $k = 2\pi/775\ nm$ is the lattice wavevector. This quench puts the atoms in a superposition of $p = \pm 2n\hbar k$ momentum states, where $n = 0, 1, 2, 3, ...$. Evolution of this highly non-equilibrium state is a great testing ground for the predictive power of GHD.

6.1.2 Momentum evolution after the quench

We start with a 1D Bose gas array containing a total of $N \sim 3 \times 10^5$ atoms in the same initial trap that we use for the 100x trap quench. We then apply the standing wave pulse to quench the wavefunction on a spatial scale that is much smaller than the size of the distribution, so that the gas is no longer in local equilibrium. Immediately after the system has been put out of equilibrium, the momentum distribution is expected to have a central peak surrounded by satellite peaks corresponding to the momentum state

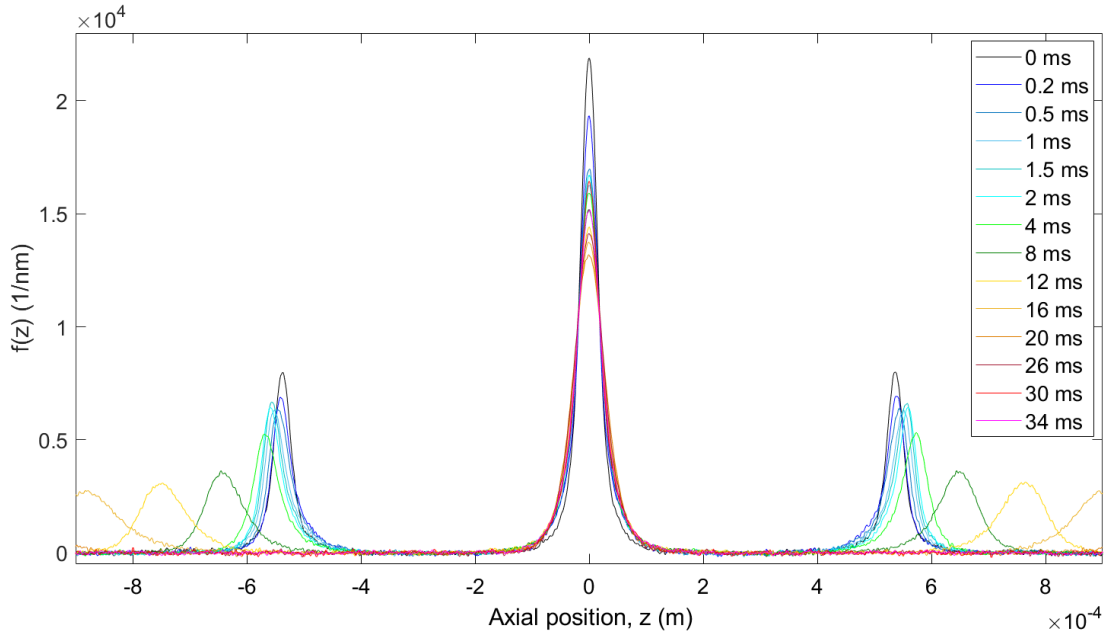

Figure 6.1. Evolution of the time-of-flight momentum distribution after a Bragg pulse quench. All distributions are normalized such that the area under the central peak is unity. Peaks in the initial distribution start to broaden rapidly as the gas locally equilibrates to a GGE. This is followed by the start of the familiar breathing oscillation as the gas responds to a depletion of atoms in the center. Satellite momentum peaks leave the field-of-view with time, as their kinetic energies are too large to be confined by the axial trap.

superposition. We measure these time-of-flight distributions after a variable evolution time in the initial axial trap. Our aim is to study the central peak.

The preliminary data for momentum evolution at various times after the wavefunction quench is shown in Figure 6.1. The first thing to note is that the satellite peaks start to escape the field-of-view after a couple of milliseconds; we choose a shallow 1.2 E_r trap so they are able to escape, rather than returning to collide with the central peak. Hence, we focus on the portion of the momentum distribution still accessible. The initially sharply peaked central peak starts to broaden quickly over the first millisecond or so and then slows down as the system finishes locally relaxing. A better way to see this is by following the full width at half maximum (FWHM) of the central cloud as a function of time, as

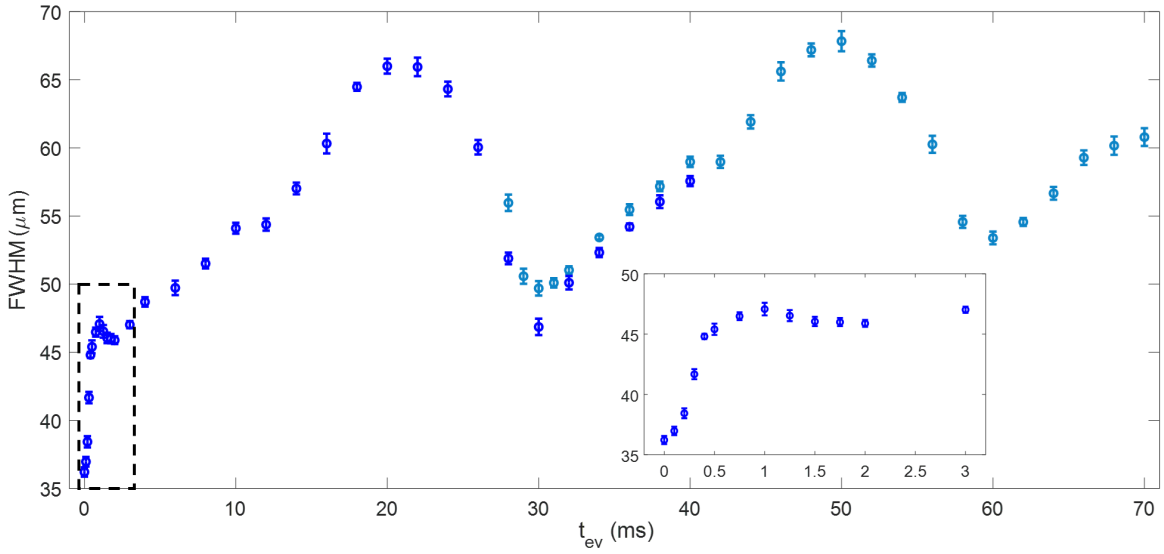

Figure 6.2. Evolution of the full width at half maximum (FWHM) of the central peak of the momentum distributions. Change in color denotes measurements taken at a later date, when the gas' initial temperature was higher (the qualitative behavior is the same). A blown-up view of the rapid initial rise (outlined by the dashed black line) is shown in the inset. The immediate sharp rise in the FWHM is followed by an asymmetric breathing oscillation. However, the system does not return to its initial state it instead repeats its asymmetric breathing behavior while slowly losing contrast.

shown in Figure 6.2.

Here, we can see the approach to local equilibration; the rapid initial broadening occurs as the gas relaxes to the local GGE. Since information about the quenched non-equilibrium state has to travel through the gas, the natural timescale for equilibration can be estimated by the time it takes for sound to propagate across the atomic cloud [54]:

$$t_{eq} \sim (q v_s)^{-1} \tag{6.2}$$

The above expression is for particles in a ring geometry (instead of an inhomogeneous system with a confining trap). Hence, $q = \frac{2\pi}{L}$ is the lowest order of the quantized Bragg momentum associated with periodic boundary conditions, L is the size of the gas, and v_s

is the speed of sound through the gas. For a Lieb-Liniger gas the speed of sound can be calculated using thermodynamic relations [56]:

$$v_s(\gamma) = \frac{\hbar}{m|a_{1D}|}\left[2\frac{d^2e(\gamma)}{d\gamma^2} - \frac{8}{\gamma}\frac{de(\gamma)}{d\gamma} + \frac{12}{\gamma^2}e(\gamma)\right]^{1/2} \tag{6.3}$$

where $e(\gamma)$ is a solution to the Lieb-Liniger system of equations (See Appendix D for some more information). In the low γ limit, the expression can be reduced to [56, 57]:

$$v_s = \frac{\hbar n_{1D}}{m}\left(\gamma - \frac{1}{2\pi}\gamma^{3/2}\right)^{1/2} \tag{6.4}$$

Equation 6.4 is accurate for $\gamma \leq 10$ and therefore applicable to our system. For our experimental parameters the speed of sound is

$$v_s \approx 3\frac{mm}{s} \tag{6.5}$$

With the distance from the center to the edge of the gas about 10 μm, the time taken for information to travel across the gas is about 0.5 ms, which is comparable to the observed equilibration time.

Past equilibration, the FWHM behavior shows evidence of breathing, as the cloud collapses after the quench depletes a significant fraction of atoms into higher momentum states which then escape. It remains to be seen why the shape of the breathing oscillations is asymmetric, but it is reproducible and repeats over the first couple of cycles. We plan on doing a simulation of dynamics using GHD for this quench so it can shed some light on the matter. We will also study the relaxation to local GGE at different densities to

explore its behavior at different initial conditions.

6.2 Upgrades to the experimental apparatus

As mentioned in Chapter 2, we recently obtained a new 50 W 1064 nm laser to replace the old 10 W laser that had an electronic malfunction. With the additional power, we were able to put more than twice the previous power into the crossed dipole trap beams used to create the BEC. We plan to use the remaining ∼20 W to form additional beams for a more uniform trapping configuration.

6.2.1 Dipole trap beam shape improvement

The intensity modulation setup for the dipole trap beams used for the work in this dissertation has been described in Joshua Wilson's thesis [25]. We use a scheme that consists of vertically polarized light incident on an electro-optic modulator (EOM) followed by a Glan-laser prism. When a control voltage is applied to the EOM, it smoothly rotates the polarization of the incoming light and the prism dumps the light which has a horizontal polarization component. The actual setup uses two pairs of EOMs and waveplates, each followed by a Glan-laser prism, to get a light intensity at the end that is a smooth function of the EOM control voltage. We had set up the configuration such that we get as much of the incoming 10 W of light as possible when each EOM is performing a full $\lambda/4$ rotation of the polarization, but also so that we are able to achieve as little leakage as possible when the EOMs are fully off. We also drove the two EOM

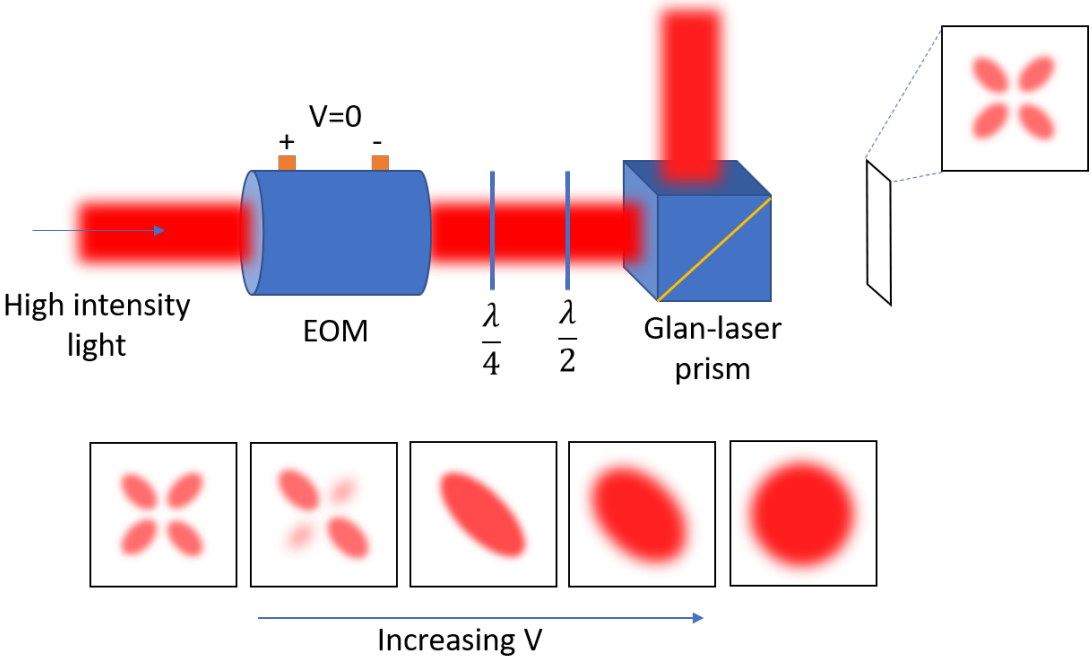

Figure 6.3. Emergence of a clover-leaf pattern due to a thermal depolarization effect in the EOM crystal. Top: The pattern is present at zero EOM control voltage when there is a high intensity beam incident on the crystal. Bottom: As control voltage is increased, the beam shape becomes more circular as more of the light with the correct polarization is transmitted. At full transmission the beam shape is identical to that of the incoming beam.

pairs with two different high-voltage supplies, each with a slew rate of 35 V/μs. For the experiments discussed in this thesis involving large sudden quenches, we drove all 4 EOMs with another single more powerful supply with a much higher slew rate 750 V/μs so we could make faster changes in the intensity.

When high light intensities (more than a couple of Watts) are incident on our EOMs, there is a thermal depolarization effect that slightly perturbs the polarization of the light making it through the crystal. Even with zero control voltage applied to the EOMs, there is a non-negligible amount of light that gets past the Glan-laser prism and which has a clover-leaf shape relative to the polarization axes of the EOM crystal.

As seen in Figure 6.3, the shape of the clover pattern changes with control voltage in

a way that makes one of diagonals more intense and other less intense for small voltages. As the voltage increases, the beam becomes rounder in shape; near full polarization rotation, the beam returns to its Gaussian shape as all the light is transmitted. This effect was present in the setup with the 10 W laser, but the second set of EOMs and prism was able to give a fairly round beam throughout the whole range of intensities. Now with more than 20 W incident on the EOMs, the effect is much more pronounced and the beam shape is highly elliptical if the same configuration is used.

While setting up and aligning the new beam, we discovered a property of the thermal depolarization effect that we were able to exploit to our advantage. We noticed that reversing the polarity of the EOM control voltage has the effect of making the beam more intense along the opposite diagonal.

So, if the first pair of EOMs were set up to rotate the polarization in one direction, the second pair could be set up with the opposite polarity and therefore the two sets would elongate the beams along opposite directions (see Figure 6.4). This made the beam much rounder for our range of control voltages.

Another adjustment we made was letting a small fraction of light ($\sim$1.5 W) past the first Glan-laser prism by intentionally misaligning one of the first EOMs. With the higher transmitted intensity after the first Glan-laser prism, the Gaussian shaped dominates the clover pattern when incident on the second set of EOMS, so when they are turned on at low voltages the final beam at the end is rounder in shape.

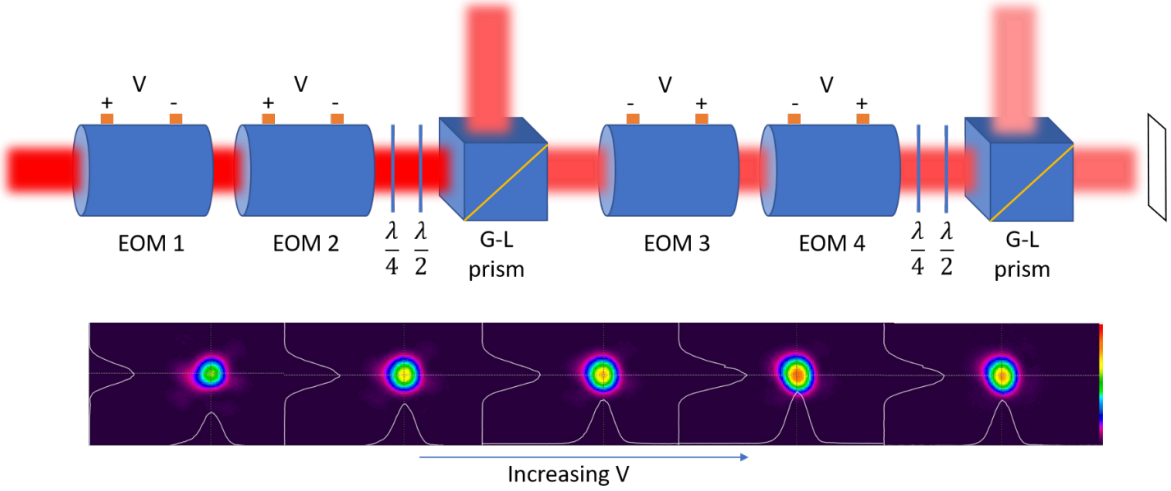

Figure 6.4. The intensity control setup with the upgraded 1064 nm laser. Top: The second pair of EOMs is driven by high voltage with the opposite polarity of the first pair so the beam shape preserves more of its roundness as the voltage is increased. Pictures on the bottom show actual beam shape measurements after the final Glan-laser prism, for control voltages ranging from 0.05 V to 0.5 V.

6.2.2 Beam for a flat potential

The lattice anti-trap has so far been compensated for by leaving on a shallow dipole trap that keeps the potential flat over ∼30 μm and limits our 1D flat potential to a small range. A larger flat region would grant us access to much longer 1D expansion times, making rapidity measurements more reliable at the tails, and also give us the ability to perform the entire TOF in 1D in experiments with an axial lattice. We plan to achieve a large flat region by using a fraction of the available 1064 nm power to directly correct for the anti-trapping potential (which has a negative curvature) with a positive curvature trap with the same size, creating a flat potential over hundreds of μm.

This beam will require about 6 W of power to produce the necessary trap. Intensity control will be achieved with an AOM. The beam will travel across the optical table

through free space and into the chamber along the same path as the y-molasses beam, with the help of a dichroic mirror.

6.2.3 Beams for more uniform trapping

As we saw in the GHD treatment, all calculations in the theory must involve averaging over all the 1D tubes. Experimentally, the 'averaging' is built into the image acquisition process and it can often smear out interesting features in the distributions. One way to be more sensitive to these is to have more uniform trapping across the tubes so that trivial effects such as dephasing between tubes during evolution are not as big a contribution.

To achieve more uniform trapping, we plan on creating two beams: one with a relatively high ellipticity coming in along the x-direction and one with a top-hat shape coming in along the z-direction. The resulting trap will not have as large a variation in axial trap depths as we do currently over the region that tubes are occupied. We plan to create the BEC in the compressible crossed dipole trap and then turn on the 2D optical lattice along with these new trapping beams. The high ellipticity trapping beam will enter the chamber from the x-direction along the same path as the x-molasses beam, again with the help of a dichroic mirror.

6.3 Future experiments

Along with the ongoing evolution after Bragg diffraction experiment, we plan on performing other experiments to test GHD and to study systems away from integrability.

We are already working on getting a better understanding of thermalization due to diffractive 3-body collisions present in our system. Going further, we can induce stronger integrability breaking and observe the effects on thermalization rate. Two proposed methods of achieving this are adding a weak lattice in the axial direction, and increasing the tunneling rate between tubes so as to push the system away from quasi-1D. We will aim to measure both momentum and rapidity evolution in these experiments to obtain a handle on quantum many-body dynamics under non-integrable conditions. We also hope to push the limits of GHD and see when its predictive power breaks down.

6.4 Conclusion

In this dissertation I have described several recently conducted experiments with 1D Bose gases under various starting conditions and following strong quenches. These had the primary purpose of testing a newly-developed theoretical model called Generalized Hydrodynamics (GHD) in conditions that have not been previously explored. In this chapter I outlined further efforts in understanding more exotic systems using our apparatus. Since quantum many-body behavior is difficult to calculate even with state-of-the-art computations, we hope these works will inspire future studies into better understanding dynamics in regimes where theoretical tools are not as well-developed.

Appendix A

Principal component analysis background subtraction

As briefly mentioned in Chapter 2, when we take data in the form of absorption images, we use a combination of three different image measurements: one with no atoms or probe light (Z), one with both probe light and atoms (S), and one with probe light but no atoms (P). The operation $\frac{(P-Z)}{(S-Z)}$ on the pixel values of these three shots gives an image of the atomic density. Due to the complicated nature of the absorption probe beam path to the CCD, the probe background image usually has imperfections from interference effects and intensity fluctuations (see Figure A.1). Ideally, if nothing changes between the probe beam background (P-Z) and atom signal (S-Z) shots, the latter would have identical imperfections that would be removed when the ratio is taken to extract the atom density.

Unfortunately, slight changes in intensity, vibrations and other instabilities in the beam create a residual interference pattern when the atom density is obtained (see panel

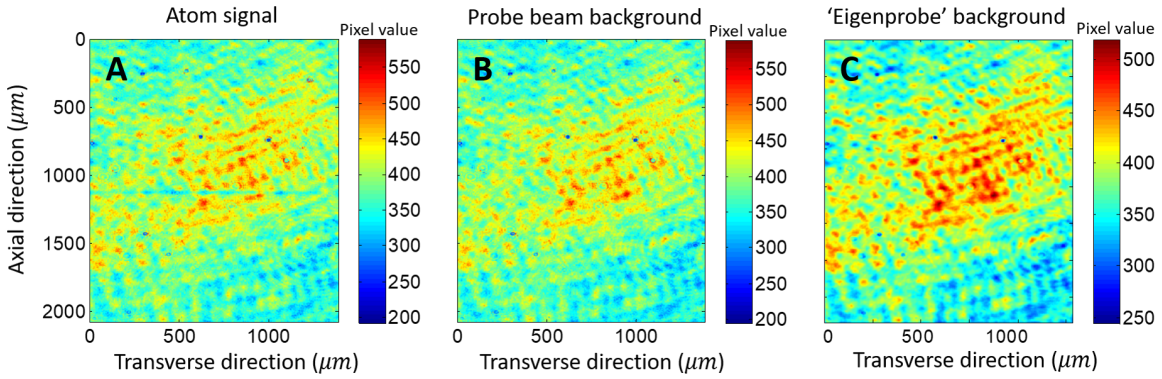

Figure A.1. Examples of images acquired during our absorption imaging scheme. The atom signal image (panel A) is a picture taken with the probe beam casting a shadow on the atomic cloud, but after subtracting an image with only the ambient light. We also need to take an image with only the probe light (after subtracting an ambient light), which is shown in panel B. The ratio of these two gives an unprocessed image that plots the atom density. As part of the principal component analysis technique, the algorithm generates 'eigenprobe' backgrounds (panel C) that are then combined to subtract off any residual high-spatial-frequency fringes in the atom density image background.

A in Figure A.2). The pattern is usually a high-spatial-frequency signal on top of the atom density, which is independent of the time between the probe background and atom signal shots and whose phase varies randomly from shot to shot. Ideally we would like to have a flat background signal without any features because integrating images is how we get the rapidity and momentum distributions and their respective energies. Any high-frequency features would affect said distributions, so we attempt to eliminate them as much as possible.

We use a principal component analysis (PCA) technique to get around this problem [42]. The algorithm we use takes backgrounds from 25-30 atom density images, but only from the region that does not contain any atom signal. With these backgrounds it creates a set of principal component ('eigenprobe') images that contain a combination of the high-frequency features from the backgrounds, as well as images with their 90°

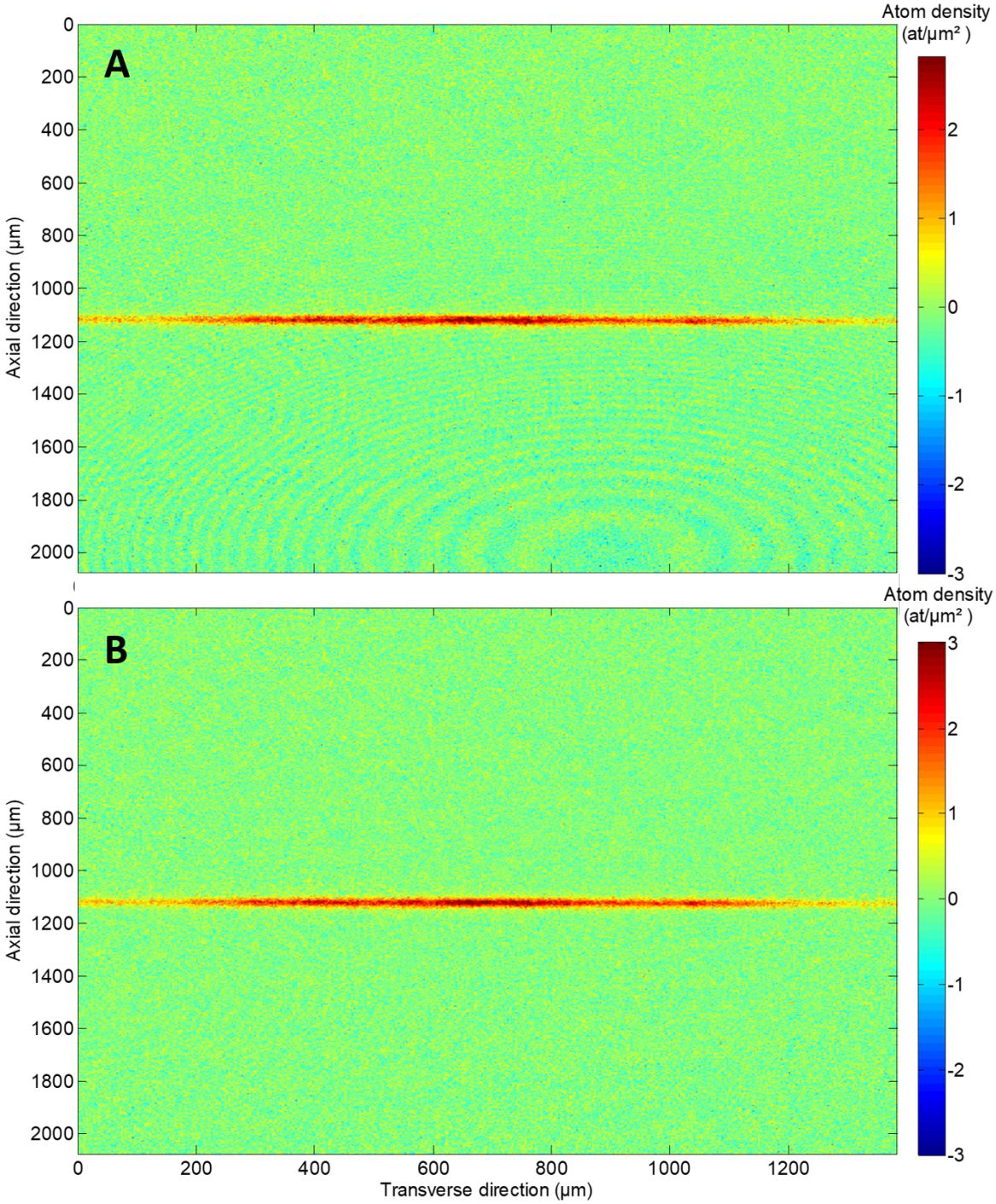

Figure A.2. An example showing our principal component analysis algorithm effectiveness. An unprocessed atom density image (A) is obtained by taking the ratio of atom signal and probe beam background images. Interference effects in the probe beam leave high-frequency features as seen in the regions where the background should nominally be flat. After processing the image using the PCA algorithm, we obtain a 'cleaned' image (B) that greatly reduces the amplitude of the interference fringes.

out-of-phase counterparts. It then fits the background of each atom density image to a linear combination of eigenprobes and the out-of-phase images. When the linear combination is subtracted from the background, it produces a 'cleaned' image with the fringes highly suppressed (shown in panel B in Figure A.2).

The principal component subtraction algorithm is applied to all atom density images to obtain processed images that are then used in the data analysis. While this method works well to remove high-spatial-frequency features, it does not get rid of slowly varying signals overlaying the background. Energy extraction is affected by this residual background, so we perform an additional background correction that is presented in Appendix E.

Appendix B

Centering the atomic cloud on the axial trap

B.1 Alignnment of the axial trap with the lattice anti-trap

An ideal quench requires all the traps to be aligned with each other in order to have symmetric behavior that can be modeled by theory. We begin by aligning the axial trap with the lattice anti-trap. Since two beams combine to make up the axial trap, we align one of them at a time. After creating a BEC, we load the atoms into the 2D optical lattice while keeping both dipole trapping beams on. We then turn off the y beam by ramping down RF power to the AOTF, so that all the trapping is provided by the x beam. We let the atoms relax in this trap and then release them.

As the cloud expands under the influence of the anti-trap, the center of mass drifts in

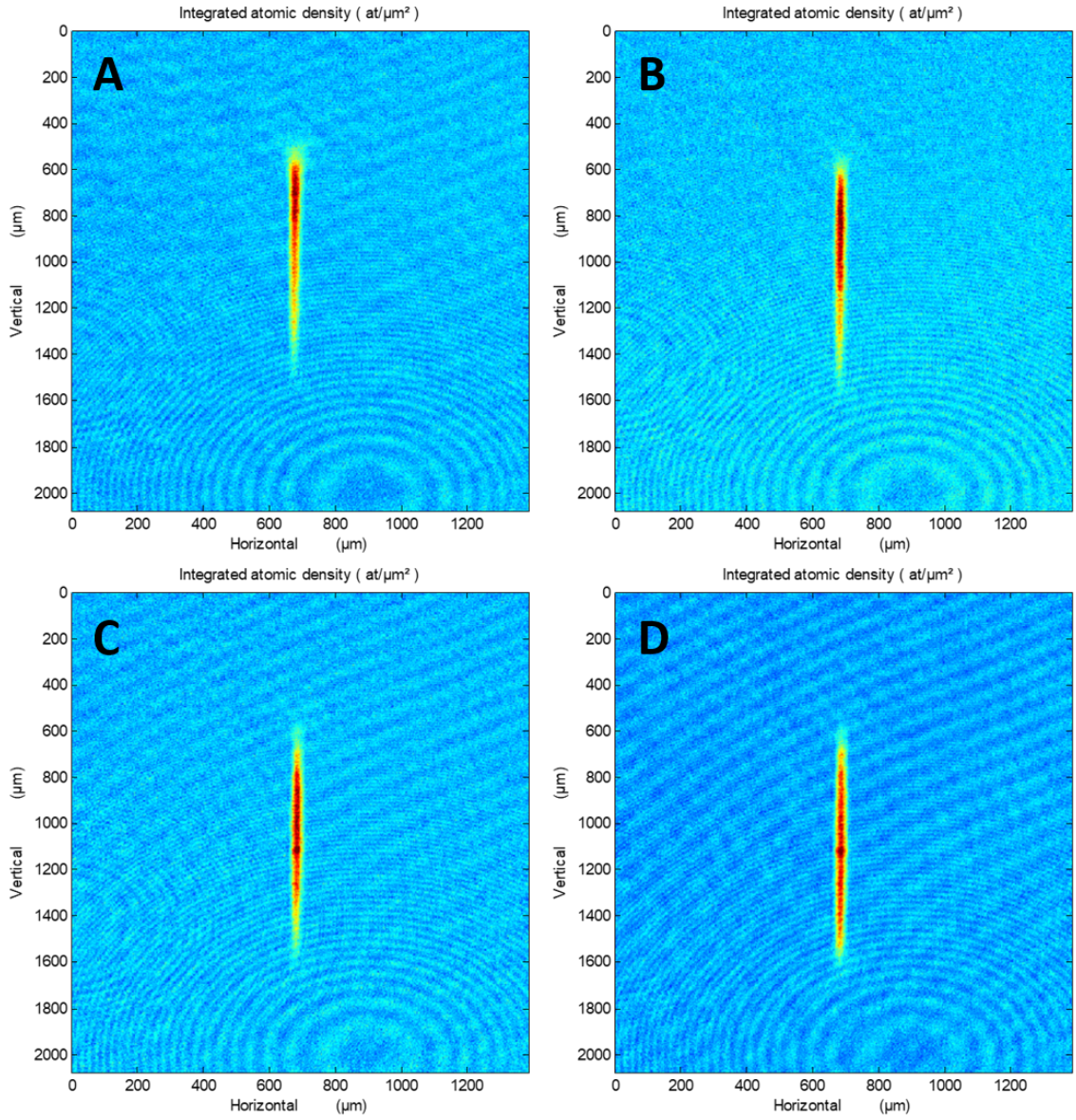

Figure B.1. Absorption images after 40 ms of 1D expansion in the 2D optical lattice following release from the x dipole beam. Starting from the image in panel A, the atoms drift upwards due to the influence of the anti-trap when the axial trap is not aligned with the lattice. As the x dipole trapping beam is moved down, the expansion starts to become more symmetric (panels B→C→D). When the trap is well-aligned with the anti-trap the atom cloud is symmetric after expansion (panel D).

the direction of the axial trap relative to the anti-trap (see panel A in Figure B.1). We take an image after 40 ms of expansion, showing the degree of misalignment between

the two. To correct it, we simply move the x dipole beam in the direction needed for symmetric expansion and take images as needed. When the beam is at the right position, the expansion is symmetric about the center and the x axial trap is considered aligned with the anti-trap (panel D in Figure B.1).

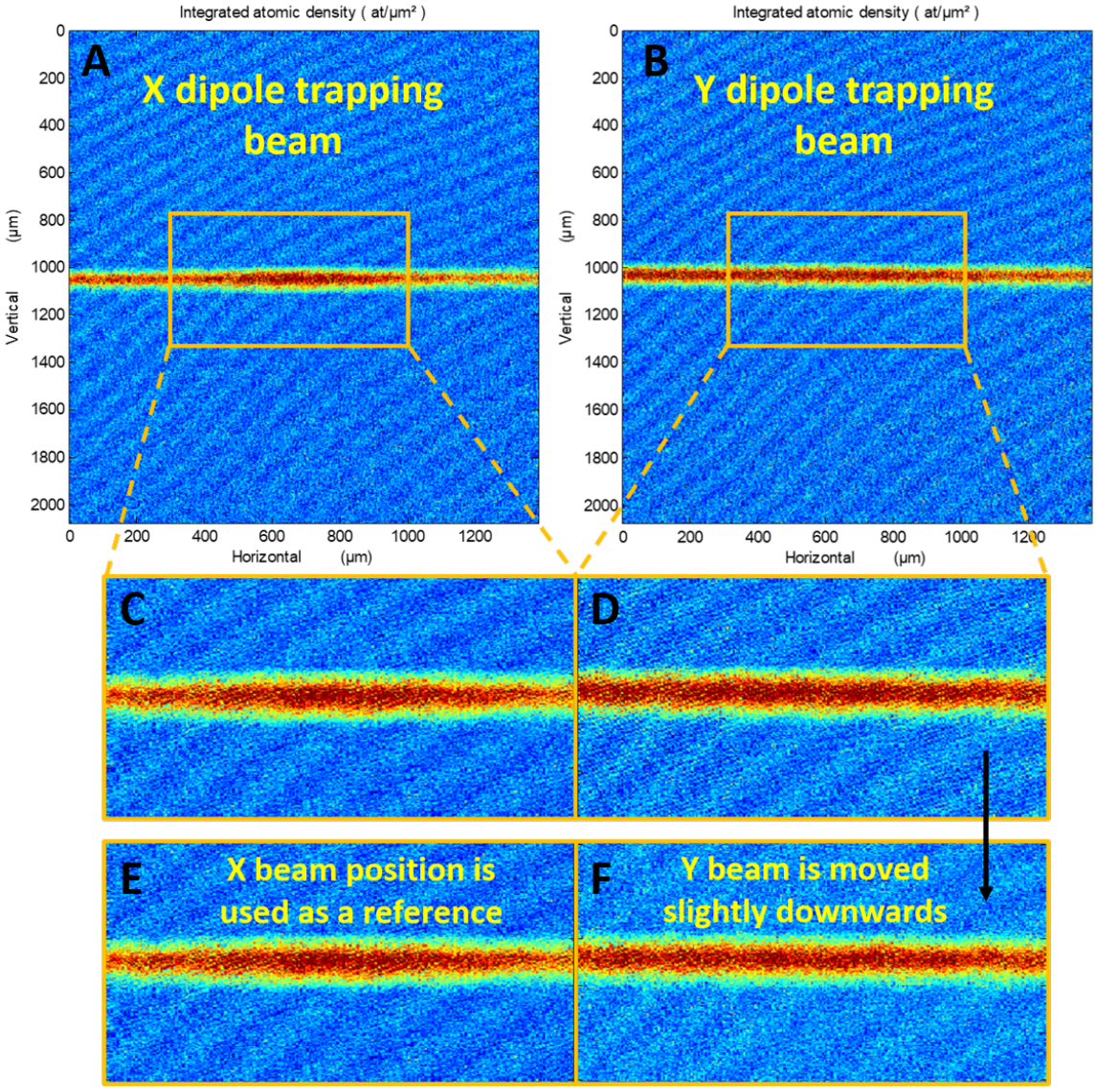

Figure B.2. Images showing alignment of the dipole beams relative to each other. After BEC production, the x(y) beam is turned off and atoms are transferred to a single trapping beam in the y(x) direction. An image is taken after 50 ms of holding time in the trap to get the relative vertical positions of the x beam (left) and y beam (right). A zoomed version is shown near the bottom as a guide. After moving the y beam down, the alignment is improved.

Next we need to align the y dipole beam with the x beam that is already in the right place. We measure the location of the two beams and use the x beam as a reference for alignment of the y beam. To make a measurement of either beam we transfer atoms from the MOT directly into a single trap created from only that beam at full intensity. The atoms spread out along the beam direction and imaging them tells us the location of the trap. As seen in the zoomed in image in Figure B.2, the y dipole beam is initially slightly displaced from the x beam. We repeat the process of moving the y beam in the appropriate direction and imaging until the beams are aligned to within 5 μm (see bottom pair of images in Figure B.2).

B.2 Fine-tuning the magnetic field gradient for balance against gravity

Now that the traps are aligned, we want to levitate the atoms as best as possible to ensure a symmetric trap quench across the atom cloud. Perfect balance is achieved when the sum of all remaining forces - gravity plus magnetic field gradient - is zero. As discussed in Chapter 2, the atoms are levitated by a field gradient after optical pumping to the $F = 1, m_F = 1$ state. The extent to which we can balance the atomic cloud is determined by the sensitivity and stability of the field gradient.

Evaporating further past our normal BEC procedure lets us obtain a cloud containing 2×10^4 atoms in a very shallow 0.05 E_r deep crossed dipole trap. We check the centering by measuring the drift after free 3D expansion from the small BEC (see Figure B.3).

Starting from the small BEC we turn off the trap and the field gradient. Time-of-flight images are taken 20 ms (panels A-D) and 90 ms (panels E-H) after the expansion, and the change in the atoms' axial positions are monitored (any motion during the gradient shutoff is identical in both TOF measurements). As the field gradient is increased the cloud drifts upwards during expansion, and we aim to minimize the size of the drift. With the smallest changes we can make to the current in one of the Helmholtz coils generating the gradient, we are able to achieve a drift as small as $\sim$5 μm between the two TOF measurements for a cloud that is 60 μm in size (see panels B and F). For the axial trap used in the 100 quench, this corresponds to an atom distribution displacement of less than 100 nm from the trap center. For the much deeper trap used in the 10x quench, the displacement is less than 10 nm.

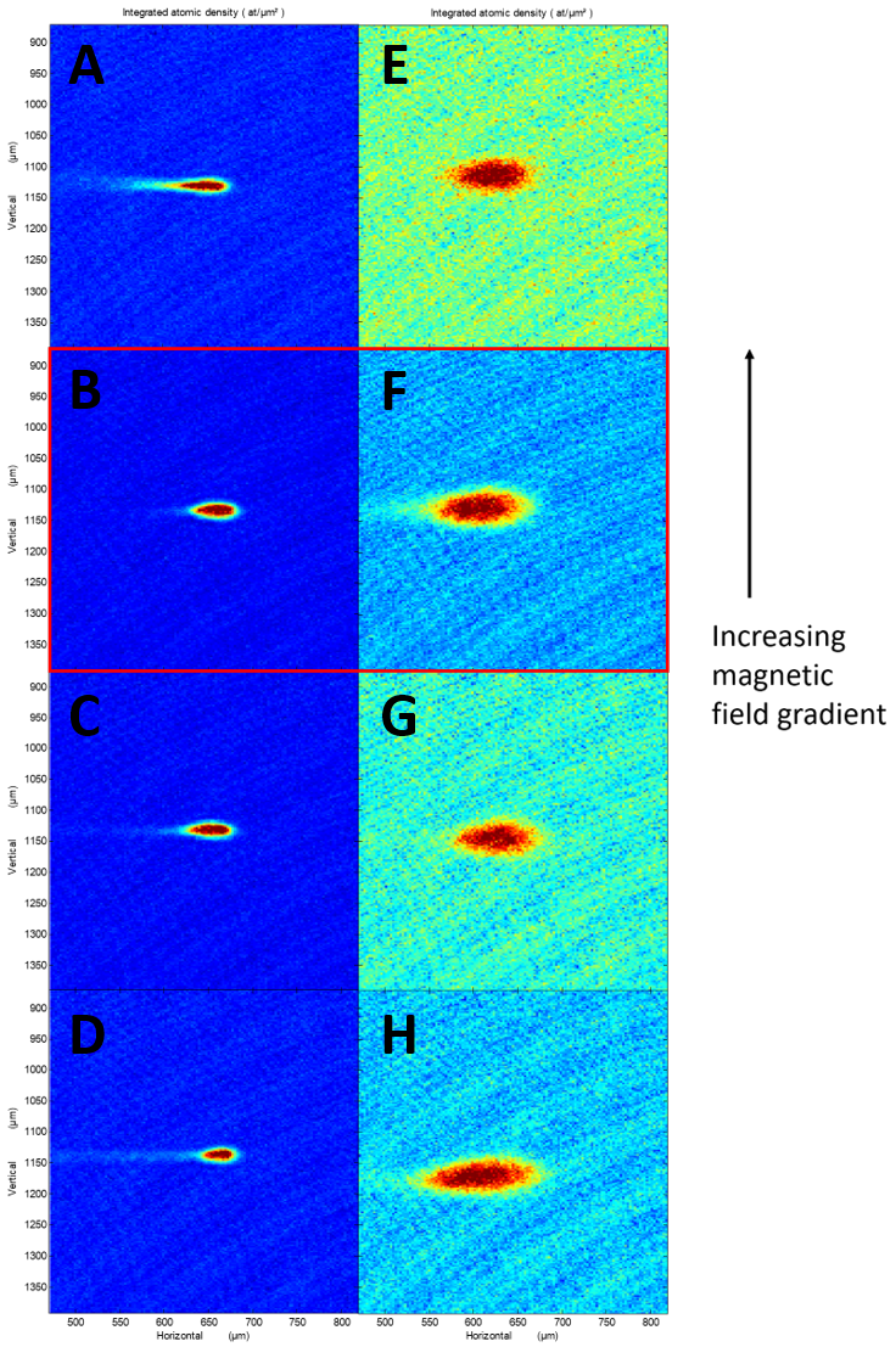

Figure B.3. Time-of-flight measurements of a tiny BEC after 3D expansion, for different magnetic field gradient strengths. Images taken after a 20 ms TOF are shown in the left column while those for 90 ms TOF are shown on the right. As the gradient is increased by controlling the amount of current in one of the Helmholtz coils, the cloud drifts upwards due to the non-zero force. At the best gradient setting (second row of images) the vertical drift is minimized to within 5 μm. The tails to the left of the main clouds are due to forces from residual transverse gradients.

Appendix C

Engineering a dipole trap depth ramp for the quench

When we perform our quenches, we have to make large changes to the axial trap depth, and therefore the intensity of the dipole trap beams, in as short a time as possible. Ideally we would want the quench to look like a rectangular pulse in time with a width equal to the variable evolution time t_{ev}. In practice we must consider experimental limitations in the speed with which we can ramp the intensity. With the intensity modulation setup used in the relevant experiments (described in Chapter 6), a sudden but small rise in the EOM voltage control lets the intensity of the transmitted beam increase to the desired value in about 25 μs. For the large changes needed for a quench involving of hundreds of milliwatts of power, the response is more complicated. During the initial rapid ramp, the intensity reaches about 85% of its steady-state value, as seen in panel A in Figure C.1. There is a $\sim$80 kHz signal visible in the intensity but this small amplitude noise does not affect the system evolution because no other experimental timescale is that fast. After

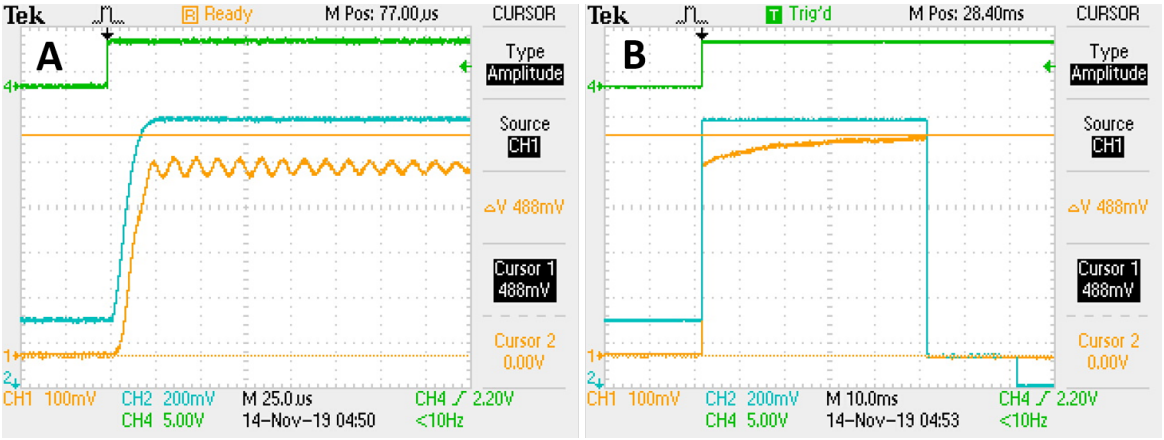

Figure C.1. Photodiode measurements of the dipole trap beam intensity after a sudden increase in EOM control voltage. On the oscilloscope, the sudden jump in the green signal marks the time at which the intensity is set to increase. The blue signal monitors the voltage applied to the EOMs, while the yellow signal is the light intensity measured on a photodiode. A quench to a 100x deeper trap is shown, with the solid horizontal yellow line representing the steady-state value of the deeper trap intensity. The light intensity response is very quick (25 μs, as seen in panel A), followed by a slower relaxation to steady-state over tens of milliseconds (panel B). In the blown-up view of the first 200 μs in panel A, there is a ∼80 kHz signal on top of the slow response. This is faster than any other evolution timescale and therefore does not affect the system.

that, thermal effects in the EOMs cause the light to slowly reach the nominal intensity in about 70 ms (see zoomed-out view in panel B). The shutoff at the end of the quench (not shown here) takes ∼15 μs.

Changing the ramp-up and ramp-down times, since they are limited by the slew rate of the voltage supply and thermal effects in the EOMs, requires hardware changes. But with the existing hardware we can essentially eliminate the 70 ms relaxation time by initially overshooting and gradually decreasing the control voltage as the intensity control system relaxes. An example of this is shown in Figure C.2, where 3 ramps are stitched together to make the overall shape of the pulse as constant as possible during the quench. In the above example, there is initially an exponential ramp that starts at an overshot level and decays for 1.5 ms, followed by two linear ramps that slowly decrease

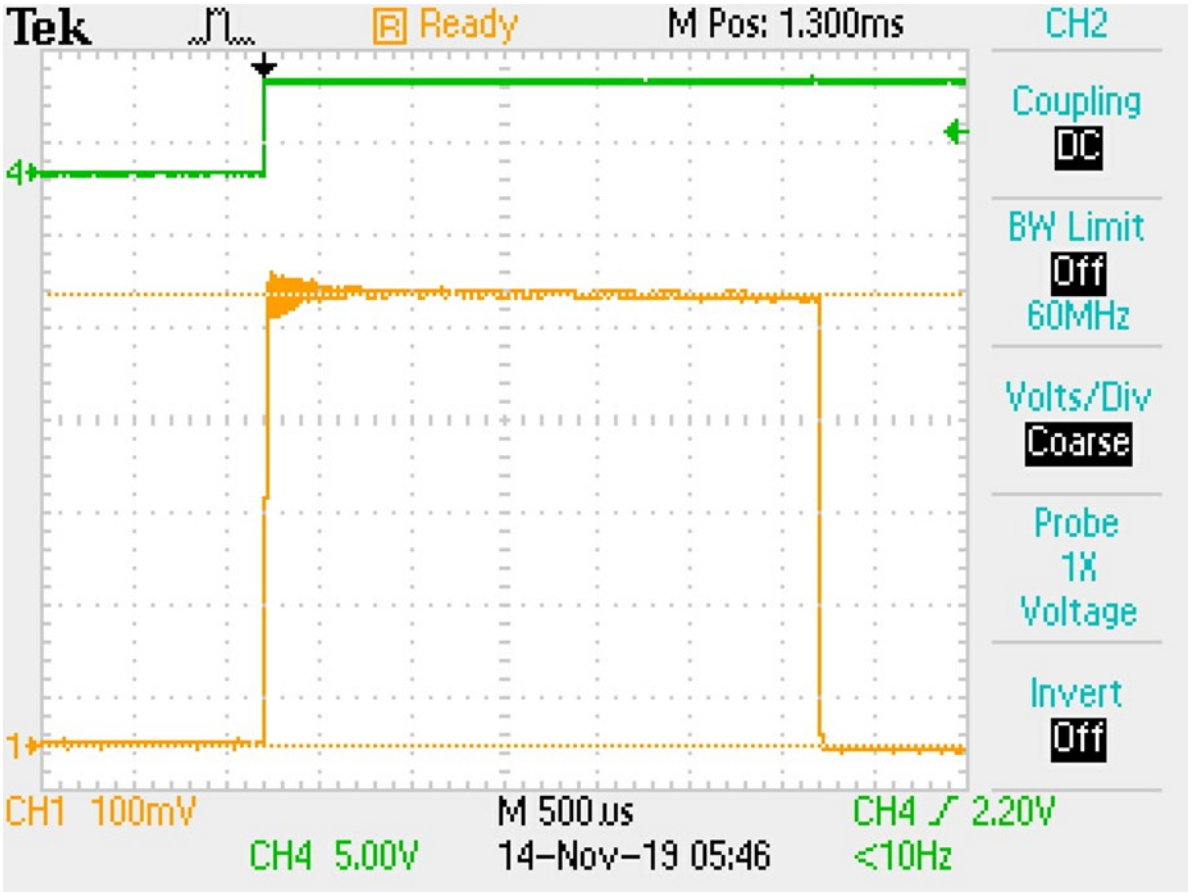

Figure C.2. Example measurement of a 100x quench we use in the experiment. The rise in the green signal shows when the control for the quench is set to start. Yellow denotes the light intensity during the $t_{ev} = 3$ ms quench where 3 separate ramps are joined together to compensate for the transients and make the pulse as rectangular as possible. The intensity stays within 2% of the steady-state value during the quench.

the intensity and last for ∼0.7 ms each. Other quench durations need other combinations of ramps to make the pulse shape rectangular. For short quenches for example, one exponential ramp might suffice. However for quenches longer than a few milliseconds, we find that 3 ramps work just fine, where the last linear ramp needs to be much longer than the first two.

We are able to achieve a quench with an intensity that is within 2% of nominal steady-state value needed for the deeper trap. The measurement of the intensity is prone

to drifts of 2% during the course of data acquisition, so we periodically make adjustments to the EOM voltage to reasonably keep the quenches as consistent as possible.

Appendix D

Calculation of the initial transverse atom distribution

In order to simulate the experiments involving large trap quenches using GHD, we need to know the distribution of atoms among tubes. Individual tube evolution is then calculated and a weighted average over tubes is performed for comparison to experimental measurements.

We use two measurements as a starting point for the initial distribution calculation: the total atom number N_{tot}, and the full initial 3D trapping configuration provided by the crossed dipole trap (see Equation 4.1). We assume that as the 2D optical lattice is ramped up from the starting point of the BEC, the transition from 3D to 1D is adiabatic. The gas is therefore assumed to remain in the ground state until a critical lattice depth U_{2D}^{*} at which tubes "decouple" into individual 1D gases, after which they evolve independently of each other. In reality this is not the case as different regions in the ensemble decouple at different times, but this approximation is gives us an answer

that is consistent with observations.

With the assumption of adiabaticity, we can assign a global chemical potential μ that is shared by all tubes across the 2D array up until they decouple. In steady state one can think of filling up the axial trap $U(z)$ for each tube with atoms until the energy reaches the level of the chemical potential. Mathematically this is written as [12]

$$\begin{aligned} \phi\left(n_{i,j}(z)\right) + U_{i,j}(z) = \mu \quad & for \quad |z| \leq R_{i,j} \\ n_{i,j} = 0 \qquad\qquad & for \quad |z| > R_{i,j} \end{aligned} \tag{D.1}$$

Here I have the used the notation with subscripts i, j so that a tube with those indices has a position (x_i, y_j) in the 2D array. $n_{i,j}$ is the 1D density in the tube, $\phi(n)$ is the Gibbs free energy per particle, $U_{i,j}(z)$ is the trapping potential along the tube. $R_{i,j}$ is the axial position of the edge of the atomic cloud within that tube, and can be defined by imposing a normalization condition for the number of atoms in a tube, $N_{i,j}$:

$$\int_{-R_{i,j}}^{R_{i,j}} n_{i,j}(z)dz = N_{i,j} \tag{D.2}$$

The Gibbs free energy can be derived using a classical hydrodynamic approximation of a trapped gas in local thermal equilibrium at T=0 [12]:

$$\phi(n) = \left(1 + n\frac{\partial}{\partial n}\right)\epsilon(n) \tag{D.3}$$

where $\epsilon(n) = \frac{\hbar^2}{2m}n^2 e\left(\gamma(n)\right)$ is the energy per particle. $\gamma = 2/n|a_{1D}|$ is the familiar dimensionless coupling parameter and $e(\gamma)$ is a complicated function that arises from

the solution of the Lieb-Liniger system of equations, and is often tabulated for use in calculations of 1D gas behavior. We can further simplify the expression for the Gibbs free energy by taking the derivative in Equation D.3:

$$\phi = \frac{2\hbar^2}{m|a_{1D}|^2}\frac{1}{\gamma^2}\left(3e(\gamma) - \gamma\frac{de}{d\gamma}\right) \tag{D.4}$$

Here it is convenient to write in terms of γ because one can easily determine the value with the tabulated function. Given the simple relation between γ and n, it is possible to solve for the density $n(z)$ by applying the constraint in Equation D.1 for a given chemical potential.

The decoupling depth enters the problem through the mapping parameter $|a_{1D}|$. For a given decoupling depth and chemical potential, there exists a solution for $n_{i,j}(z)$ and therefore the tube occupation number $N_{i,j}$.

$$\sum_{i,j} N_{i,j} = N_{tot} \tag{D.5}$$

We use the total atom number to work backwards and solve for the correct values of the decoupling depth and chemical potential that satisfy Equation D.5. In the process we obtain the atom distribution among tubes $N_{i,j}$ that is then fed as the initial condition for GHD simulations.

Appendix E

Experimentally extracting the rapidity energies and errors

In the initial image processing, high-spatial-frequency interference fringes are removed using a principal component analysis technique (see Appendix A). All the work presented in this thesis concerns the axial evolution of the system, so we integrate each image transversely to get an axial profile. For data analysis of the rapidity and momentum distributions after trap quenches, we take an average of 15 of the transversely-integrated images at each evolution time step. Since the axial position of the atomic cloud can vary by $\sim$50 μm from image to image due to magnetic field fluctuations, the averaging step includes fitting the top of the distribution to a Gaussian and shifting and aligning their centers to the axial position $z = 0$. Even after averaging, there often remains a low frequency signal in the background of the images (it is visible in the panels A-C in Figure E.1). This can be problematic when trying to extract quantities such as the total integrated atom number and energy associated with rapidity/momentum distributions,

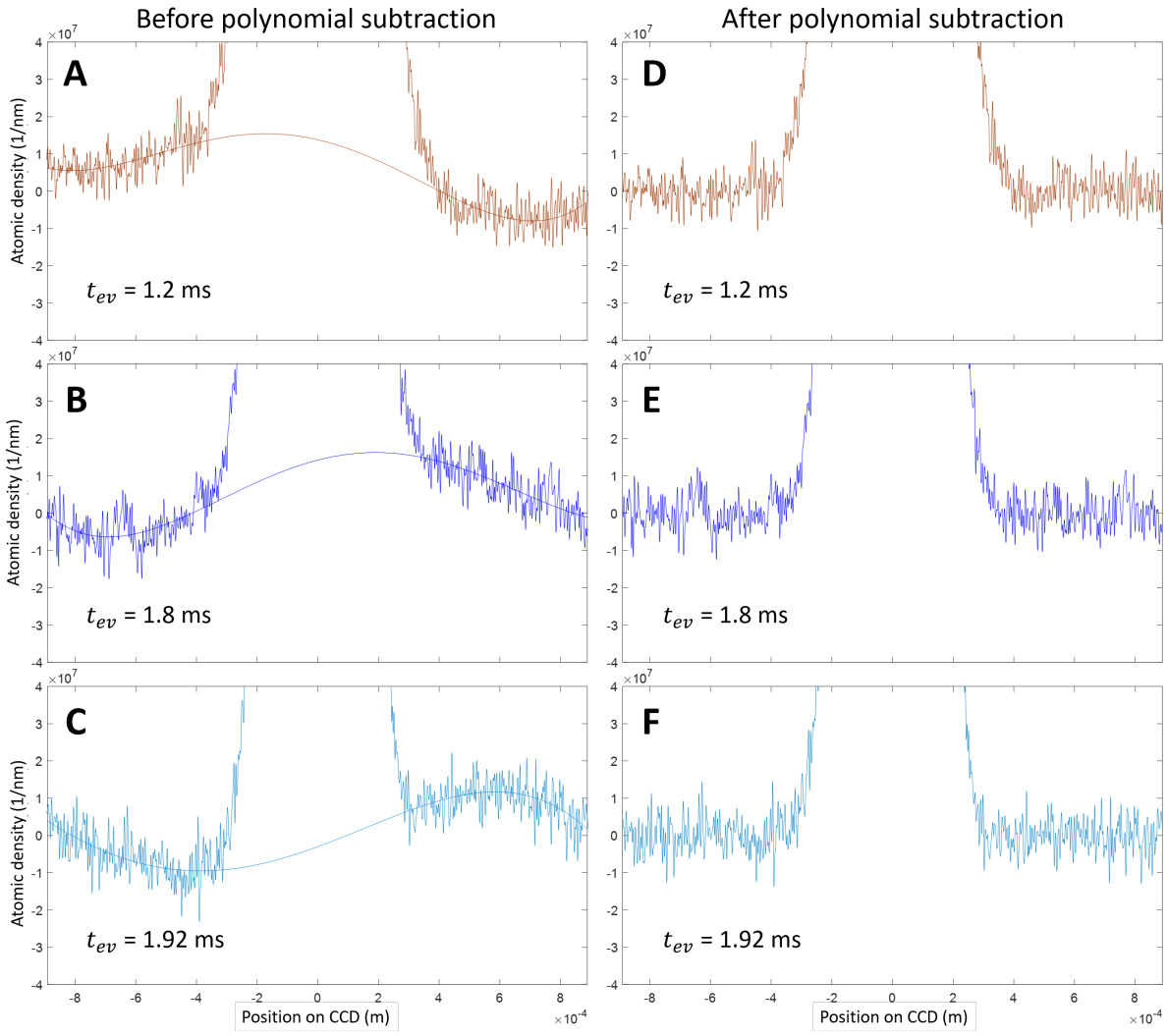

Figure E.1. Examples of application of the polynomial subtraction method on axial momentum distribution profiles. Momentum distributions at three different times after the 100x quench have a slowly varying background signal (panels A-C) after transverse integration of the images and averaging of 15 shots. A 4^{th} order polynomial fits well in the region excluding the atom signal (see the smooth solid lines in panels A-C). After subtracting the polynomial from the distribution, the residual background level is much closer to zero (panels D-F).

since they rely on the background level outside the atom signal being close to zero but also because the latter increases as the square of the axial coordinate.

Ideally we would like to remove as much of the slowly varying background in the distributions. We find that a 4^{th} order polynomial fit to the region outside the atom

signal is able to capture the background behavior very well (smooth solid lines panels A-C in Figure E.1), so we apply and subtract the fit polynomial for every curve. Backgrounds of the resulting profiles appear very flat, as seen in panels D-F in Figure E.1, but there are additional uncertainties in the zero level in the region with atoms. I discuss these later in this Appendix.

Once we have well-behaved and normalized axial distributions we can extract rapidity and kinetic energies per particle, in the form of Equation 5.1 in Chapter 5. In practice we measure time-of-flight (TOF) distributions, so the momentum coordinate is the position axis scaled according to the mapping defined by the duration of the TOF:

$$p_{TOF} = \frac{m z_{TOF}}{t_{TOF}} \tag{E.1}$$

where m is the mass of the Rb atom, z_{TOF} is the axial coordinate, and t_{TOF} is the TOF used for the measurement at a given evolution time. Integrating numerically, each spatial slice with position z_i and width Δz_i contributes an energy equal to $f(z_i)\frac{p_i^2}{2m}$. Therefore the total energy up to a maximum momentum z_m can be written as

$$E_{z_m} = \sum_{z_i \in [-z_m, z_m]} \frac{p_i^2}{2m} f(z_i) \Delta z_i = \sum_{z_i \in [-z_m, z_m]} \frac{m}{2} \left(\frac{z_i}{t_{\mathrm{TOF}}} \right)^2 f(z_i) \Delta z_i \tag{E.2}$$

As the integration bound z_m is increased to include the entire atom signal, E_{z_m} rises and starts saturating to its true value E (shown in Figure E.2). We take E to be the average value between two cutoff points. The left cutoff (shown in red circles in Figure E.2) is the point where the energy curve intersects a 2^{nd} order polynomial that

passes through the origin and the first maximum of the highest and lowest energy curves ($t_{ev} = 0$ ms and $t_{ev} = 1.32$ ms). The right cutoff is at a constant value of $z_m = 0.6$ mm for all energy curves, past which there are clearly no atoms and the noise in the background disproportionately contributes to the energy.

To extract error bars, we consider three sources of uncertainty. First, we take the contribution from the variation of E in the the energy curve as the peak-to-peak fluctuation in the flat region. The second contribution comes from the uncertainty in the background level after the 4^{th} order polynomial subtraction. We filter out noise with a spatial frequency higher than $1.25 \times 10^4\ m^{-1}$, as those have a negligible effect on the energy. The rms amplitude of the remaining background level is then used with Equation E.2 to obtain its associated energy error. Lastly, how much the 4^{th} order polynomial changes the atom signal region of the axial distribution is also taken into consideration. In the noise spectrum of the background, we find the amplitude A_t of the spatial frequency component with length L_t equal to the region with atoms. This mode has a form $f_t(z_i) = A_t cos(\pi z_i / L_t)$, so the error associated with it is obtained again using Equation E.2. The combined error is computed as the quadrature sum from all three sources of uncertainty.

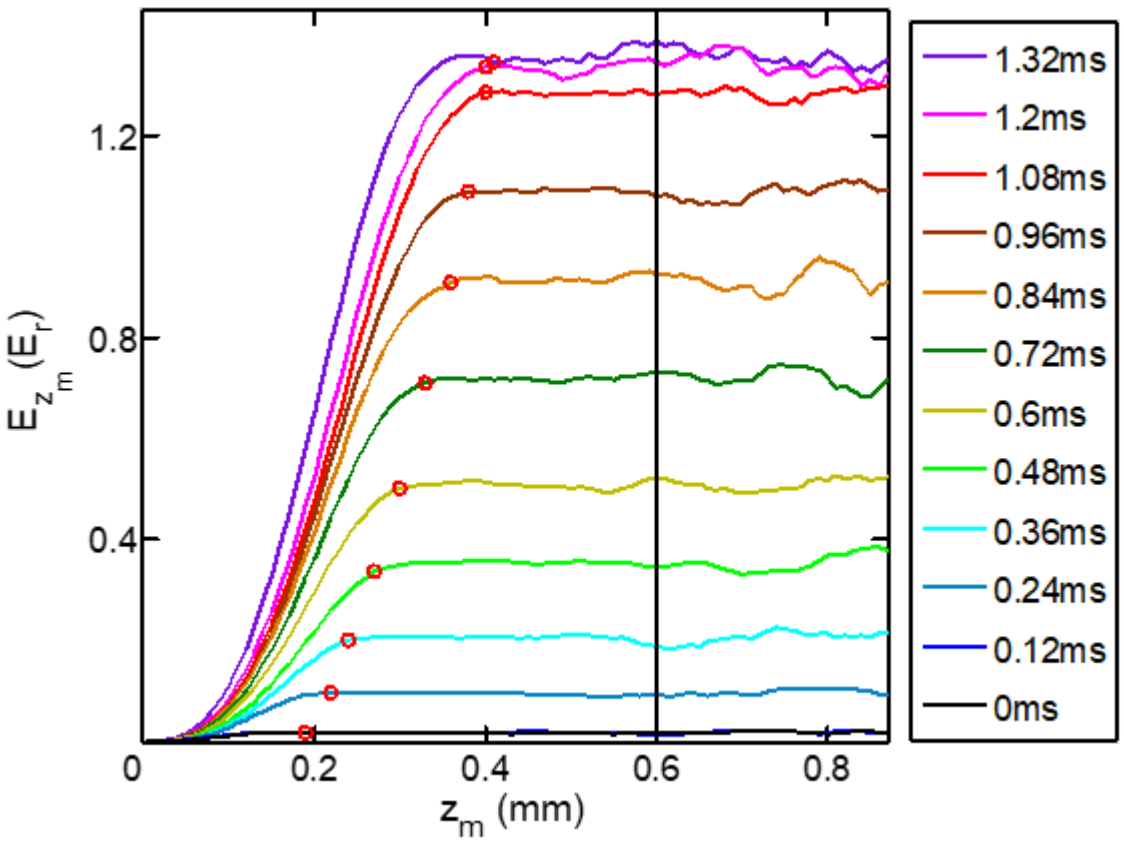

Figure E.2. Integrated rapidity energy after the 100x quench as a function of the size of the integration region. The results of carrying out the integral in Equation E.2 are shown for rapidity distributions for the first half-cycle. As E_{z_m} increases it aymptotes at the rapidity energy. We take the true value of the energy as the average value in the region between the left cutoff (marked by red circles) and the right cutoff (black line at $z_m = 0.6$ mm).

Appendix F

Spatial evolution of the atomic cloud during the quench

Due to the nature of our absorption imaging scheme, it is not possible to resolve individual tubes and the densities are too high for in-situ measurements of the 1D gas size. Instead of direct observations, we infer the spatial evolution of the 1D gas ensemble using GHD, since we know it works well in reproducing experimental results of observables like rapidity distributions.

F.1 Evolution during the 10x trap quench

For the experimental parameters used for the 10x quench, changes in size and coupling parameter are modest. As mentioned in Chapter 5, the average value of γ is initially 1.4 and reaches a minimum of 0.3 at the peak compression point. Meanwhile the central tube containing 140 atoms ranges from $\gamma \approx 0.9$ and to $\gamma \approx 0.2$ (see the bottom left

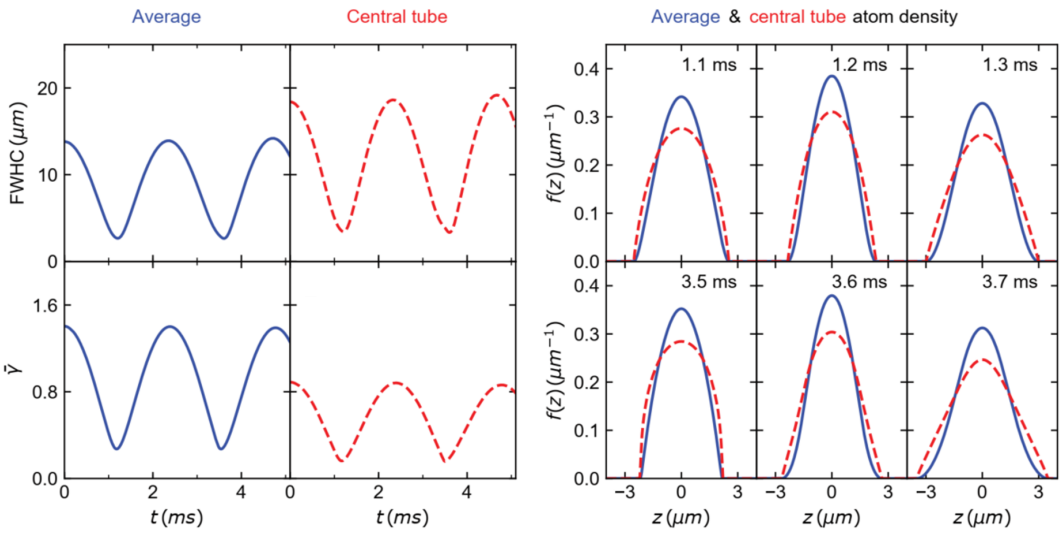

Figure F.1. Evolution of spatial size and coupling parameter for the 10x quench. All calculations are done using GHD with the relevant trapping parameters and with a total atom number $N = 3 \times 10^5$. Solid blue lines show quantities that are averaged over all occupied tubes, while red dashed lines denote the same for the central tube with $N = 140$ atoms. On the left, the top (bottom) panels display the full width at half the central density (coupling parameter) evolution for the first two cycles. 1D spatial distributions near peak compression points in the two cycles are shown in panels on the right.

panels in Figure F.1).

During the evolution, the 1D cloud size (full width at half the central density) for an average tube falls from a maximum of 14 μm to 3 μm, while that for the central tube goes from 18 μm to 4 μm.

Spatial distributions $f(z)$ for the tube average and central tube near the highest density times in the first two cycles are shown in the panels on the right in Figure F.1. The changes are not large at all, showing the relatively slow evolution of quasiparticles.

F.2 Evolution during the 100x trap quench

In contrast, for our 100x quench the evolution is very different. As seen in Figure F.2, the density in the center tube undergoes dramatic changes close to the half-cycle points. Even when averaged over tubes, the full width at half central density decreases by a factor of 35 as the size goes from 17 μm to 0.5 μm, as seen in the left panels in Figure F.3. Being such a large quench, the large variation in density corresponds to the gas passing through coupling regimes, starting in the Tonks-Girardeau regime reaching well into the intermediate coupling regime at maximal compression.

Unlike the 10x quench, there is rapid change in the spatial distribution near half-cycle, which results in the quasiparticle behavior varying quickly as a large amount of kinetic energy is converted to interaction energy. Interestingly, there are peculiar features in the density by the second cycle, and give rise to some sharpness even in the ensemble average.

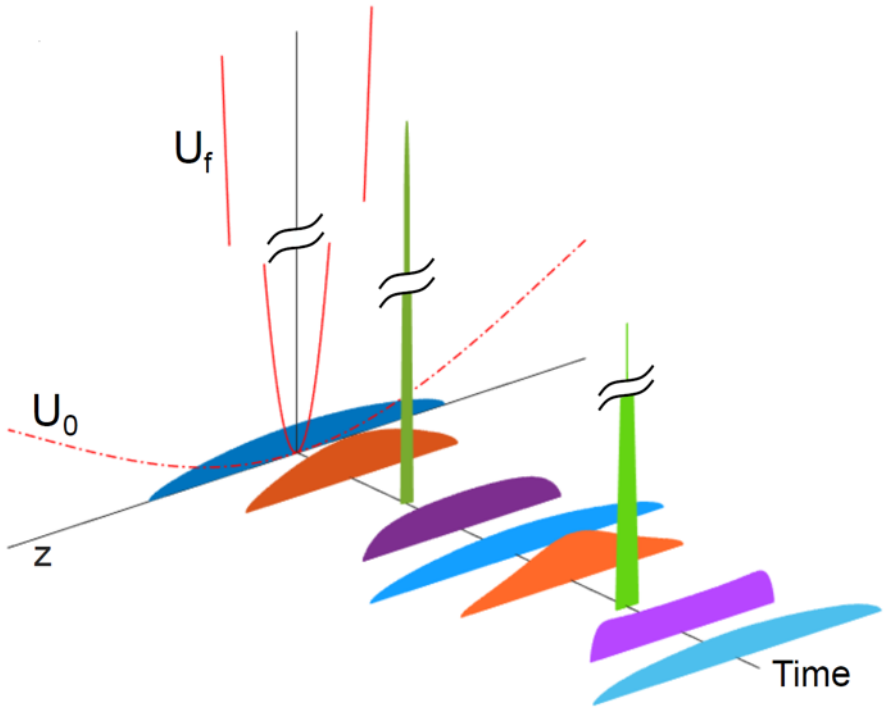

Figure F.2. Illustration plotting the spatial distribution $f(z)$ evolution in the central tube after the 100x quench. Distributions are shown at quarter-cycle steps for the first two cycles. The density increases by a large factor from $t = 0$ to mid-cycle, such that a break in the vertical axis needs to be introduced to see the distributions on a visible scale.

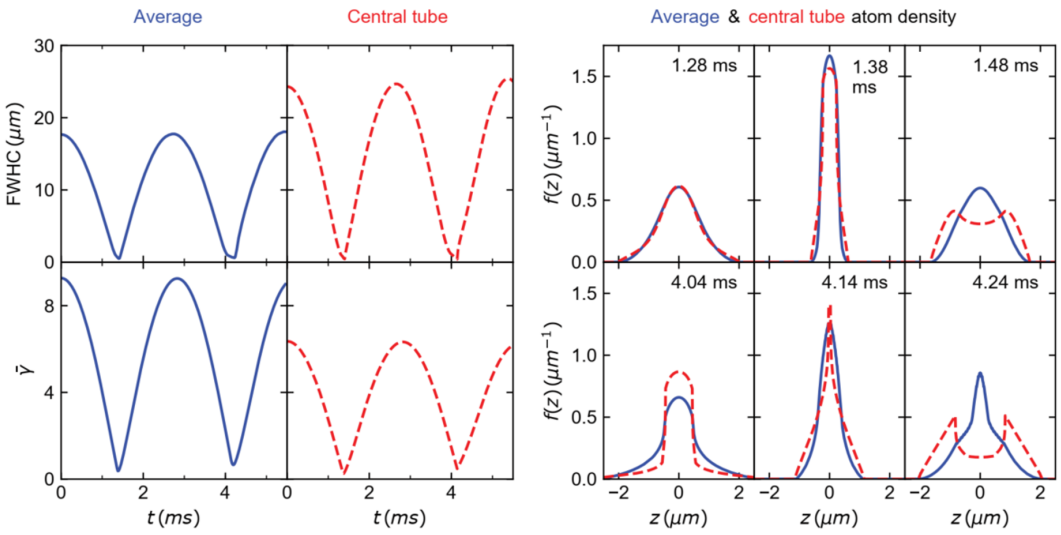

Figure F.3. Evolution of spatial size and coupling parameter for the 100x quench. GHD calculations are performed with the appropriate trapping parameters and with a total atom number $N = 9.8 \times 10^4$. Like in Figure F.1, solid blue lines are tube averaged quantities, and red dashed lines are for the central tube with $N = 24$ atoms. Panels on the left display the full width at half the central density and coupling parameter during for the first two cycles. On the right, spatial distributions near peak compression points are shown in panels on the right. Here, individual tubes start to exhibit sharp features in the second second cycle, but are mostly smeared when averaged over tubes.

Bibliography

[1] Caux, J.-S. and F. H. L. Essler (2013) "Time evolution of local observables after quenching to an integrable model," *Phys. Rev. Lett.*, **110**, p. 257203.

[2] Yang, C. N. and C. P. Yang (1969) "Thermodynamics of a one dimensional system of bosons with repulsive delta function interaction," *J. Math. Phys.*, **10**, p. 1115.

[3] Paredes, B., A. Widera, V. Murg, O. Mandel, S. Folling, I. Cirac, G. V. Shlyapnikov, T. W. Hansch, and I. Bloch (2004) "Tonks-Girardeau gas of ultracold atoms in an optical lattice," *Nature*, **429**, p. 277.

[4] Haller, E., M. Gustavsson, M. J. Mark, J. G. Danzl, R. Hart, G. Pupillo, and H.-C. Nagerl (2009) "Realization of an Excited, Strongly Correlated Quantum Gas Phase," *Science*, **325**, p. 1224.

[5] Wilson, J. M., N. Malvania, Y. Le, Y. Zhang, M. Rigol, and D. S. Weiss (2020) "Observation of dynamical fermionization," *Science*, **367**, p. 1461.

[6] Schemmer, M., I. Bouchoule, B. Doyon, and J. Dubail (2019) "Generalized Hydrodynamics on an Atom Chip," *Phys. Rev. Lett.*, **122**, p. 090601.

[7] Girardeau, M. (1960) "Relationship between Systems of Impenetrable Bosons and Fermions in One Dimension," *Journal of Mathematical Physics*, **1**, p. 516.

[8] Lieb, E. H. and W. Liniger (1963) "Exact analysis of an interacting Bose gas. I. The general solution and the ground state," *Phys. Rev*, **130**, p. 1605.

[9] Bethe, H. (1931) "On the theory of metals," *Zeitschrift fur Physik*, **71**, p. 205.

[10] Kinoshita, T., T. Wenger, and D. S. Weiss (2004) "Observation of a One-Dimensional Tonks-Girardeau Gas," *Science*, **305**, p. 1125.

[11] Olshanii, M. (1998) "Atomic Scattering in the Presence of an External Confinement and a Gas of Impenetrable Bosons," *Phys. Rev. Lett.*, **81**, p. 938.

[12] Dunjko, V., V. Lorent, and M. Olshanii (2001) "Bosons in Cigar-Shaped Traps: Thomas-Fermi Regime, Tonks-Girardeau Regime, and In Between," *Phys. Rev. Lett.*, **86**, p. 5413.

[13] Rigol, M., V. Dunjko, V. Yurovsky, and M. Olshanii (2007) "Relaxation in a Completely Integrable Many-Body Quantum System: An Ab Initio Study of the Dynamics of the Highly Excited States of 1D Lattice Hard-Core Bosons," *Phys. Rev. Lett.*, **98**, p. 050405.

[14] Caux, J.-S. and R. M. Konik (2012) "Constructing the Generalized Gibbs Ensemble after a Quantum Quench," *Phys. Rev. Lett.*, **109**, p. 175301.

[15] Castro-Alvaredo, O. A., B. Doyon, and T. Yoshimura (2016) "Emergent Hydrodynamics in Integrable Quantum Systems Out of Equilibrium," *Phys. Rev. X.*, **6**, p. 041065.

[16] Bouchoule, I. and J. Dubail (2021) "Generalized Hydrodynamics in the 1D Bose gas: theory and experiments," .

[17] Sutherland, B. (2004) *Beautiful models: 70 years of exactly solved quantum many-body problems*, World Scientific Publishing Company.

[18] Mazets, I. E., T. Schumm, and J. Schmiedmayer (2008) "Breakdown of Integrability in a Quasi-1D Ultracold Bosonic Gas," *Phys. Rev. Lett.*, **100**, p. 210403.

[19] Tang, Y., W. Kao, K.-Y. Li, S. Seo, K. Mallaya, M. Rigol, S. Gopalakrishnan, and B. L. Lev (2018) "Thermalization near integrability in a dipolar quantum Newton's cradle," *Phys. Rev. X.*, **8**, p. 021030.

[20] Mazets, I. E. (2011) "Integrability breakdown in longitudinaly trapped, one-dimensional bosonic gases," *The European Physical Journal D*, **65**, p. 43.

[21] Dubail, J. (2019) "A more efficient way to describe interacting quantum particles in 1D," *Physics*, **9**, p. 153.

[22] Doyon, B. (2020) "Lecture notes on generalised hydrodynamics," *SciPost Phys. Lect. Notes*, **18**.

[23] Bulchandani, V. B., R. Vasseur, C. Karrasch, and E. J. Moore (2017) "Solvable hydrodynamics of quantum integrable systems," *Phys. Rev. Lett.*, **119**, p. 220604.

[24] Minguzzi, A., P. Vignolo, and M. P. Tosi (2002) "High-momentum tail in the Tonks gas under harmonic confinement," *Phys. Rev. A.*, **294**, p. 222.

[25] Boninsegni, M., N. V. Prokof'ev, and B. V. Svistunov (2006) "Worm algorithm and diagrammatic Monte Carlo: A new approach to continuous-space path integral Monte Carlo simulations," *Phys. Rev. E.*, **74**, p. 036701.

[26] Boninsegni, M., N. V. Prokofev, and B. V. Svistunov (2006) "Worm algorithm for continuous-space path integral Monte Carlo simulations," *Phys. Rev. Lett.*, **96**, p. 070601.

[27] Xu, W. and M. Rigol (2015) "Universal scaling of density and momentum distributions in Lieb-Liniger gases," *Phys. Rev. A.*, **92**, p. 063623.

[28] Jacqmin, T., B. Fang, T. Berrada, T. Roscilde, and I. Bouchoule (2012) "Momentum distribution of one-dimensional Bose gases at the quasicondensation crossover: Theoretical and experimental investigation," *Phys. Rev. A.*, **86**, p. 043626.

[29] Wilson, J. M. (2020) *Dynamical Fermionization and Bose-Fermi Oscillation in One-Dimensional Bose Gases*, Ph.D. thesis, The Pennsylvania State University.

[30] Kinoshita, T., T. Wenger, and D. S. Weiss (2006) "A quantum Newton's cradle," *Nature*, **440**, p. 900.

[31] Riou, J.-F., A. Reinhard, L. A. Zundel, and D. S. Weiss (2012) "Spontaneous-emission-induced transition rates between atomic states in optical lattices," *Phys. Rev. A.*, **86**, p. 033412.

[32] Riou, J.-F., L. A. Zundel, A. Reinhard, and D. S. Weiss (2014) "Effect of optical-lattice heating on the momentum distribution of a one-dimensional Bose gas," *Phys. Rev. A.*, **90**, p. 033401.

[33] Tolra, B. L., K. M. O'Hara, J. H. Huckans, W. D. Phillips, S. L. Rolston, and J. V. Porto (2004) "Observation of Reduced Three-Body Recombination in a Correlated 1D Degenerate Bose Gas," *Phys. Rev. Lett.*, **92**, p. 190401.

[34] Zundel, L. A., J. M. Wilson, N. Malvania, L. Xia, J.-F. Riou, and D. S. Weiss (2019) "Energy-Dependent Three-Body Loss in 1D Bose Gases," *Phys. Rev. Lett.*, **122**, p. 013402.

[35] Zundel, L. A. (2019) *Studying the Onset of Thermalization with Out-of-equilibrium One-dimensional Bose Gases*, Ph.D. thesis, The Pennsylvania State University.

[36] Kinoshita, T., T. Wenger, and D. S. Weiss (2005) "All-optical Bose-Einstein condensation using a compressible crossed dipole trap," *Phys. Rev. A.*, **71**, p. 011602(R).

[37] Wenger, T. (2007) *Experiements on a One-Dimensional Bose Gas: Thomas Fermi to Tonks-Girardeau*, Ph.D. thesis, The Pennsylvania State University.

[38] Anderson, M. H., J. R. Ensher, M. R. Matthews, C. E. Wieman, and E. A. Cornell (1995) "Observation of Bose-Einstein Condensation in a Dilute Atomic Vapor," *Science*, **269**, p. 198.

[39] Davis, K. B., M.-O. Mewes, M. R. Andrews, N. J. van Druten, D. S. Durfee, D. M. Kurn, and W. Ketterle (1995) "Bose-Einstein Condensation in a Gas of Sodium Atoms," *Phys. Rev. Lett.*, **75**, p. 3969.

[40] Balykin, V. I., V. S. Letokhov, and V. I. Mushin (1980) "Observation of the cooling of free sodium atoms in a resonance laser field with a scanning frequency," *JETP Lett.*, **29**, p. 560.

[41] Ertmer, W., R. Blatt, L. Hall, and M. Zhu (1985) "Laser Manipulation of Atomic Beam Velocities: Demonstration of Stopped Atoms and Velocity Reversal," *Phys. Rev. Lett.*, **54**, p. 996.

[42] Segal, S. R., Q. Diot, E. A. Cornell, A. A. Zozulya, and D. Z. Anderson (2010) "Revealing buried information: Statistical processing techniques for ultracold-gas image analysis," *Phys. Rev. A.*, **81**, p. 053601.

[43] Rigol, M. (2005) "Finite-temperature properties of hard-core bosons confined on one-dimensional optical lattices," *Phys. Rev. A.*, **72**, p. 063607.

[44] Rigol, M. and A. Muramatsu (2005) "Fermionization in an Expanding 1D Gas of Hard-Core Bosons," *Phys. Rev. Lett.*, **94**, p. 240403.

[45] Minguzzi, A. and D. M. Gangardt (2005) "Exact Coherent States of a Harmonically Confined Tonks-Girardeau Gas," *Phys. Rev. Lett.*, **94**, p. 240404.

[46] Mei, Z., L. Vidmar, F. Heidrich-Meisner, and C. J. Bolech (2016) "Unveiling hidden structure of many-body wave functions of integrable systems via sudden-expansion experiments," *Phys. Rev. A.*, **93**, p. 021607.

[47] Campbell, A. S., D. M. Gangardt, and K. V. Kheruntsyan (2015) "Sudden Expansion of a One-Dimensional Bose Gas from Power-Law Traps," *Phys. Rev. Lett.*, **114**, p. 125302.

[48] Fokkema, T., I. S. Eliens, and J.-S. Caux (2014) "Split Fermi seas in one-dimensional Bose fluids," *Phys. Rev. A.*, **89**, p. 033637.

[49] Doyon, B., J. Dubail, R. Konik, and T. Yoshimura (2017) "Large-scale description of interacting one-dimensional Bose gases: Generalized hydrodynamics supersedes conventional hydrodynamics," *Phys. Rev. Lett.*, **119**, p. 195301.

[50] Ruggiero, P., P. Calabrese, B. Doyon, and J. Dubail (2020) "Quantum generalized hydrodynamics," *Phys. Rev. Lett.*, **124**, p. 140603.

[51] Rosi, G. D. and S. Stringari (2016) "Hydrodynamic versus collisionless dynamics of a one-dimensional harmonically trapped Bose gas," *Phys. Rev. A.*, **94**, p. 063605.

[52] Peotta, S. and M. D. Ventra (2014) "Quantum shock waves and population inversion in collisions of ultracold atomic clouds," *Phys. Rev. A.*, **89**, p. 013621.

[53] Kormos, M., Y.-Z. Chou, and A. Imambekov (2011) "Exact three-body local correlations for excited states of the 1D Bose gas," *Phys. Rev. Lett.*, **107**, p. 230405.

[54] van den Berg, R., B. Wouters, S. Eliens, J. D. Nardis, R. M. Konik, and J.-S. Caux (2016) "Separation of Time Scales in a Quantum Newton's Cradle," *Phys. Rev. Lett.*, **116**, p. 225302.

[55] Caux, J.-S., B. Doyon, J. Dubail, R. Konik, and T. Yoshimura (2019) "Hydrodynamics of the interacting Bose gas in the quantum Newton cradle setup," *SciPost Phys.*, **6**, p. 70.

[56] Gudyma, A. (2015) *Non-equilibrium dynamics of a trapped one-dimensional Bose gas*, Ph.D. thesis, Universite Paris-Saclay.

[57] Lieb, E. H. (1963) "Exact Analysis of an Interacting Bose Gas. II. The Excitation Spectrum," *Phys. Rev.*, **130**, p. 4.

Vita

Neel Malvania

Education

B. Eng. in Engineering Physics, McMaster University (2014).

Academic and Professional Experience

Graduate Research Assistant, Department of Physics, Pennsylvania State University (June 2015 – July 2021). Supervisor: David S. Weiss

Teaching Assistant, Department of Physics, Pennsylvania State University (August 2014 – December 2015). Supervisor: Daniel Costantino

Publications

- N. Malvania, Y. Zhang, Y. Le, J. Dubail, M. Rigol, D. S. Weiss. "Generalized hydrodynamics in strongly interacting 1D Bose gases, Science **373**, 1129-1133 (2021).
- J. M. Wilson, N. Malvania, Y. Le, Y. Zhang, M. Rigol, D. S. Weiss. "Observation of dynamical fermionization", Science **367**, 1461-1464 (2020).
- L. A. Zundel, J. M. Wilson, N. Malvania, L. Xia, J. F. Riou, D. S. Weiss. "Energy-dependent 3-body loss in 1D Bose gases", Phys. Rev. Letters **122**, 013402 (2019).

Invited Talks

- SRI International, Princeton, NJ (April 2021, virtual).
- The MITRE Corp, McLean, VA (April 2021, virtual).
- Sandia National Laboratory, Albuquerque, NM (February 2021, virtual).

Select Conference Presentations

- **Speaker**, 52st Annual Meeting of APS Division of Atomic, Molecular and Optical Physics, "*Generalized Hydrodynamics in strongly interacting quenched 1D Bose gases."* (June 2021).
- **Speaker**, 51st Annual Meeting of APS Division of Atomic, Molecular and Optical Physics, "*Rapidity evolution after a trap quench in a 1D Bose gas."* (June 2020).
- **Speaker**, 50th Annual Meeting of APS Division of Atomic, Molecular and Optical Physics, "*Energy-dependent 3-body loss in 1D Bose gases."* (May 2019).
- **Poster**, 49th Annual Meeting of APS Division of Atomic, Molecular and Optical Physics, "*Onset of thermalization in a nearly integrable 1D Bose gas."* (May 2018).
- **Speaker**, 47th Annual Meeting of APS Division of Atomic, Molecular and Optical Physics, "*Observation of dynamical fermionization in 1D Bose gases."* (May 2016).